Design, Implementation and Control of a Magnetic Levitation Device

by

Ehsan Shameli

A thesis
presented to the University of Waterloo
in fulfillment of the
thesis requirement for the degree of

Doctor of Philosophy

in

Mechanical Engineering

Waterloo, Ontario, Canada, 2008

Abstract

Magnetic levitation technology has shown a great deal of promise for micromanipulation tasks. Due to the lack of mechanical contact, magnetic levitation systems are free of problems caused by friction, wear, sealing and lubrication. These advantages have made magnetic levitation systems a great candidate for clean room applications. In this thesis, a new large gap magnetic levitation system is designed, developed and successfully tested. The system is capable of levitating a 6.5(gr) permanent magnet in 3D space with an air gap of approximately 50(cm) with the traveling range of 20x20x30 mm^3. The overall positioning accuracy of the system is 60μm.

With the aid of finite elements method, an optimal geometry for the magnetic stator is proposed. Also, an energy optimization approach is utilized in the design of the electromagnets.

In order to facilitate the design of various controllers for the system, a mathematical model of the magnetic force experienced by the levitated object is obtained. The dynamic magnetic force model is determined experimentally using frequency response system identification. The response of the system components including the power amplifiers, and position measurement system are also considered in the development of the force model.

The force model is then employed in the controller design for the magnetic levitation device. Through a modular approach, the controller design for the 3D positioning system is started with the controller design for the vertical direction, i.e. z, and then followed by the controller design in the horizontal directions, i.e. x and y.

For the vertical direction, several controllers such as PID, feed forward and feedback linearization are designed and their performances are compared. Also a control command conditioning method is introduced as a solution to increase the control performance and the results of the proposed controller are compared with the other designs.

Experimental results showed that for the magnetic levitation system, the feedback linearization controller has the shortest settling time and is capable of reducing the positioning error to RMS value of 11.56μm.

The force model was also utilized in the design of a model reference adaptive feedback linearization (MRAFL) controller for the z direction. For this case, the levitated object is a small microrobot equipped with a remote controlled gripper weighting approximately 28(gr). Experimental results showed that the MRAFL controller enables the micro-robot to pick up and transport a payload as heavy as 30% of its own weight without a considerable effect on its positioning accuracy. In the presence of the payload, the MRAFL controller resulted in a RMS positioning error of 8μm compared with 27.9μm of the regular feedback linearization controller.

For the horizontal position control of the system, a mathematical formula for distributing the electric currents to the multiple electromagnets of the system was proposed and a PID control approach was implemented to control the position of the levitated object in the xy-plane. The control system was experimentally tested in tracking circular and spiral trajectories with overall positioning accuracy of 60μm.

Also, a new mathematical approach is presented for the prediction of magnetic field distribution in the horizontal direction. The proposed approach is named the pivot point method and is capable of predicting the two dimensional position of the levitated object in a given vertical plane for an arbitrary current distribution in the electromagnets of the levitation system. Experimental results showed that the proposed method is capable of predicting the location of the levitated object with less than 10% error.

Acknowledgements

I would like to thank my supervisors, Professor Behrad Khamesee and Professor Jan Paul Huissoon, and my research colleagues David Graig and Caglar Elbuken for their support and guidance during the course of my research. I would also like to acknowledge the support of my friends Babak Ebrahimi and Roozbeh Borjian, and my parents towards the final product you are now reading.

Funding for this research was provided by the Natural Science and Engineering Research Council of Canada (NSERC).

Table of Content

List of Tables

List of Figures

Chapter 1

Introduction

1.1. Overview

The use of magnetic fields as a method of actuation has been considered for over five decades. The initial applications of magnetic actuation were in solenoid actuators, magnetic cranes and electrical switches.

Approximately three decades ago, the first magnetic levitation train was proposed and initialized as a high speed mass transportation vehicle. Various experimental and a large number of theoretical studies have been done in Japan, Germany and the United States and have resulted in interesting outcomes.

After several years, changing market requirements have forced manufacturers to develop new technologies of actuation. In the high-tech industry, which increasingly relies on microassembly, product requirements drive manufacturers to change their production strategies. Many of these products need to be fabricated under highly controlled environments. Recently, magnetic actuation has been shown to be a feasible solution for high performance actuators delivering ultra fine positional control.

1.2. Applications of Magnetic Actuation

Due to the lack of mechanical contact, magnetic actuators can be used in special environments without problems caused by friction, abrasion or lubrication. These advantages have provided motivation to use magnetic levitation in wafer transportation [1]-[6] photolithography [7]-[10], teleoperation [11]-[14], wind tunnel [15]-[29], magnetic bearings [30]-[71] and many other applications.

1.2.1. Wafer Transportation

Since magnetic levitation systems are contactless and dust free, they are ideal for wafer transportation during semiconductor fabrication. This idea was introduced in [1] in which an attractive type magnetic levitation driven platform was proposed. In order to control the position, a feedback control scheme was employed. By transferring magnetic energy from an outside source, this platform is capable of linear, contactless movement without an onboard power supply.

In [2] and [3], Park et. al proposed a linear contactless wafer transport system. This system consists of a wafer carrier, two levitation tracks, two stabilization tracks and a propelling system. Levitation is achieved by using opposing forces produced between electromagnet tracks and permanent magnets assembled on the carrier. A number of electromagnets assembled at the corners of the levitation tracks stabilize the platform by using a simple feedback control. A constant propelling force is obtained by sending specific current patterns to the propulsion coils on the levitation tracks.

Yamakawa et. al. [4] reported a magnetic levitation transport system which can carry silicon wafers into a number of process chambers for product fabrication under particle-free conditions. Since there are no sliding mechanical parts in this system, it does not need lubricants. Therefore, the transport system is free from oil and has a long lifetime.

In [5], a linear induction motor implemented as the drive system and the attractive force of the motor was used to levitate a transportation stage in wafer distribution industry. The transportation stage consists of a U-shaped part surrounding a straight stationary track. By delivering an AC current to the coils assembled on the stationary track, the induction phenomenon results in enough attraction force to levitate the stage. The vertical position is controlled by tuning the frequency of the AC currents in coils.

In [6], a passively levitated stage is proposed. The system consists of a transportation stage, path track and propelling coils. A number of permanent magnets are assembled at the bottom of the transportation stage and the stationary path track. Levitation is achieved due to the opposing force generated between the permanent magnets. Several electromagnets are assembled at the sides of the path track. By delivering the electrical currents in a certain pattern to the electromagnets, the propulsion force is generated and the platform is transported along the path.

1.2.2. Photolithography

Magnetic levitation is also appropriate for stepper stages in photolithography. These stages provide large displacements in a plane, small displacements normal to the plane and small roll, pitch and yaw motions.

In [7], [8] and [9] a high precision magnetic levitation stage with a displacement range of 50(mm) x 50(mm) in the 2D plane was presented. A linear motor capable of providing forces in both suspension and translation is the key element of this stage.

The stage utilizes four levitation linear motors for suspension and a servo driver to provide the propulsion forces. Position feedback is provided by three plane mirror interferometers and three capacitance probes.

An oil medium is used to increase the damping of the system and provide more disturbance rejection and less power dissipation in the actuators. The stage operates with a positioning error as low as 5(nm) rms in the x- and y- directions and a maximum error of 2.2(nm) rms in the z- direction.

In [10] a planar magnetic levitation device is proposed which employs standard electromagnets to achieve a 2DOF motion. The electromagnets are assembled at the ends of the three arms of an imaginary star. The central axis of coils follow a star shaped pattern with angular distance of 120 degrees between each two adjacent axes.

The levitated stage is a small disk made of ferromagnetic material. This stage is placed at the center of the imaginary star. The vertical position of the disk is controlled by a fourth electromagnet suspended over the star patterned electromagnets. Two optical encoders are mounted on the top of the moving platform to feedback the planar position of the levitated disk. This system is proposed as a precision stage for photolithography.

1.2.3. Teleoperation

Magnetically suspended actuation is a powerful technique for teleoperation purposes which is extensively applicable in hazardous environments (nuclear reactors, biohazard laboratories, and chemical plants), minimally invasive surgeries and wind tunnels.

In [11], a coarse-fine teleoperation system is proposed. This system uses a 6DOF magnetic levitation device (MLD) master to control a 6DOF fine positioning MLD slave mounted on a 6DOF coarse positioner arm. The slave's flotor is levitated by six Lorentz actuators arranged at 60 degrees intervals around a horizontal ring.

The wrist's fixed stators are attached to the coarse positioner arm, whereas the coils of each actuator are contained in the thin hexagonal flotor shell. Optical beams are used to measure the position of the flotor with respect to the stator. This device is designed for psychophysical studies of system transparency.

Salcudean et. al [12]-[13] presented a force-reflecting teleoperation system comprising a conventional manipulator equipped with a magnetically levitated teleoperation master identical to the wrist. By using a combination of position and rate control, their suggested system would require only small operator hand motions but would provide low mechanical impedance, high motion resolution and force feedback over a substantial volume.

In [14] a master-slave teleoperation system is developed in which the slave robot is magnetically levitated. In contrast with ordinary master-slave systems, the levitated robot is isolated from any other contact forces from outside. This has highly improved the comfort and maneuverability of the teleoperation system.

1.2.4. Wind Tunnel

In [15]-[17], a magnetic suspension device for application in wind tunnels is introduced and calibrated. The proposed wind tunnel is constructed based on a magnetic suspension balance system having 10 coils. There are eight iron cored electromagnetic coils and two air-cored electromagnetic coils around the test section of the magnetic suspension wind tunnel.

The coils are arranged so as to generate a proper field to levitate the test model. A permanent magnet is embedded inside the test model body that is made of a light non-ferrite material.

A lateral effect detector is used to sense the motion along the x direction and roll angle and two quadrant detectors are used to measure the position and orientation in other directions. The test chamber has the cross section of 10(cm) x 10(cm) in the vertical plane.

In [18], Smith et al proposed a superconducting magnetic suspension system for measurement of drag on rotationally symmetric bodies in liquid helium flow field. There are two vertical support coils and two drag coils in the device. The drag and support fields are orthogonal.

The vertical support coils are of a counter wound racetrack configuration designed to produce a quadra pole field in the plane perpendicular to the flow. The drag coils are built up from Helmholtz pairs, designed to produce a particular field B and field gradient dB/dz along the direction of the flow.

The drag force is calculated based on the virtual work theory. Sensor coils mounted along the flow direction detect a flux change at the time that the levitated body is allowed to deflect a small amount of delta under the applied drag.

In [19], a superconducting magnetic levitation system is proposed for application in a large 8(ft) x 8(ft) wind tunnel. This device is capable of levitating a model airplane in air speeds up to 0.9 Mach.

Fourteen external electromagnets levitate and control the superconducting solenoid which is embedded inside the test model. The whole system is surrounded in a high pressure steel chamber.

Through experiments it was shown that the magnetic system generated a field of 6.1 Tesla and current density of 30,000(A/cm^2) and successfully levitated a model airplane.

Britcher et. al. [20]-[23] suggested an approach in which a superconducting solenoid is carried within the model being tested in the wind tunnel. The superconducting solenoid is assembled in place of the conventional ferromagnetic core. Using this technique, the size of the models being investigated can be considerably increased.

He also developed digital control strategies for the wind tunnel magnetic suspension and balance systems, which in turn permit wind tunnel testing of aircraft models free from support interference.

Johnson and Dress from the NASA Langley Research Center [24] reported a 13-inch subsonic wind tunnel using a magnetic suspension and balance System. This tunnel allows flow visualization over model spans of 6 to 8 inches and lengths of 8 to 12 inches.

The tunnel is capable of achieving air speeds up to Mach 0.5 and has predictable longitudinal Mach number distributions. There are many other examples of magnetic levitation based wind tunnels some of them can be found in references [25]-[29].

1.2.5. Magnetic Bearings

Since there is no mechanical contact between the rotor and stator, magnetic bearings are ideal for high rotating speeds in extreme environments and are utilized in many applications [30]-[34].

In general there are two types of magnetic bearings; passive and active. Passive magnetic bearings use permanent magnets and superconductors as the sources of magnetic energy and generally are stabilized without any need for closed loop control systems. Where as active magnetic bearings use electromagnets as one source of magnetic energy and need closed loop controllers to be stabilized.

In practice, magnetic bearings are used to levitate the rotor inside the stator.

1.2.6. Passive Magnetic Bearings

In [35], a passive hybrid superconductor-permanent magnet bearing is proposed for the levitation of the rotor inside stator.

In [36]-[37] two permanent magnet passive bearings are reported. The proposed bearings use the repulsive forces between the like magnetic poles for levitating the rotor.

Filatov et. al. [38]-[39] proposed a method for the design of passive magnetic bearings using high-temperature superconductors. Their design showed advantages of low force-displacement hysteresis and high ratios of the load capacity and stiffness versus bearing size and weight.

They reported a load capacity of 5.2(N) for a superconducting ring of 0.4(g) mass. The load capacity of the bearing were found to be 3.7 (N/cm^2).

An advantageous feature of passive suspension systems is that they are intrinsically stable, in contrast to active magnetic bearings and therefore can provide much higher reliability, which is known to be the crucial factor in applications requiring continuous non-contact suspension of high-speed rotors.

An example of such an application is flywheel energy storage systems [40], which are considered to be an attractive alternative to conventional electrochemical batteries from both environmental and overall energy efficiency aspects.

Researchers in [41]-[43] developed a radial-type superconducting magnetic bearings (SMB) for a 10(kW) flywheel energy storage system. The bearings consist of an inner-cylindrical stator composed of YBCO bulk superconductors and an outer-rotor composed of permanent magnets. The rotor is suspended without contact using the pinning forces of the bulk superconductors up to the speed of 7500 rpm. They estimated the rotation loss of the SMB as 40(W) at 7500 rpm, mainly caused by the inhomogeneous magnetic field of the bulk superconductors.

Bassani et. al. [44]-[46] studied the mathematical methods for calculation of forces acting on passive magnetic bearings and proposed a method to identify the stability domain of passive magnetic systems.

An interesting new application of magnetic bearings is their use in artificial hearts. Wang et. al. [47] utilized passive magnetic bearings in the structure of a brushless DC (BLDC) motor for blood pump application.

The magnetic suspension of the rotor is realized by the use of the proposed bearings. The axial stability of the rotor is obtained by the radial force of the passive magnetic bearings. The radial magnetic suspension of the machine rotor is achieved by the optimal design of the air-gap length, thickness and axial length of the permanent magnets in the bearings, and the BLDC motor.

Qian et. al. [48]-[49] reported a rotary impeller pump utilizing active magnetic bearings for blood pumping. The pump is composed of a rotor and a stator. The rotor comprises several permanent magnets and an impeller driven by a set of coils in the stator. Two passive magnetic bearings are used to levitate the rotor inside the stator.

In contrast with the passive magnetic bearings, active systems are capable of precisely controlling the air gap and vibrations of the rotor.

1.2.7. Active Magnetic Bearings

Polajzer et. al. [50]-[56] proposed the design procedure of a radial active magnetic bearing. The initial design is improved by a numerical optimization, using the bearing mass-force ratio as the minimization target. Using a 2 dimensional (2D) finite element method, the force is calculated via the Maxwell's stress tensor.

Through dynamic analysis of the active magnetic bearing, Polajzer et. al. showed that the magnetic nonlinearities and cross-coupling effects deteriorate the overall system's performance and proposed the use of real-time controllers to cope with the considerable fall in the electromotive forces due to these disturbing effects.

Nocolsky and his colleagues [57]-[62] presented a hybrid active system comprising a passive axial bearing and two active radial magnetic bearings. This system is designed for an induction machine with a vertical rotor and results in a fully levitated system up to the speed of 6300 rpm.

Each active radial bearing measures four shaft-positions using eddy-current sensors displaced each 90 degrees for measuring the shaft position and a PID control system for feeding back the currents.

Levitation of the shaft is achieved through using two NdFeB permanent magnets and bulk pieces of YBCO. The stiffness of the superconducting axial bearing is investigated by measuring the vertical and transversal elastic constants and showed a linear dependence on the air gap.

Schulz et. al. [63]-[65] proposed a concept for a reliable switching amplifier for active magnetic bearings. Their proposed amplifier consists of two or more left and right switching amplifier half-bridges. These so called “Hot Swap Modules” (HSMs) are connected in parallel, each with its own error detection and decoupling circuitry.

If an error occurs in an HSM, it is autonomously switched off and disconnects itself from the active magnetic bearing actuator, while the remaining, fully functioning HSMs take over the required current. This will significantly reduce the chance of failure for active magnetic bearing systems.

More research on active magnetic bearings can be found in the works done by Brown et. al. in [66]-[68] or others [69]-[71].

1.2.8. Microrobotics

Besides many industrial applications of magnetic levitation systems, remote actuation of objects can lead into promising results in the field of microrobotics. One of the more complex issues related to the design of microrobotic systems is the design of the propulsion system.

As objects scale down in size, viscous forces start to become dominant, and the amount of power required to propel the system per unit mass will increase [72]-[73].

For example, [74] describes several microrobots that use various piezoelectric-based actuator assemblies for motion. The authors discuss how their original design required 300 volts to actuate the piezoelectric actuators, while a more recent design allowed them to reduce the required input to 60 volts.

Of more recent interest is the development of ionic conducting polymer film (ICPF) actuators. Under wet conditions the ICPF actuator will deform under as little as 1.5 volts. This actuator was successfully implemented on a fish-like microrobot [75].

Depending on the size of the microrobot, electromagnetic [76]-[77] and pneumatic micro motors [78] may also be an option for driving wheels, tracks, or propellers.

There is also the issue of how the power is transmitted. Some of the various methods used on robotic systems include direct wiring, batteries, and solar power.

The main disadvantage of direct wiring is that it limits the operating range of the microrobot, and may also hinder the motion of the microrobot [74]. There may also be issues with convenience for the end user.

The endoscopic robot discussed in [73] is driven by pneumatic power. The trailing wires required to power the robot may be a source of discomfort to the patient during operation of the system. The invasiveness of the robot could be reduced significantly if an onboard power system were to be used to eliminate the trailing wires.

The most apparent way to overcome this issue is through the use of onboard power storage, i.e. a battery. The main drawback to this technology is that the amount of power a battery can store is proportional to the volume of the battery [79].

Although batteries are able to eliminate many of the problems associated with direct wiring, the operating life of the microrobot will be significantly reduced since most batteries on the centimetre and millimetre scale cannot store the amount of energy required to operate the system actuators over an extended period of time.

Solar-powered robots have shown some promise. In [80], 90 solar cells spread out over a 2 square millimeter area are able to produce 100 microwatts of power, which is more than sufficient to power the simple robotic design discussed in the paper.

Similarly, in [81] a solar array is used to generate a 100(V) power supply, which is theoretically capable of driving many of the propulsion systems described above but has yet to be implemented on a microrobotic system.

Solar power is not without its disadvantages, one example being that it would be impossible for a robot operating in the human body to receive any sort of power from this method. Further complicating matter is that the propulsion system will not be the only onboard system requiring power. There will also be actuators and communication equipments that will require a power source to operate.

One effective method of microrobotic propulsion that has shown a great deal of promise is the use of a magnetic propulsion system.

1.2.9. Magnetic Propulsion

The primary benefit of magnetic propulsion systems is that the magnetic field is produced external to the microrobot, and the locomotive power is transmitted “wirelessly” through the interaction between the magnetic field and magnetic object [82]-[83].

Mathieu et. al. [84]-[87] reported the use of a magnetic resonance imaging (MRI) system to propel a ferromagnetic core. The concept was studied for future development of micro devices designed to perform minimally invasive interventions in remote sites accessible through the human cardiovascular system. The results indicated that with the technology available today for gradient coils used in clinical MRI systems, it is possible to generate sufficient gradients to propel a ferromagnetic sphere in the larger sections of the arterial system.

Miki and his colleagues [88] utilized Gd-Ba-Cu-O bulk high temperature superconductors (HTS) in pole-field magnets in an axial-gap type rotating machine. The HTS magnets are assembled on the rotor plates and cooled down with a liquid cryogen supplied via a rotary joint. This technique implies the possibility of smaller and lighter rotating motors or generators with a HTS bulk magnet for a sub-megawatt class propulsion system.

Ohashi et. al. [89]-[90] developed two magnetically levitated conveyance systems. The first system [89] is a hybrid magnetically levitated device in which pinning force of high temperature bulk super conductor is used for the levitation and guidance. This system needs no control rule for levitation and guidance. To increase levitation force, repulsive force of the permanent magnet is used.

In the second system [90], a combined levitation and propulsion system is proposed. The source of the magnetic force is a two phase linear motor. Modulation of the voltage applied on the primary windings is generating the propulsion force and traveling field effects generate the levitation force. Experimental results showed that this system realizes contact-less conveyance with various propulsion patterns.

The magnetic propulsion system is highly suitable for micromanipulation tasks. If the magnetic propulsion range is increased, remote teleoperation of levitated objects and microrobots can be realized.

Khamesee and his colleagues [91]-[97] proposed a large gap magnetic levitation/propulsion system suitable for teleoperation. Their proposed device comprises several electromagnets installed on a yoke shaped ferromagnetic material. All the electromagnets' poles are connected to a single part called pole piece. The combination of electromagnets, pole piece and yoke is called magnetic drive unit (MDU) which in fact is the stator of the system.

The rotor can be either a small permanent magnet or a microrobot freely levitated and moved within the air gap between the two yoke ends. The distance between the levitated object and the electromagnets can get up to 20(cm) which is very large compared with the available magnetic propulsion systems in the literature. The proposed system has reported a traveling range of 30x30x30(mm^3) for the levitated object.

Khamesee has also shown the practical performance of this system in light pick-and-place operations using a levitated microrobot. The microrobot is equipped with a gripper that is designed to grasp objects within the workspace.

Such grippers are typically manufactured from bimorphic materials such as shape memory alloys [98]-[102] and piezoelectric materials [103]-[108]. The general characteristic of these materials is that they will deform when energized by a current and will return to their original shape when the current is removed.

The interesting aspect of such materials is their high force to weight ratio as well as their simple operation making them very good candidates for micro gripping applications.

The workspace of the system does not necessarily have to be planar, since the microrobot is capable of motion in all three cardinal directions. The large spatial separation between the magnetic drive unit and the microrobot allows for the microrobot to operate in an enclosed space, separate from the rest of the environment. This would be useful for applications in semiconductor industry, such as wafer transportation or photolithography. It would also be useful in pharmaceutical or biomedical research, both to minimize environmental contaminants or to protect the operator from potentially hazardous chemicals.

In all of these cases, the isolation of the magnetic drive unit from the clean room area means that it would not have to be decontaminated between work operations. Multiple robots are used so that, while one robot is being cleaned, the other robot is put into service, reducing down time. If the cost of the microrobot can be kept within a low acceptable range, it could even be disposed of after use.

1.3. Thesis Objective and Scope

The subject of this thesis is based on the application of magnetic actuation in telemanipulation. This thesis is aiming to design a large gap magnetic levitation system capable of three dimensional positioning of an object with ultra precise positioning accuracy.

Through the course of this thesis, a new large gap magnetic levitation system was completely designed, fabricated and successfully tested in several experiments. This process involved several steps including finite element analysis and structural design of the parts, coil design, dynamic system modeling, instrument selection, interfacing and controller design for the system.

This work is organized as follows:

Chapter 1 presents a brief overview on the magnetic actuation methods and their applications in industrial devices. Large gap magnetic levitation is presented as a feasible solution for several microrobotic applications including clean room pick and place operations and drug delivery. The thesis objectives and scope are also presented.

Chapter 2 presents a brief introduction on the electromagnetic field formulation for magnetostatic case. Also, an overview on the calculation of the magnetic force experienced by a small permanent magnet in an external magnetic field is presented and the finite element formulation of magnetostatics case is addressed.

Chapter 3 provides the details of the magnetic drive unit (MDU) design and simulation. The formulation for calculating the magnetic field of a current carrying coil is introduced and the optimal design of the electromagnets for less power consumption is addressed. The design criteria of pole piece and yoke are also presented.

Chapter 4 presents the various components of the experimental setup and their performance characteristics. The properties of the yoke, pole piece and electromagnets are provided and the theoretical accuracy of the system inputs and outputs are investigated. Details of the power amplifier, laser sensors, levitated objects and the control software are also presented.

Chapter 5 discusses the method to derive the dynamic model of the magnetic force experienced by the levitated object. The magnetic force is produced by the magnetic drive unit. The proposed method uses the frequency response identification of the comprising components of the magnetic levitation system including the power amplifier and coils. As a result, a compact and accurate magnetic force model is derived which takes the hysteresis and inductance effects into account.

Chapter 6 addresses the closed loop position control of the levitated object in the vertical direction. Several control strategies are presented including PID, feed forward and feedback linearization controllers. Performances of the controllers are compared through the step response and ramp response characteristics. The levitated object in this chapter is a small cylindrical permanent magnet with a constant mass.

Chapter 7 uses the controller design results of Chapter 6 and presents an adaptive control strategy for vertical position control of the microrobot. The controller presented in this chapter is capable of adapting itself with uncertainties in the mass of the levitated object. The performance of the adaptive controller is investigated for a situation in which the weight of the levitated microrobot is increased up to 30 percent of its original weight.

Chapter 8 presents the three dimensional control of the levitated object. The response of levitated object is investigated in following step commands. The performance of the levitated object is also investigated as it traces two circular and spiral trajectories in the horizontal plane.

Chapter 9 provides a mathematical model capable of estimating the maximum point of magnetic field in any given horizontal plane within the working range of the levitation system. Experimental verifications showed that the proposed model is capable of predicting the maximum point of magnetic field with less than 8% error.

Chapter 10 presents the conclusions and recommendations of this thesis. So far, this research has resulted in the publication of 5 journal articles in well-known scientific societies such as IEEE Transactions on Magnetics, Journal of Mechatronics and Journal of Applied Physics. Also, 3 conference papers have been published and two journal articles have been submitted to the Journal of Applied Physics and Journal of Mechatronics. A detailed list of publications related to this research is provided in Appendix A.

Chapter 2

Introduction to Electromagnetics

2.1. Introduction

This chapter presents the governing equations used in the analysis of the magnetic levitation device. In general, there are different types of equations associated with magnetic field related problems. One important concept in the analysis of such problems is the problem classification.

Problem classification is an important concept because the general theory and methods of solution usually apply only to a given class of problems. Categorizing the problem is generally based on such factors as the loads, boundary conditions and solution region.

In the magnetic levitation device, the source of magnetic field is a set of electromagnets where each electromagnet is supplied with an external current source.

The solution region is an interior type meaning that the boundaries of the system are bounded to finite values.

The material used in the design of the magnetic levitation device is a soft magnetic iron with homogeneous magnetic properties meaning that its magnetic properties are not functions of space variables. It is also isotropic i.e. its properties are independent of direction. Moreover, the source of electric energy for the levitation system is a DC power supply and the levitation system is properly grounded meaning that there is no free electric charge available in the system. In addition, as it will be presented in chapter 6, the bandwidth of the levitation system is less than 20 Hz meaning that there is no high frequency current in the system.

Based on these characteristics, the problem of magnetic levitation device analysis is classified as a magnetostatics type. Magnetostatics field theory applies at very low frequencies when the dimensions of the region of interest are small relative to the wavelength of the electromagnetic field that permeates it. For the levitation device, the system resides in a cubic region of free space that measures 1.5(m) on each side. Assume that the system generates a time-harmonic electromagnetic field which propagates across this region with light velocity of $c = 3\times10^{8}\left(m/s\right)$. Therefore, any changes in the field are felt throughout the region within 5 ns. On the other hand, based on the bandwidth of the system, a maximum frequency of 20 Hz can be assumed for the magnetic field meaning that the smallest harmonic period of the field is 50 ms. Therefore the field changes 10^{7} times slower than the time required for it to propagate across the region and hence, the assumption of a magnetostatics formulation is valid.

In this chapter, the governing equations of magnetostatics are presented and method of calculating the magnetic force experienced by a small permanent magnet in an external field is addressed. A detailed introduction on the magnetic field formulation and classification is presented in Appendix B.

2.2. Magnetostatic Fields

Magnetostatic fields are produced due to motion of electric charges with uniform velocity. Magnetostatic formulation is also an accurate approximation even when the currents are not static as long as the currents do not alternate rapidly [109]. The basic laws of such fields are Ampere's law:

$$\oint_{L} \mathbf{H} \cdot d\mathbf{l} = \int_{S} \mathbf{J} \cdot d\mathbf{S} \tag{2-1}$$

Where $d\mathrm{S}$ is the surface element and $d\mathrm{l}$ is the length element. The law of conservation of magnetic flux (also called Gauss's law for magnetostatics) is given as:

$$\oint \mathbf{B} \cdot d\mathbf{S} = 0 \tag{2-2}$$

where $\mathbf{H}$ is the magnetic field intensity (in amperes/meter), $\mathbf{J}$ is the electric current density (in amperes/meter^2) and $\mathbf{B}$ is the magnetic flux density (in tesla or Wb/meter^2).

The differential forms of equation (2-1) and (2-2) are obtained as:

$$\nabla\times\mathbf{H} = \mathbf{J} \tag{2-3}$$

and,

$$\nabla\cdot\mathbf{B} = 0 \tag{2-4}$$

The vector fields $\mathbf{B}$ and $\mathbf{H}$ are related through the permeability μ (in henries/meter) of the medium as:

$$\mathbf{B} = \mu\mathbf{H} \tag{2-5}$$

In terms of the magnetic vector potential $\mathbf{A}$ (in Wb/meter) [110]:

$$\mathbf{B} = \nabla \times \mathbf{A} \tag{2-6}$$

Applying the vector identity for an arbitrary vector $\mathbf{F}$ [110]:

$$\nabla \times (\nabla \times \mathbf{F}) = \nabla(\nabla \cdot \mathbf{F}) - \nabla^2\mathbf{F} \tag{2-7}$$

to Eqs. (2-3) and (2-6) leads to Poisson's equation for magnetostatic fields:

$$\nabla^2\mathbf{A} = -\mu\mathbf{J} \tag{2-8}$$

When $\mathbf{J} = 0$, Eq. (2-8) becomes Laplace's equation:

$$\nabla^2\mathbf{A} = 0 \tag{2-9}$$

In the absence of currents ($\mathbf{J} = 0$), the magnetic flux density $\mathbf{H}$ can be expressed in term of magnetic scalar potential Ψ (in amperes/meter) as [110]:

$$\mathbf{H} = -\nabla\Psi \tag{2-10}$$

The use of magnetic scalar potential reduces the three components of magnetic field $\mathbf{H}$ into one component Ψ making computations easier and more time efficient. Appling Eq. (2-3) on Eq.(2-10) yields:

$$-\nabla \times \nabla\Psi = 0 \tag{2-11}$$

Equations (2-6), (2-8), (2-10) and (2-11) are useful tools in calculation of magnetic field in magnetostatic cases. The magnetic field will be used in the calculation of magnetic force experienced by the levitated object in the levitation device.

In the next section, calculation of the magnetic force experienced by a small permanent magnet in an externally applied magnetic field is presented.

2.3. Magnetic Force

In [110] it is shown that the magnetic force due to an external field $\mathbf{B}$ experienced by a current carrying loop with area of S, current I and the surface normal $\mathbf{n}$ is obtained as:

$$\mathbf{F} = \nabla(\mathbf{p}.\mathbf{B}) \tag{2-12}$$

where, $\mathbf{p}\left(Am^2\right)$ is the dipole moment of the loop and is defined as:

$$\mathbf{p} = IS\mathbf{n} \tag{2-13}$$

In Eq. (2-13), $\mathbf{p}$ is assumed to be constant over the surface of the loop. Khamesee et. al. [91]-[94] showed that for a small permanent magnet, the magnetic dipole moment can be assumed constant over the volume of the magnet and the equivalent magnetic dipole moment for the permanent magnet can be calculated as:

$$\mathbf{p} = \left(\frac{\mathbf{B}_s}{\mu_0}\right) v \tag{2-14}$$

where $\mathbf{B}_s$, μ_0 and v are the magnetic field at the magnet surface, the permeability of the volume $\left(\mu_0 = 4\pi \times 10^{-7}\ \mathrm{H/m}\right)$ and the magnet volume respectively.

Since $\mathbf{B}$ is an externally applied field and is taken outside its generating source, therefore, the Maxwell equation yields that:

$$\nabla \times \mathbf{B} = 0 \tag{2-15}$$

Using Eq. (2-15) and based on the assumption of $\mathbf{p}$ constant, Eq. (2-12) can be written in the Cartesian coordinate with unit vectors $\mathbf{e}_x$, $\mathbf{e}_y$, $\mathbf{e}_z$ as:

$$\mathbf{F} = \left[\mathbf{p}.\left(\frac{\partial \mathbf{B}}{\partial x}\right)\right]\mathbf{e}_x + \left[\mathbf{p}.\left(\frac{\partial \mathbf{B}}{\partial y}\right)\right]\mathbf{e}_y + \left[\mathbf{p}.\left(\frac{\partial \mathbf{B}}{\partial z}\right)\right]\mathbf{e}_z \tag{2-16}$$

From Eq. (2-16) it is clearly inferred that the amount of the magnetic force in each direction is in direct relationship with the gradient of the externally applied magnetic field in that direction. Therefore, increasing the gradient of the field will result in an increase in the magnetic force. This is one of the key design considerations when designing magnetic actuation systems. It can be shown that the torque experienced by a magnetic dipole moment $\mathbf{p}$ in an externally applied field $\mathbf{B}$ is [110]:

$$\mathbf{T} = \mathbf{p} \times \mathbf{B} \tag{2-17}$$

Equation (2-17) shows that a permanent magnet with dipole $\mathbf{p}$ tends to rotate so as to align its moment $\mathbf{p}$ to field $\mathbf{B}$, thereby acquiring its minimum potential energy.

In general, the solution of the field equations for complex geometries such as the magnetic levitation unit is a complicated task and is performed through numerical methods. In the next section, the finite element technique is presented as an accurate method in solving the governing equations of magnetic fields.

2.4. Introduction to Finite Element Method

This section introduces the finite element method (FEM) as a tool for solution of magnetostatic problems. In this method, the solution region is discretized into simple geometric shapes called finite elements. For each element, a stiffness matrix is calculated so as to relate the material properties and applied loads to the values at the nodes of the element as:

$$\left[\mathbf{K}^{e}\right][\mathbf{x}]=[\mathbf{f}] \tag{2-18}$$

where, $\left[\mathbf{K}^{e}\right]$ is the element stiffness matrix, $[\mathbf{x}]$ is the vector of unknown nodal values and $[\mathbf{f}]$ is the element's force vector. The element stiffness matrix depends on the geometry and properties of the element. For each type of problem, i.e. magnetic, structural or thermal, a specific element stiffness matrix has to be used.

The element stiffness matrices will all be inserted into a global stiffness matrix $\left[\mathbf{K}^{G}\right]$ which relates all the unknown nodal values of the solution domain to the applied loads, and material properties as:

$$\left[\mathbf{K}^{G}\right][\mathbf{X}]=[\mathbf{F}] \tag{2-19}$$

where $[\mathbf{X}]$ is the global unknown nodal values and $[\mathbf{F}]$ is the global force vector.

In magnetic problems, the two most common solution types are the magnetic scalar potential and the magnetic vector potential. As stated earlier in this chapter, the magnetic scalar potential is suitable for the solution domains in which there is no external source of current density available. On the other hand, the magnetic vector potential solution is suitable for the cases in which there is an external current density available in the solution domain.

For the analysis of magnetic levitation systems, the source of the magnetic field is the external current density in the electromagnets and thus the magnetic vector potential formulation is used. In the next section, with the aid of finite element analysis, the design of the magnetic drive unit is addressed.

Chapter 3

Design of the Magnetic Drive Unit

3.1. Introduction

In this chapter the details of the magnetic drive unit (MDU) design and simulation are provided. The MDU is responsible for generating a controllable magnetic field distribution within the air gap. A proper design of the MDU will significantly increase the performance of the levitation system, including its range of motion.

The MDU consists of three main sections; electromagnets, pole piece and yoke. Electromagnets are the heart of the MDU in the sense that they receive the electric energy from an external power source and generate an electromagnetic field. Since one electromagnet cannot provide a three dimensional control on the magnetic field, several electromagnets should be used in the MDU. The pole piece is a part made of ferromagnetic material and connects the electromagnet poles together. Existence of the pole piece is necessary as it increases the controllability of the system on the distribution of the magnetic field. The yoke is also made of soft magnetic iron and is used to generate a closed loop magnetic signal. This will increase the intensity and gradient of the magnetic field within the air gap as the higher gradient of the magnetic field will result in a larger magnetic force.

In order to design the MDU, all the components have to be designed separately. Once the components are designed, the overall performance of the system should be analysed to assure the satisfactory performance of the MDU. In the following sections, the design procedure of the electromagnets, pole piece and yoke is presented.

3.2. Electromagnet Design

An electromagnet consists of many magnetic dipoles stacked on top of one another.

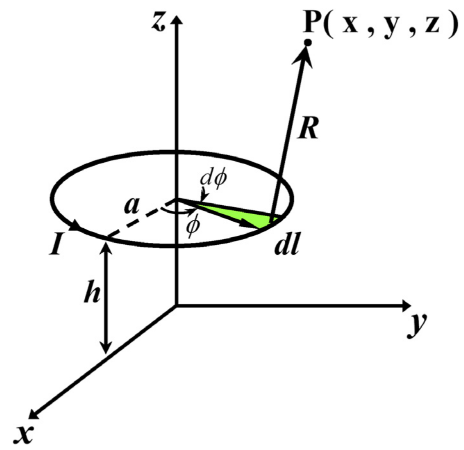

Figure 3-1: Calculation of magnetic flux density generated by a current carrying loop.

Figure 3-1 illustrates a current carrying loop of radius a at height h above the horizontal plane. In the Cartesian coordinate, the elemental section $d\mathbf{l}$ of the loop is expressed as:

$$d\mathbf{l} = a\left(-\sin\phi\,\mathbf{i} + \cos\phi\,\mathbf{j} \right) d\phi \tag{3-1}$$

Therefore, vector $\mathbf{R}$ is obtained as:

$$\mathbf{R} = \left(x - a\cos\phi\right)\mathbf{i} + \left(y - a\sin\phi\right)\mathbf{j} + \left(z - h\right)\mathbf{k} \tag{3-2}$$

where $\mathbf{i}$, $\mathbf{j}$ and $\mathbf{k}$ are the Cartesian unit vectors in the x, y and z directions respectively. Thus, the magnetic flux density $\mathbf{B}$ at point $p\left(x, y, z\right)$ is obtained as [110]:

$$\mathbf{B}\left(p\right) = \frac{\mu_0}{4\pi}\int_c \frac{I\,d\mathbf{l}\times\mathbf{R}}{\left|\mathbf{R}\right|^3} = \frac{\mu_0 m}{4\pi^2 a}\int_0^{2\pi} \frac{\left(-\sin\phi\,\mathbf{i} + \cos\phi\,\mathbf{j}\right)\times\mathbf{R}}{\left|\mathbf{R}\right|^3} d\phi \tag{3-3}$$

where μ_0 is the permeability of the free air, subscript c indicates integration over a closed path and m is the magnetic dipole moment of the loop and is defined as:

$$m = \pi I a^2 \tag{3-4}$$

Now assume that a solenoid with length L, radius a and current I is wound in such a way that there are N turns of wire per unit length of the solenoid. For a filamentary element dz as shown in Figure 3-2, the number of turns is calculated as:

$$N_{dz} = N\,dz \tag{3-5}$$

Thus, the magnetic dipole moment for this element can be obtained as:

$$m_{dz} = NI\pi a^2\,dz = N\,m\;dz \tag{3-6}$$

By replacing m with m_{dz} in Eq.(3-3), the magnetic flux density at point $p(x,y,z)$ due to the filamentary element dz can be calculated as:

$$\mathbf{B}_{dz}(p)=\frac{\mu_0 m_{dz}}{4\pi^2 a}\int_0^{2\pi}\frac{(-\sin\phi\ \mathbf{i}+\cos\phi\,\mathbf{j})\times\mathbf{R}}{|\mathbf{R}|^3}d\phi \tag{3-7}$$

By integrating over the length of the solenoid, the total solenoidal magnetic flux density at point $p(x,y,z)$ is calculated as:

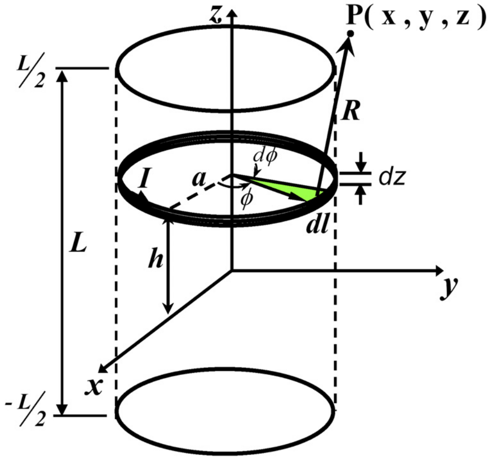

Figure 3-2: Calculation of magnetic flux density generated by a filamentary current carrying element.

$$\mathbf{B}(x,y,z)=\frac{\mu_0 N m}{4\pi^2 a}\int_{-L/2}^{L/2}\int_0^{2\pi}\frac{(-\sin\phi\,\mathbf{i}+\cos\phi\,\mathbf{j})\times\mathbf{R}}{|\mathbf{R}|^3}d\phi\ dz \tag{3-8}$$

For multi layered coils with inside radius r_{in}, outside radius r_{out} and a winding density of σ wires per unit area, the magnetic dipole moment for a filamentary element of radius r, thickness dr and height dz is defined as:

$$m_{\upsilon}=\sigma I\pi r^2\,dr\,dz \tag{3-9}$$

Therefore the magnetic flux density at point $p(x,y,z)$ is obtained as:

$$\mathbf{B}(x,y,z)=\frac{\mu_0\sigma I}{4\pi}\int_{r_{in}}^{r_{out}}\int_{-L/2}^{L/2}\int_0^{2\pi}\frac{r(-\sin\phi\,\mathbf{i}+\cos\phi\,\mathbf{j})\times\mathbf{R}}{|\mathbf{R}|^3}d\phi\,dz\,dr \tag{3-10}$$

where $\mathbf{R}$ is defined by replacing a in Eq.(3-2) with r. Increasing the current in the coil will generate a counter electromotive force (EMF) which opposes the electrical current change in the coil. The emf is defined based on Faraday's law and is obtained as [110]:

$$Emf = -\mathrm{L}\frac{dI}{dt} \tag{3-11}$$

where L is the inductance of the coil and is defined as:

$$\mathrm{L} = \frac{\mu N^2 A}{l} \tag{3-12}$$

in which l is the total length of the coil, μ is the relative permeability of the core material, and N and A are the number of turns and the cross section area respectively.

Basically, in designing the electromagnets for the MDU, one of the objectives of the design is to minimize the inductance of the coils since the inductance will oppose the direction of current flow in the coils.

On the other hand, another design objective for the coils is to maximize the amount of magnetic field that each coil can generate. As inferred from Eq. (3-10) increasing the number of wires in the electromagnet, will increase the winding density σ which eventually increases the magnetic flux density of the coil. However, this will also increase the inductance of the coil as inferred from Eq. (3-12).

Therefore, an optimal design should be selected for the electromagnets. In the next section, optimal design of the electromagnets is presented.

3.3. Optimal Geometry design of the Electromagnets

The optimization objective in the coil design is selected to be the power consumption. In other words, for a fixed intensity of magnetic field, the optimal coil will consume the least electrical energy.

The selection of the energy consumption as the optimization target will minimize the power dissipation hence temperature variation in the MDU. This will guarantee the least variations in the physical properties of the system as a result of thermal drift. The main parameters in the design of the coil are the internal and external radii as well as the coil length.

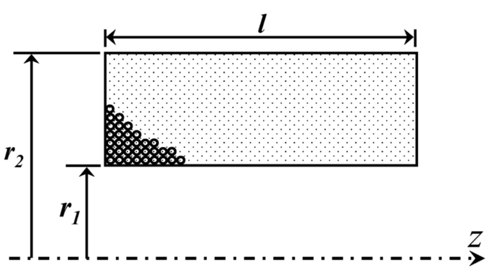

$$\alpha = \frac{r_2}{r_1} \quad , \quad \beta = \frac{l}{2r_1}$$

Figure 3-3: Geometry definition of a coil.

Figure 3-3 illustrates the geometry of a coil. Using the basic electrical formulas for the electric power consumption in a resistive element, the power dissipation in the coil can be written as:

$$W = \int dW = j^2 \rho \int dV \tag{3-13}$$

where $j\left(A/cm^2\right)$ is the current density in the conductor part of the coil and $\rho\left(\Omega \cdot cm\right)$ is resistivity.

By defining λ as the active section of winding divided by the total section of winding, the power can be obtained as [112]:

$$W = j^2 \rho \lambda r_1^3 2\pi\beta\left(\alpha^2 - 1\right) \tag{3-14}$$

From Eq. (3-14), j can be expressed as:

$$j = \left[\frac{1}{2\pi\beta(\alpha^2 - 1)}\right]^{\frac{1}{2}} \left(\frac{W}{\rho\lambda r_1^3}\right)^{\frac{1}{2}} \tag{3-15}$$

Using Eq. (3-10), the magnetic flux at the center of the coil is calculated as:

$$H_0 = j\lambda r_1 \frac{4\pi\beta}{10} \ln \frac{\alpha + \sqrt{\alpha^2 + \beta^2}}{1 + \sqrt{1 + \beta^2}} \tag{3-16}$$

A “field factor” can be defined as:

$$F\left(\alpha, \beta\right) = \frac{4\pi\beta}{10} \ln \frac{\alpha + \sqrt{\alpha^2 + \beta^2}}{1 + \sqrt{1 + \beta^2}} \tag{3-17}$$

Using Eq. (3-16), the conductor current density j can be calculated as:

$$j = \frac{H_0}{r_1 \lambda F(\alpha, \beta)} \tag{3-18}$$

By substituting (3-18) in Eq. (3-14) and doing some algebraic operations, the magnetic field in terms of the power consumption is expressed as:

$$H_0 = \frac{F(\alpha,\beta)}{\sqrt{2\pi\beta(\alpha^2-1)}}\left(\frac{W\lambda}{\rho r_1}\right)^{\frac{1}{2}} \tag{3-19}$$

Combining all the geometric terms of Eq. (3-19) into a single factor called the “Fabry factor” or “G-factor”, Eq. (3-19) can be rewritten as:

$$H_0 = G(\alpha,\beta)\left(\frac{W\lambda}{\rho r_1}\right)^{\frac{1}{2}} \tag{3-20}$$

where,

$$G(\alpha,\beta) = \frac{1}{5}\left(\frac{2\pi\beta}{\alpha^2-1}\right)^{\frac{1}{2}} \ln\frac{\alpha+\sqrt{\alpha^2+\beta^2}}{1+\sqrt{1+\beta^2}} \tag{3-21}$$

As inferred from Eq. (3-20), for a constant value of magnetic field intensity H_0, the minimum power consumption W is obtained by maximizing the Fabry factor $G(\alpha,\beta)$. Figure 3-4 demonstrates the value of the Fabry factor for a uniform current density coil.

As seen in this figure, the maximum Fabry factor is $G = 0.179$ which happens in the vicinity of $\alpha = 3$ and $\beta = 2$. In other words, a coil of $\alpha = 3$ and $\beta = 2$ will be optimal from the power consumption point of view.

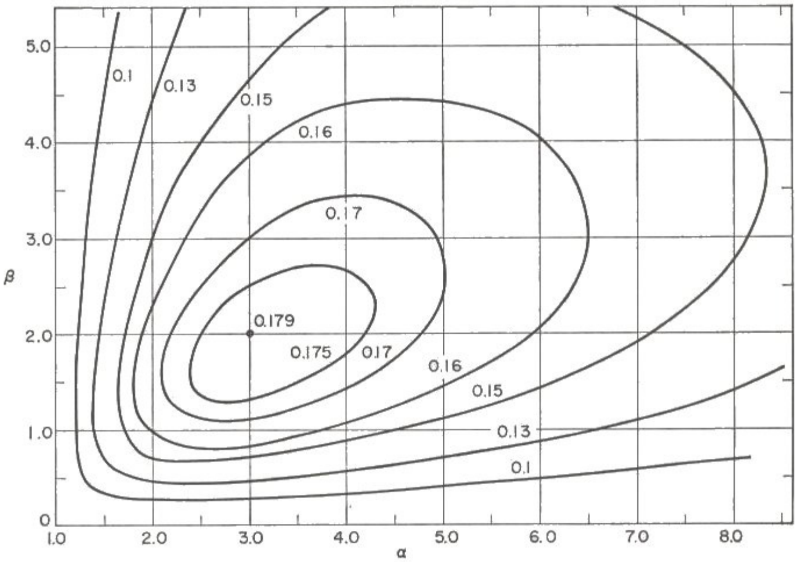

Figure 3-4: The value of Fabry factor for a uniform current density coil [112].

The fabricated coils have the inside diameter of $r_1 = 0.01(m)$, outer diameter of $r_2 = 0.02(m)$ and length of $l = 0.04(m)$. The approximate Fabry factor of each electromagnet is $G = 0.165$. Each electromagnet has approximately 840 turns of #22 AWG wire.

3.4. Pole Piece Design

As mentioned earlier, the pole piece is made from soft magnetic iron and connects the poles of the electromagnets together. The magnetic field from the electromagnets will magnetize the pole piece.

Due to the induced magnetization, the pole piece changes the distribution of the magnetic field in the air gap. Due to the magnetization nonlinearity, magnetic flux leakage and sharp edge effects at the corners of the pole piece, in general there is no theoretical method capable of accurately calculating the pole piece effect [113]-[114].

The governing equation for analysing the pole piece effect is the Poisson's equation for magnetostatic fields as:

$$\nabla^2 \mathbf{A} = -\mu \mathbf{J} \tag{3-22}$$

where $\mathbf{J}\left(A/m^2\right)$ is the external electric current density.

As mentioned in the previous chapter, Eq. (3-22) should be solved for the magnetic vector potential $\mathbf{A}$ subject to the boundary conditions and loads applied to the solution domain. In general, the most common technique in solving this equation is the finite element (FE) method.

The objective of the pole piece design process is to maintain controllability over the distribution of magnetic field. Since the levitated object is moving towards the maximum point of magnetic field, an important factor in the design of the pole piece is the ability of the pole piece to shift the position of the maximum point of magnetic field within the working envelope of the system.

The working envelope is defined as a vertical range within the air gap in which 3D levitated movement can take place. Since a single electromagnet cannot control the distribution of the magnetic field in a horizontal plane, one must employ multiple electromagnets. However, multiple electromagnets will generate a magnetic field distribution with multiple peaks in the magnetic field.

Figure 3-5 illustrates the qualitative pole piece performance for a simple system with two identical electromagnets.

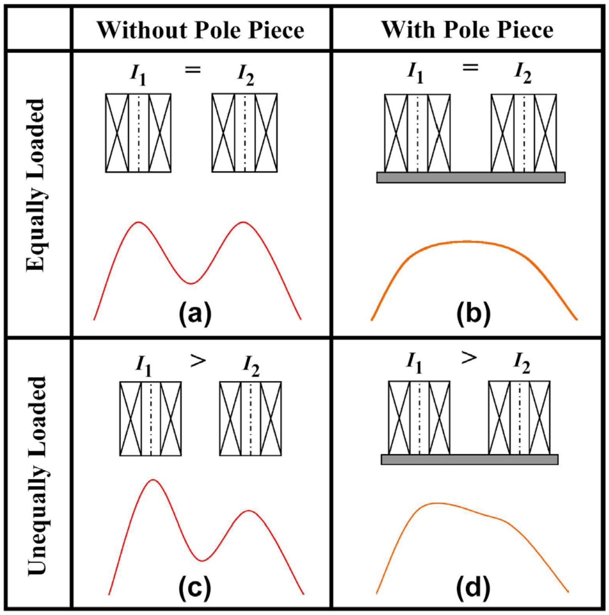

Figure 3-5: Demonstration of the qualitative performance of pole piece.

As Figure 3-5(a) shows, when the electromagnets are energized with identical currents, the distribution of the magnetic field in the vertical direction will have two peaks below the electromagnets. However, for our particular application, the resultant vertical field induced by the electromagnets must be configured in such a way that only one magnetic peak exists within a horizontal plane below the coils.

In this way, feeding the electromagnets with identical currents would bring this magnetic peak below the centre of the pole piece. Therefore, the levitated object will be levitated below the center of the pole piece. This is achieved by proper design of the pole piece.

As shown in Figure 3-5(b), in the presence of the pole piece, the maximum point of the magnetic field for equally loaded coils will be a unique point below the centre of the pole piece. The position of the maximum B point (B_{max} point) is controlled by tuning the electrical currents in the electromagnets.

As demonstrated in Figure 3-5(c), increasing the electrical current in the left electromagnet i.e. I_1, the left magnetic peak will go higher than the right magnetic peak. However, for the position control of the levitated object, we have to be able to shift the location of the magnetic peak in horizontal directions. Figure 3-5(d) shows how pole piece will combine the magnetic peaks into a focal point of magnetic field closer to the stronger coil. In fact, in the presence of the pole piece, increasing the current in one coil will shift the magnetic peak towards that coil.

Each pole piece has a specific operating range. In other words, each pole piece can generate a unique $\mathrm{B}_{\mathrm{max}}$ point within a limited range below the pole piece. At distances too close to the pole piece, the magnetic field is uneven with multiple maximum points, and at points far from the pole piece the magnetic field is too weak.

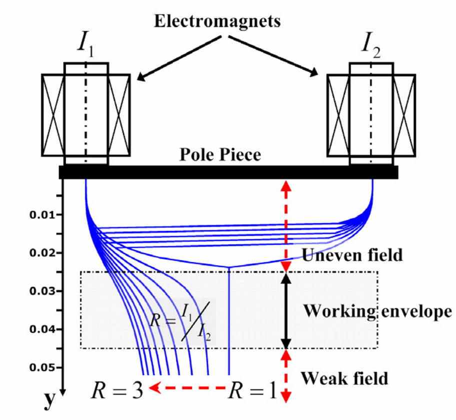

Figure 3-6: Definition of the working envelope according to $\mathrm{B}_{\mathrm{max}}$ lines.

Figure 3-6 shows the concept of the change in the location of $\mathrm{B}_{\mathrm{max}}$ point when the current ratio is changed. The example system shown in this figure is composed of two identical electromagnets and a bar pole piece. R is the current ratio and is defined as the ratio between the electrical currents I_1 and I_2 in the left and right electromagnets. The lines in the figure indicate the geometrical position of $\mathrm{B}_{\mathrm{max}}$ points for different R ratios. The y is defined as the vertical distance under the pole piece and is expressed in meters.

Between y values of 0 and 0.025(m), multiple magnetic poles exist. Thus, the system has no control on the position of the maximum point of magnetic field. Also, when y is greater than 0.045(m), the magnetic field is too weak to lift an object. This limits the working envelope to the range $y \in [0.025, 0.045]m$ where there exists only one B_{max} point on each horizontal plane. Since the levitated object tends to stay at this B_{max} point, motion of the magnet can be achieved by shifting the location of the B_{max} point. This allows for accurate levitation and positioning.

In practice, due to the complexity of calculations, the working envelope boundaries are found experimentally or through finite element analysis. Based on the pole piece design criteria mentioned in this chapter, several finite element models were established and the performance of the pole piece profiles for different current ratios fed to the coils were analyzed. The final design was selected as a disk shaped pole piece with seven identical electromagnets installed on its top. The details of the experimental setup will be provided in the experimental setup section.

3.5. Yoke Design

The yoke is made of soft magnetic iron and is used to generate a closed loop magnetic circuit. This part increases the magnetic field intensity and gradient in the working envelope. Moreover, the yoke is responsible for aligning the magnetic field lines with the vertical direction. Since the weight of the levitated object results in a force in the vertical direction, alignment of the magnetic field lines with the vertical direction will result in a higher magnetic force opposite to the weight of the object.

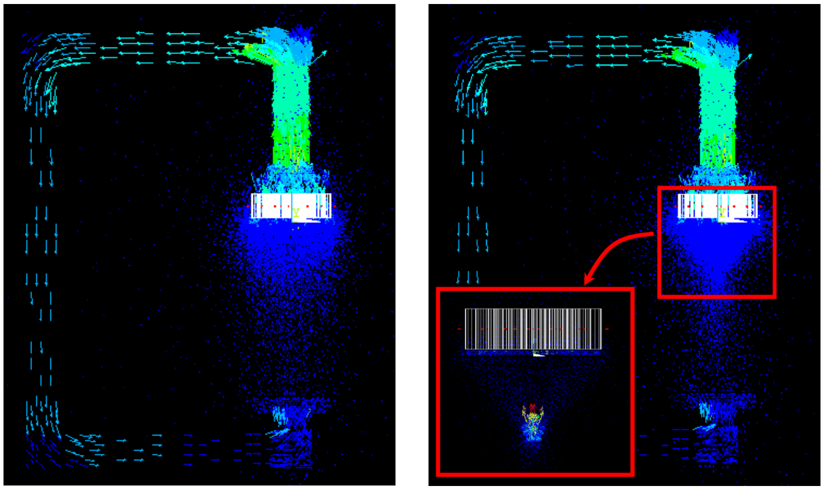

a) With no levitated object. **b) With levitated object.**

Figure 3-7: Schematic of the magnetic flux distribution in the levitation system.

Figure 3-7 shows the simulation results for the effect of yoke in increasing the magnetic flux density in the air gap. Although the yoke design is not complicated, there are a few factors that must be considered in the design process. Figure 3-8 shows a schematic view of the pole piece connected to the yoke. The dimensions of the yoke have important effects on the orientation of the magnetic field inside the gap.

Finite element simulations illustrated that for small values of l_a and l_d, the magnetic field inside the gap is inclined towards the yoke middle part i.e. the lateral flux leakage will be increased.

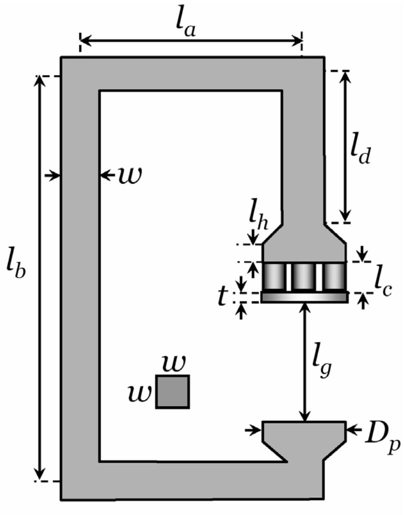

Figure 3-8: Schematic view of a yoke and a pole piece.

A simple approach in obtaining an estimate of the pole piece sizing can be followed by the application of the magnetic resistant method [110]. Based on this method, the total flux is modelled as the electrical current passing through an arrangement of resistors. Each resistor, represent a particular material in the field and the current in the resistor represents the flux passing through that material.

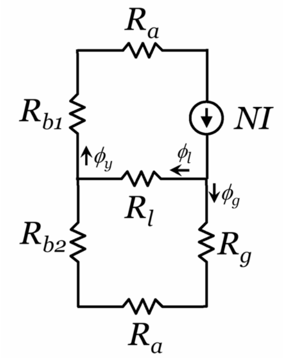

Figure 3-9: Resistor model of the yoke.

Figure 3-9 shows the resistor model of the yoke system. In this figure, R_g represent the resistance of the gap between two yoke ends. Also R_l represents the resistance between the pole piece and the internal yoke part. N is the total number of wire turns, I is the current in the coils and ϕ is the magnetic flux with the SI unit of weber (wb).

If the yoke is designed in such a way that R_l is relatively higher (more than 5 times) than R_g, this will guarantee a high ratio of ϕ_g/ϕ_l. Therefore, the amount of undesired flux leakage to the internal yoke parts will be less than 20% of the total flux. The values of R_l and R_g are approximated as [110]:

$$R_l = \frac{l_a}{\mu_0 A_l} \tag{3-23}$$

and,

$$R_g = \frac{l_g}{\mu_0 A_g} \tag{3-24}$$

where, A_l and A_g are the flux penetration surfaces and μ_0 is the permeability of the air. Approximations of these two surfaces can be assumed as [110]:

$$A_l = (l_c + t)w \tag{3-25}$$

$$A_g = \frac{\pi D_p^2}{4} \tag{3-26}$$

Where D_p is the diameter of the pole piece as shown in Figure 3-8. Using the circuit analysis rules, the ratio between the desired and undesired flux leakages is obtained as:

$$\frac{\phi_g}{\phi_L} = \frac{R_l}{R_g + R_a + R_{b2}} \tag{3-27}$$

where, R_{b2} and R_a are obtained as:

$$R_{b2} = \frac{l_b - l_d}{\mu_0 \mu_r w^2} \tag{3-28}$$

$$R_a = \frac{l_a}{\mu_0 \mu_r w^2} \tag{3-29}$$

In Eq. (3-28), μ_r refers to the relative permeability of the iron and is selected as $\mu_r = 4000$. For the design purposes, the value of w was selected from the available iron sheet thicknesses in the market as $w = 2.5(in) = 6.35(cm)$.

The choice of w was based on the heavy weight of parts comprising the pole piece. Selection of a small w will result in a reduction in the structural stiffness of the yoke. Moreover if the w is small, the yoke will experience magnetic saturation.

The diameter of the pole piece was selected as a function of the outer electromagnets' diameter. Figure 3-10 illustrates the layout of the pole piece and electromagnets. As it is inferred from this figure, in order for the pole piece to cover all the electromagnets, its diameter should be slightly over three times the diameter of the electromagnet.

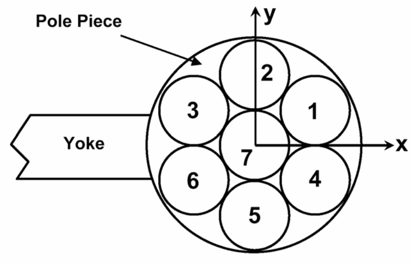

Figure 3-10: Layout of the pole piece and electromagnets.

The outer diameter of each electromagnet is 4.2(cm) leading to the pole piece diameter selection of $D_p = 13.2(cm)$.

An initial leakage of 15% was allowed for the design of the yoke geometry leading to calculation of one possible yoke parameter set as:

$$\begin{bmatrix} L_a & L_b & L_c & L_d & L_g \end{bmatrix} = \begin{bmatrix} 0.45 & 0.72 & 0.04 & 0.24 & 0.28 \end{bmatrix}(cm) \tag{3-30}$$

Issues such as structural stiffness of the yoke and adaptability of the system with different sizes of coils and pole piece profiles were taken into account during dimension selection of the yoke.

For the design check, a fully operational system utilizing 24 electromagnets in the yoke system was considered. In the highest operational capacity, the maximum electrical current in each coil will be 3.5(A).

Using the electrical circuit rules, from Figure 3-9, the magnetic flux ϕ_y in the yoke is calculated as:

$$\phi_y = \frac{NI}{\dfrac{R_l\left(R_g + R_a + R_{b2}\right)}{R_l + R_g + R_a + R_{b2}} + R_a + R_{b1}} \tag{3-31}$$

where,

$$R_{b1} = \frac{l_d}{\mu_0 \mu_r w^2} \tag{3-32}$$

Using the numerical values of Eq. (3-30), $w = 0.0635(m)$, $N = 24\times 840$ and $I = 3.5(A)$, the magnetic flux in the yoke is calculated as $\phi_y = 0.0048(wb)$. Therefore the magnetic flux density in the yoke, B_y, is calculated as:

$$B_y = \frac{\phi_y}{w\times w} = 1.18\left(T\right) \tag{3-33}$$

Since the soft ferromagnetic iron reaches the magnetic saturation at approximately 2.2(T) [109], the size selection of the yoke ensures that under no condition, the system will experience saturation.

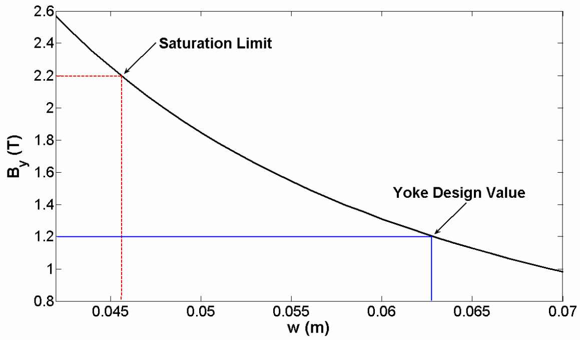

Figure 3-11: Relationship between the yoke thickness w and magnetic flux B_y in the yoke.

Figure 3-11 illustrates the approximate relationship between the yoke thickness w and magnetic flux density B_y in the yoke. As seen in this figure, the selected dimensions of the yoke provide a wide safety margin to avoid saturation in the system.

In order to demonstrate the effect of yoke on the distribution of the magnetic field, some simulation results are presented. Figure 3-12 provides a comparison between the vertical fields generated with and without the use of a yoke. The plots of this figure are obtained from finite element simulations of a system consisting of seven equally loaded electromagnets and a disk pole piece.

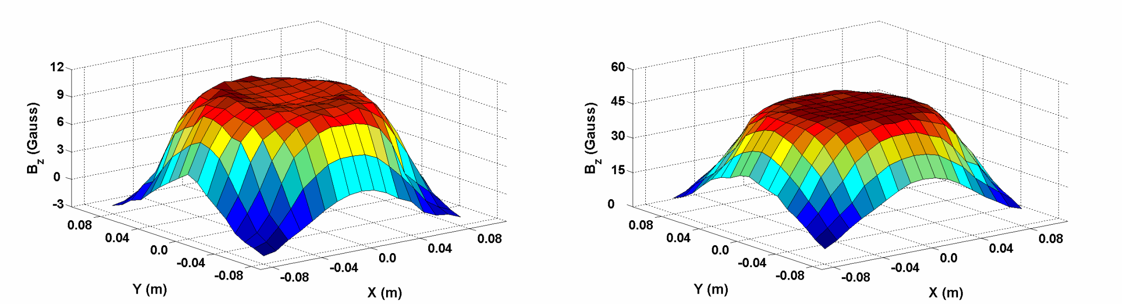

a) Without yoke.

b) With yoke.

Figure 3-12: The effect of yoke on an equally loaded disk pole piece with seven electromagnets.

As seen in Figure 3-12, the magnetic flux density generated in the presence of the yoke is up to five times higher than the magnetic flux density generated without the yoke.

For the cases that the currents fed to the coils are not equal i.e. unequally loaded cases, the yoke will increase the horizontal gradient of the magnetic field towards the maximum point of magnetic field. This will eventually increase the magnitude of the horizontal force on the levitated object and utilize its horizontal movement.

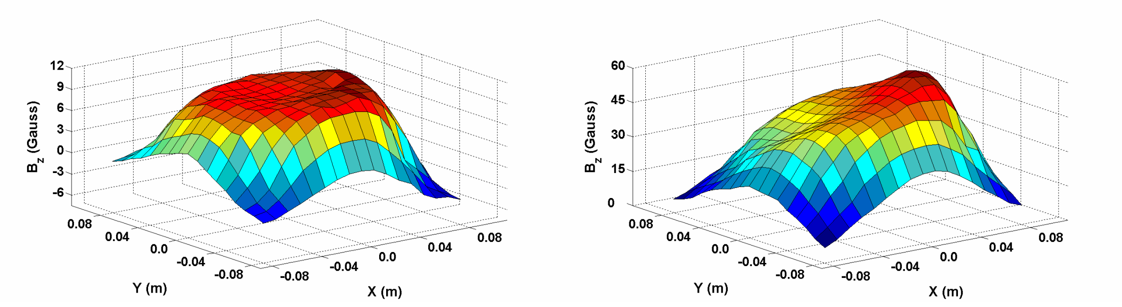

a) Without yoke.

b) With yoke.

Figure 3-13: The effect of yoke on an unequally loaded disk pole piece with seven electromagnets.

Figure 3-13 shows the simulation results for a system with seven unequally loaded electromagnets and a disk shaped pole piece. The plots of this figure compare the distribution of the vertical magnetic field with and without the presence of yoke. As illustrated in Figure 3-13(b), by introducing the yoke to the system, the horizontal gradient of the magnetic field will significantly increase. This figure shows that in the presence of the yoke, the slope of the magnetic field towards the maximum point of the field is relatively higher compared with the no yoke case. This means higher field gradients in the horizontal direction and eventually higher forces.

In the next section, some experimental performance of the magnetic levitation device is addressed.

3.6. Experimental Performance of the Levitation Device

The actual system's performance in generating a desired distribution of magnetic field, and shifting the maximum point of magnetic field was examined in a set of experiments with the fabricated magnetic levitation device. For this purpose, a robot arm was used to position a gauss meter probe (Model LakeShore LS-421) in the air gap of the yoke and measure the magnetic field distribution. For the first experiment, the distribution of the magnetic field was measured at a normal distance of 0.08(m) below the bottom surface of the pole piece i.e. $z = -0.08(m)$.

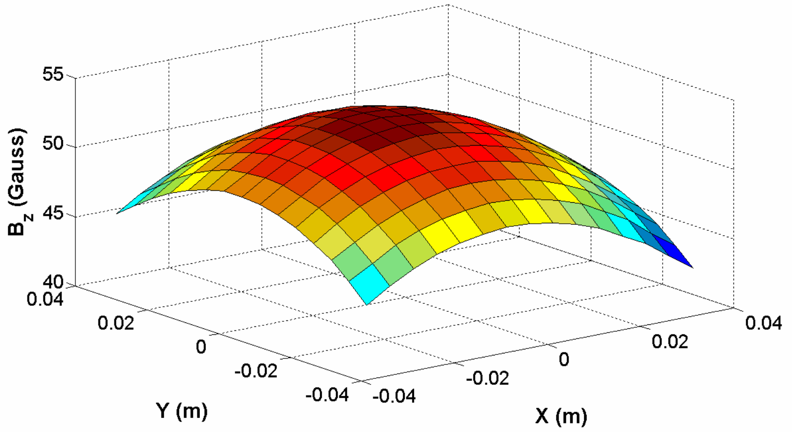

Figure 3-14: Measurement results for 3D distribution of B_z at z=-0.08(m).

$I_1=I_2=I_3=I_4=I_5=I_6=1.5(A), I_7=0$

Figure 3-14 illustrates the three dimensional distribution of B_z on the plane $z=-0.08(m)$. As it can be seen, since all the electromagnets are supplied with an equal amount of current, the maximum point of magnetic field is very close to the centre of the pole piece. This can be better seen in Figure 3-15.

This figure shows the magnetic flux contour and the magnetic flux gradient vectors at the vertical plane of $z=-0.08(m)$. As mentioned in the previous chapter, the gradient of the magnetic field in the vertical direction will result in vertical forces that bring the levitated object to the point of maximum magnetic field.

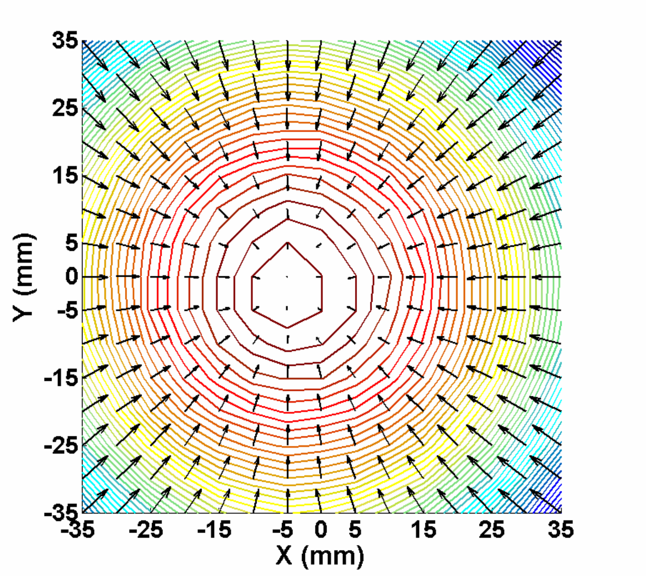

Figure 3-15: Measurement results for 2D distribution of B_z and field gradients at z=-0.08(m).

$I_1=I_2=I_3=I_4=I_5=I_6=1.5(A)$, $I_7=0$

As seen in Figure 3-15, the gradient vectors point towards the centre of the graph i.e. the maximum point of the magnetic field and at the centre, the gradient vectors are zero. This means that the levitated object will be stabilized once it is positioned at the maximum point of the magnetic field.

There is a small shift to the left in the centre of the graph in Figure 3-15. The presence of the yoke on the left side of the y-axis results in a slight shift on the position of the maximum point of magnetic field. However, the amount of this shift is less than 1.5% of the total yoke's width.

In order to investigate the performance of the device in shifting the position of the maximum point of magnetic field, the ratio of the currents was changed in a way to generate a shift along the x-axis.

Figure 3-16 provides the 3D distribution of B_z on the vertical plane $z = -0.06(m)$. As it is seen in this figure, the maximum point of the magnetic field is shifted along the negative direction of the x-axis which is due to the fact that the currents in electromagnets 3 and 6 (Figure 3-10) are higher than the ones in electromagnets 1 and 4.

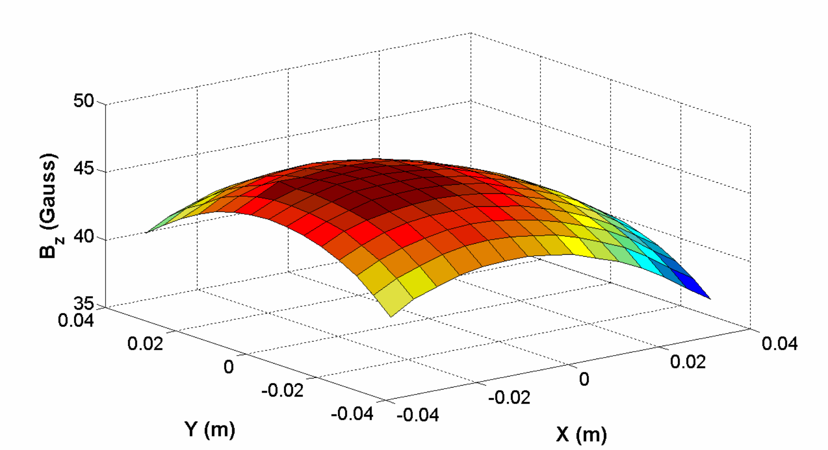

Figure 3-16: Measurement results for 3D distribution of B_z at z=-0.06(m).

I_1=I_4=0.6(A), I_2= I_5=1(A), I_3= I_6=1.4(A), I_7=0

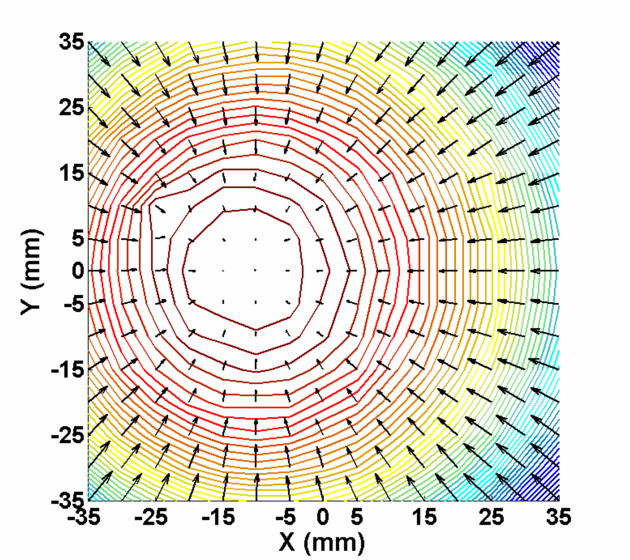

Figure 3-17: Measurement results for 2D distribution of B_z and field gradients at z=-0.06(m).

I_1=I_4=0.6(A), I_2= I_5=1(A), I_3= I_6=1.4(A), I_7=0

The two dimensional magnetic field distribution and its gradient is shown in Figure 3-17. As it is inferred from this figure, the maximum point of magnetic field was successfully shifted up to 10(mm) in the x direction.

The levitation system showed a satisfactory performance in the y direction as well. A shift along the negative direction of the y-axis was generated through decreasing the current in coils 1,2,3 and increasing the current in coils 4,5 and 6.

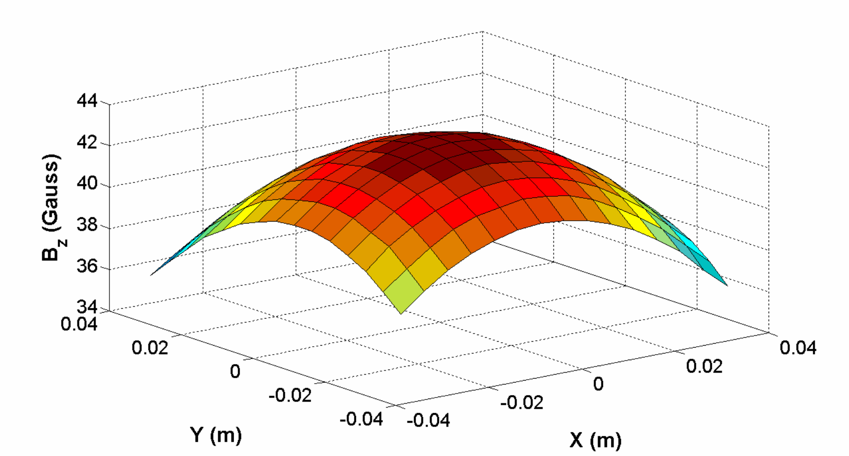

Figure 3-18: Measurement results for 3D distribution of B_z at z=-0.080(m).

I_1=I_3=0.9(A), I_2=0.75(A), I_4= I_6=2.1(A), I_5=2.25(A), I_7=0

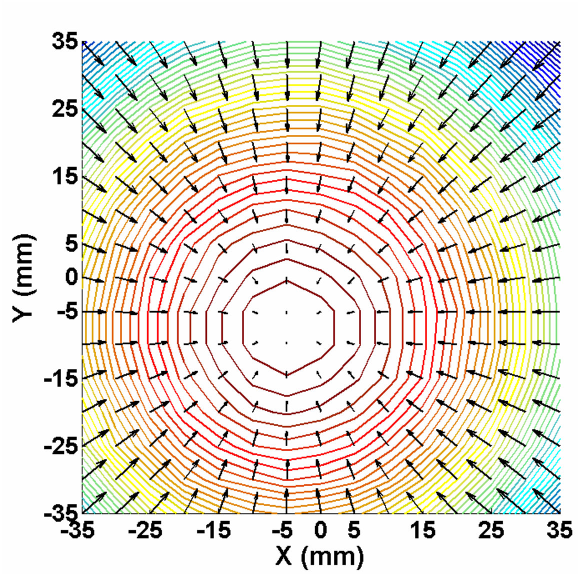

Figure 3-19: Measurement results for 2D distribution of B_z and field gradients at z=-0.080(m).

I_1=I_3=0.9(A), I_2=0.75(A), I_4= I_6=2.1(A), I_5=2.25(A), I_7=0

Figure 3-18 illustrates the 3D distribution of the B_z at vertical plane $z = -0.080(m)$. The two dimensional magnetic field distribution and magnetic gradient for this case is shown in Figure 3-19. As is seen in this figure, the maximum point of the magnetic field is shifted up to 10(mm) in the y direction.

It is important to note that the distance from the pole piece has a considerable effect on the ability to shift the maximum point of magnetic field. As mentioned earlier in this chapter, the working envelope of the levitation system is limited to a certain range below the pole piece. An experiment was performed to emphasize the effect of distance on the shift in the maximum point of magnetic field. An electrical current combination exactly the same as one used for Figure 3-18 was used in this experiment. The measurement plane was selected 5(mm) closer to the pole piece at $z = -0.075(m)$.

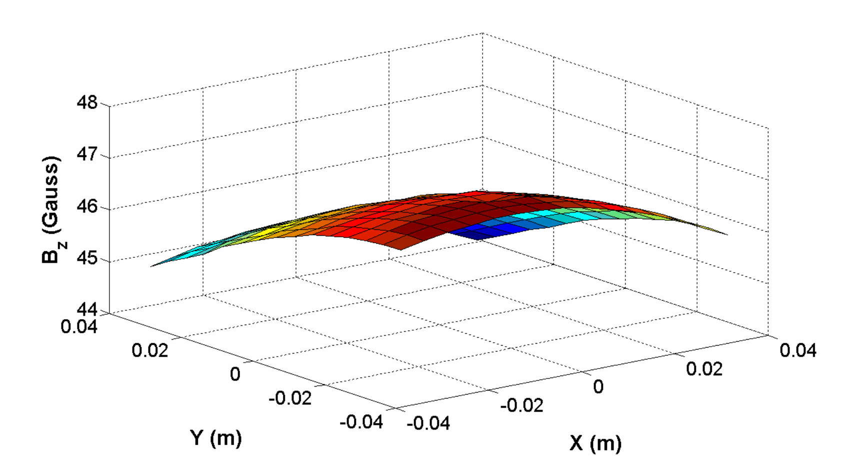

Figure 3-20: Measurement results for 3D distribution of B_z at z=-0.075(m).

$I_1=I_3=0.9(A)$, $I_2=0.75(A)$, $I_4= I_6=2.1(A)$, $I_5=2.25(A)$, $I_7=0$

Figure 3-20 shows the three dimensional distribution of B_z on the vertical measurement plane. As seen in Figure 3-21, decreasing the distance from the pole piece by 5(mm) resulted in a 20(mm) increase in the shift in the location of the maximum point of magnetic field.

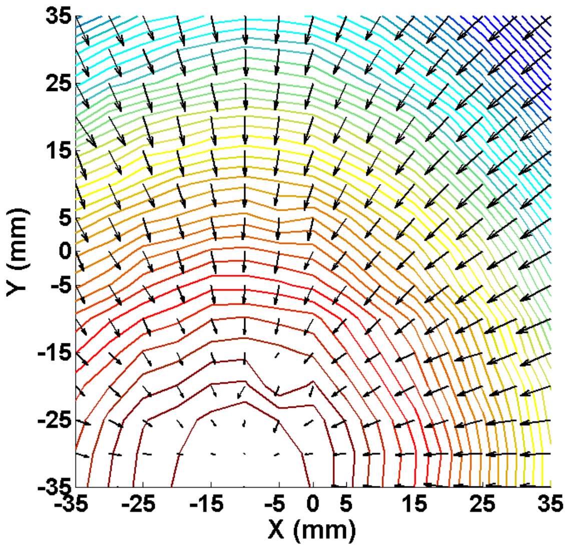

Figure 3-21: Measurement results for 2D distribution of B_z and field gradients at z=-0.075(m).

I_1=I_3=0.9(A), I_2=0.75(A), I_4= I_6=2.1(A), I_5=2.25(A), I_7=0

Distance from the pole piece also has a considerable effect on the vertical magnetic force experienced by the levitated object. Figure 3-22 shows the measured magnetic flux density B_z in the air gap along a vertical path below the center of the pole piece. In this figure Z(m) represents the distance between the measurement point and the bottom surface of the pole piece.

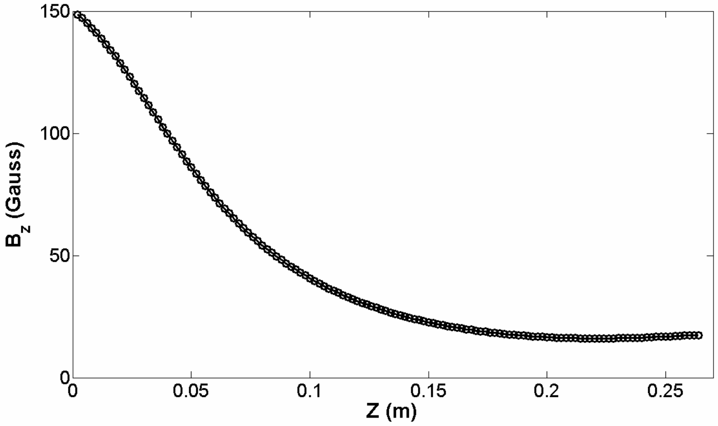

Figure 3-22: Measurement results for the effect of distance from the pole piece on B_z.

The measurements of this plot are obtained for the case that all the seven electromagnets of the device are fed with the electrical current of $1.5(A)$ each.

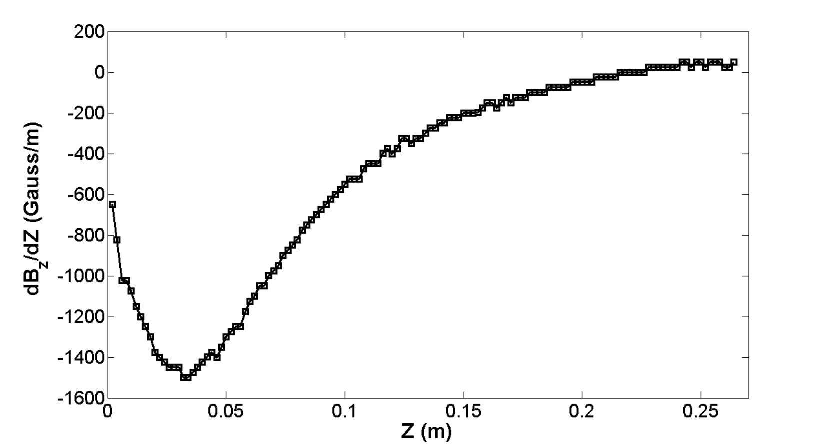

Figure 3-23: Gradient of B_z in the vertical direction.

As shown in the previous chapter, the magnitude of the vertical magnetic force experienced by the levitated object is proportional to the gradient of B_Z in the z direction. Figure 3-23 shows the gradient of the vertical magnetic field in the air gap.

As seen in this figure, the maximum magnetic field gradient was calculated approximately at z=0.04(m). Increasing the distance from the pole piece will drastically decrease the magnetic gradient level and hence the magnetic force value.

Considering the results magnetic shift measurement in Figure 3-19 and magnetic field gradient level in Figure 3-23 suggests that the bottom boundary of the working envelope is approximately located at the vertical plane $z = -0.1(m)$. The top boundary of the working envelope will also be close to $z = -0.04(m)$.

In the next section, the details of the final MDU design and experimental setup will be provided.

Chapter 4

System Setup

4.1. Introduction

In this chapter, the experimental setup and its components are introduced in detail. Figure 4-1 shows a schematic of the physical setup of the system. The laser position sensors measure the position of the levitated object and report the measured position to the controllers via a data acquisition board (DAQ). The signal from the laser sensors is in the form of an analogue voltage ranging from -10(v) to 10(v).

The DAQ then converts the voltage measurement back into a position measurement in order to generate the control signals. The output from the controller is a voltage from the analog output cards. Based on the input voltage, a specific current will be generated by the amplifier, and this current is output to the electromagnets. Up to 24 electromagnets can be connected to the amplifier. By varying the output voltage from the controller, the input current to the electromagnets will be controlled, which will change the magnetic field and cause the microrobot to move.

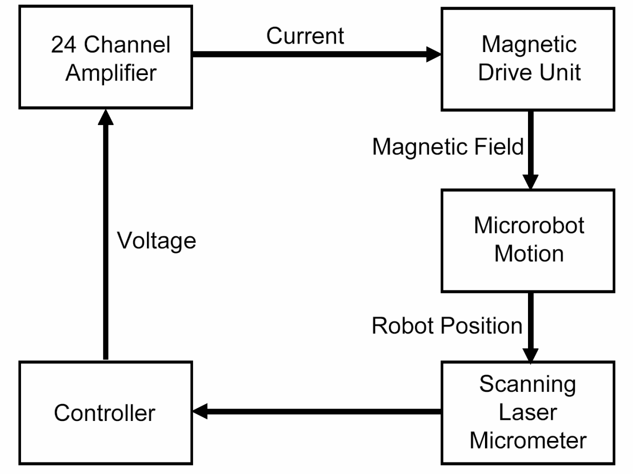

Figure 4-1: Schematic representation of the microrobot control loop.

The magnetic drive unit (MDU) is responsible for generating the appropriate magnetic field distribution and gradient required for levitation and manipulation of the object. The MDU comprises of three main parts; electromagnets, yoke and pole piece which will be discussed in the following.

4.2. Yoke and Pole Piece

The yoke and pole piece are shown in Figure 4-2 and Figure 4-3, respectively. Both yoke and pole piece are made from soft iron in order to improve the strength of the magnetic field produced by the electromagnets. The pole piece connects the poles of the electromagnets together and its responsibility is to generate a focal magnetic pole within the working envelope of the system.

Yoke is a C-shaped component designed to boost the concentration and gradient of the magnetic field within the air gap. The electromagnets can be mounted to a mounting bracket on both the upper and lower portions of the yoke. Different portions of the yoke can be reconfigured, allowing for different operating configurations. The upper portion of the yoke can be adjusted up and down relative to the lower portion of the yoke, allowing for experimentation with different air gap lengths.

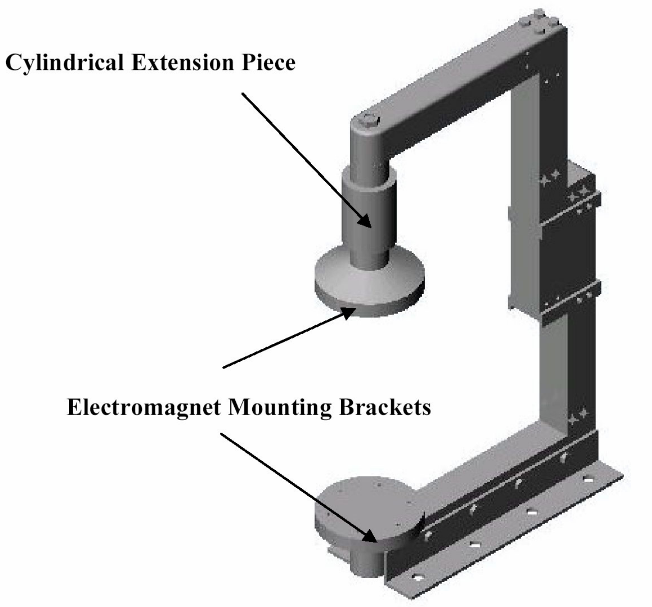

Figure 4-2: Yoke.

Permanent magnets can be inserted into the cylindrical extension piece in order to provide a bias field and theoretically reduce the power requirements needed for levitation. For the experiments in this thesis the standard cylindrical extension piece and mounting bracket are used. The air gap length is 282.6(mm).

The pole piece used for experimentation in this thesis is a disk shaped pole piece with diameter of 132(mm) and thickness of 6.35(mm). The disk pole piece was chosen as it was found to produce a strong magnetic field for vertical motion and a demonstrable shift in the equilibrium point during horizontal motion [91].

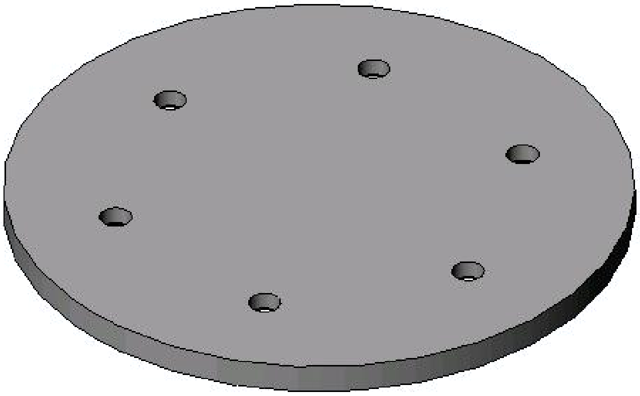

Figure 4-3: Pole piece.

4.3. Electromagnets

Up to 24 electromagnets can be installed on the magnetic drive unit. For the work discussed in this thesis seven electromagnets are installed on the upper portion of the yoke. The numbering scheme of the electromagnets is shown in Figure 4-4.

The electromagnets are custom made and provided with a male thread for attachment to the mounting bracket and a female thread for attaching the pole piece to the other side of the electromagnets. Each electromagnet has approximately 840 turns of #22 AWG wire [115]. The nominal electrical parameters of each electromagnet are shown in Table 4-1.

Table 4-1:Electrical parameters of the electromagnets [115].

Electromagnet	Resistance (Ω)	Inductance (mH)
1	4.27	29.68
2	4.23	28.84
3	4.25	29.08
4	4.25	28.77
5	4.29	27.65
6	4.25	29.64
7	4.31	28.83

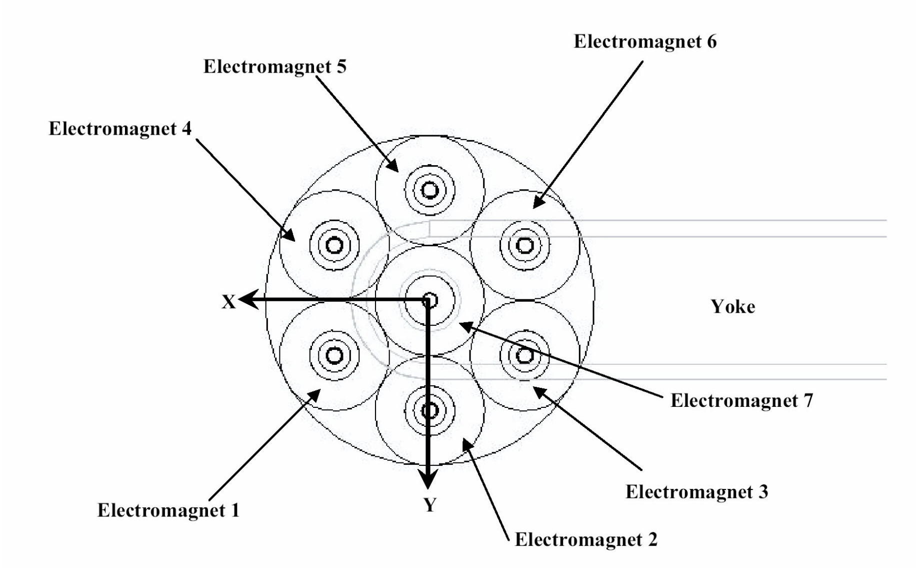

Figure 4-4: Electromagnets configuration.

4.4. Laser Sensor

Three Keyence LS-5000 scanning laser micrometers are used to measure the x, y, and z position of the levitating object. The sensors are mounted to an octagonal aluminium ring that surrounds the air gap workspace of the yoke, as shown in Figure 4-5. Important characteristics of the micrometer are summarized in Table 4-2. Figure 4-6 shows how the accuracy of the laser scanner varies depending on the location of the object being measured.

Table 4-2: Laser micrometer characteristics [116].

Measuring Range	0.2-40 mm
Scan Rate	1200 Hz
Analog Output Range	+/- 10 V
Analog Output Resolution	5 mV

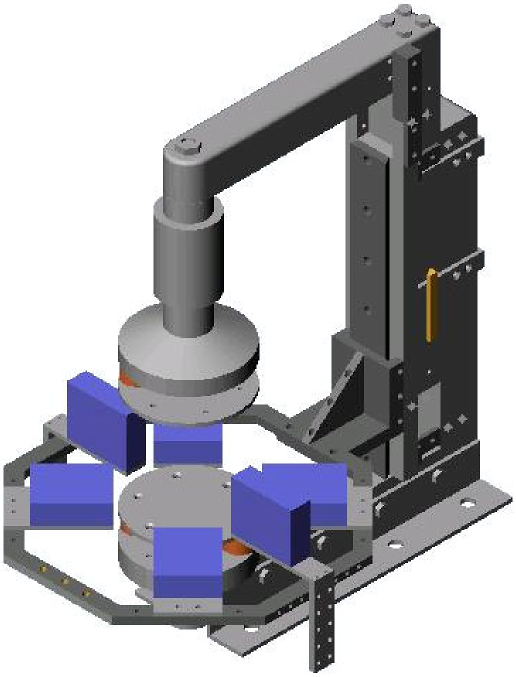

Figure 4-5: Assembled magnetic drive unit showing the layout of the laser micrometers.

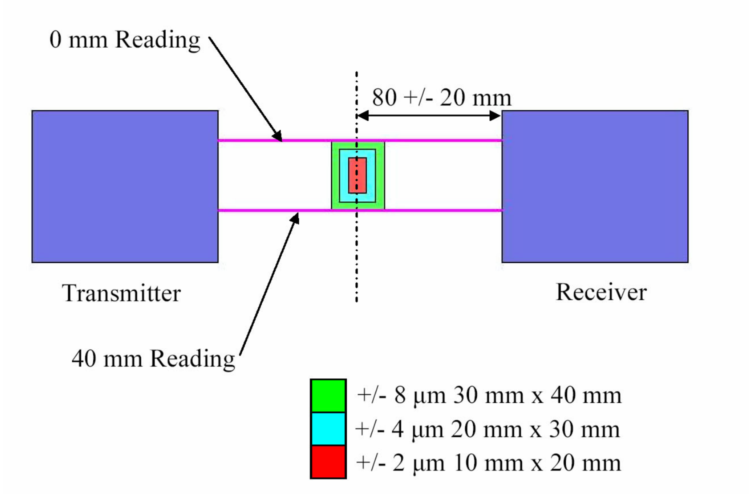

Figure 4-6: Accuracy mapping of the scanning micrometer [116].

Software is provided by Keyence that allows for calibration and configuration of the laser micrometers via an RS-232C serial connection through the COM1 or COM2 port on a computer.

Output from the laser sensors can be obtained from this serial port or through an analog output board. For this system the analog output boards are used since they permit faster data transmission than the serial connection. The output range of the analog boards is between -10 to +10 volts. Figure 4-7 illustrates the locations of the global and local frames and the location at which the output of the laser sensors will be -10(v). For simplicity in the discussion, the lasers are named as L1 and L2.

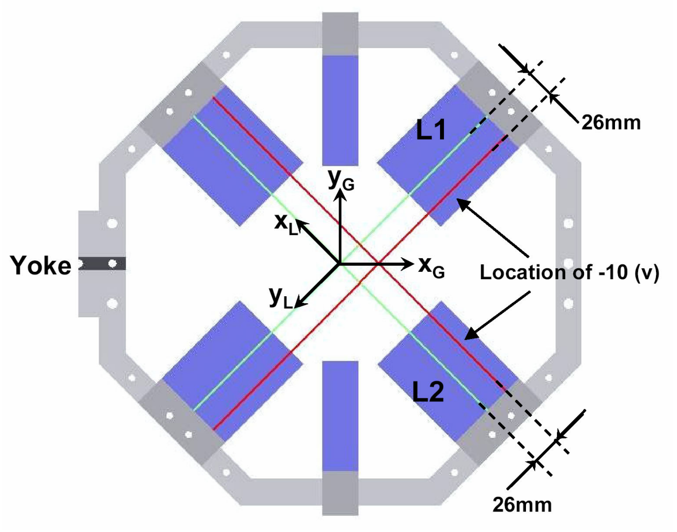

Figure 4-7: Demonstration of the local and global frames.

The first step towards transforming the laser output into an appropriate position measurement of the robot is to map the voltage outputs $\left(V_{L1},V_{L2}\right)$ of the lasers to the local cardinal pair $\left(x_L,y_L\right)$. As seen in Figure 4-7, at the location at which the lasers has the output of -10(v) we have $x_L=-26(\text{mm})$ and $y_L=-26(\text{mm})$. Therefore, the voltage mapping is obtained as:

$$x_L = 2V_{L1} - 6 \tag{4-1}$$

and

$$y_L = 2V_{L2} - 6 \tag{4-2}$$

where x_L and y_L are expressed in millimetres.

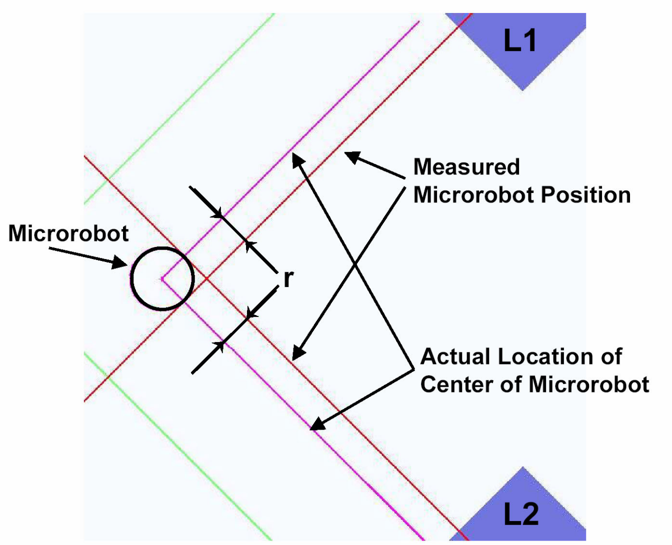

Figure 4-8: Measurement of the microrobot position.

The second step is to consider the microrobot's radius in the measurement. Figure 4-8 shows the measurement of the actual microrobot's position in the local frame. Since laser sensors read the position of the two tangent lines to the side of the microrobot, the perpendicular distances of this two lines from the center of the robot is equal to $r(\text{mm})$, which is the outer radius of the microrobot. Therefore, the actual location of the center of microrobot in the local frame, i.e. $\left(x_C,y_C\right)$, is obtained as:

$$x_C=x_L+r \tag{4-3}$$

and,

$$y_C = y_L + r \tag{4-4}$$

The third step is a rotational mapping between the local and global coordinates.

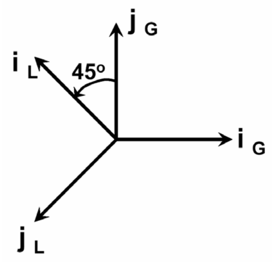

Figure 4-9: Rotation of the coordinate systems.

Figure 4-9 shows the rotation of the coordinate systems. The relation between the unit vectors of these two systems is obtained as:

$$\begin{aligned} \mathbf{i}_G &= -\sin\left(\frac{\pi}{4}\right)(\mathbf{i}_L + \mathbf{j}_L) \\ \mathbf{j}_G &= +\sin\left(\frac{\pi}{4}\right)(\mathbf{i}_L - \mathbf{j}_L) \end{aligned} \tag{4-5}$$

Therefore,

$$\begin{aligned} x_G &= -\sin\left(\frac{\pi}{4}\right)(x_C + y_C) \\ y_G &= +\sin\left(\frac{\pi}{4}\right)(x_C - y_C) \end{aligned} \tag{4-6}$$

For the horizontal measurement, since the laser stand is adjustable, the distance from the laser stand to the yoke, i.e. d(mm) must be considered in the calculations. Figure 4-10 shows the schematic of the vertical measurement frame. In this figure, h is defined as the vertical distance between the origin of the global frame and the location at which the laser output will be +10(v) and is obtained as:

$$h = -(d - 188) \tag{4-7}$$

The negative sign in Eq. (4-7) is due to the direction of positive z axis. Eq. (4-7) can be interpreted as the desired distance measurement for the case at which the laser output is equal to +10(v). Since the total measurement range of the laser is 40(mm) with an analogue output ranging from -10(v) to +10(v), the global measurement of z(mm) in terms of laser voltage V_{L3} is obtained as:

$$z = \left(20 - 2V_{L3}\right) - d + 188 \qquad (4\text{-}8)$$

where z is measured in millimetres.

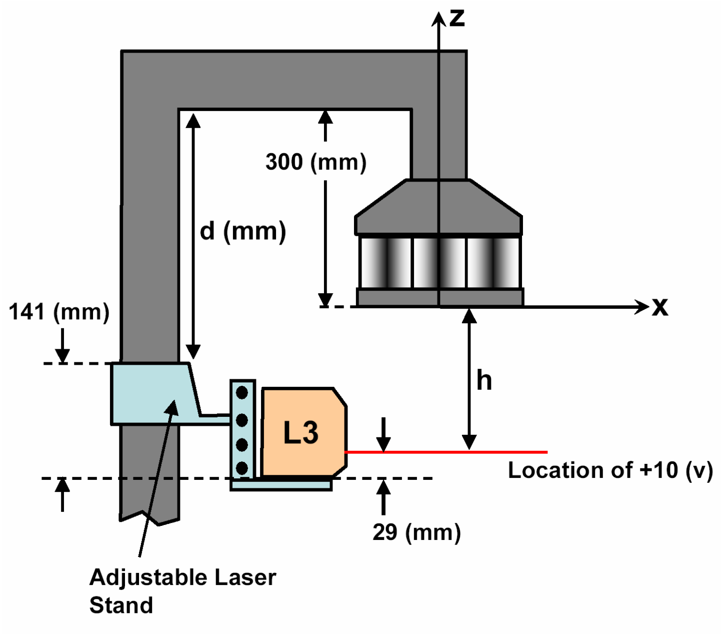

Figure 4-10: Vertical measurement frame.

4.5. Input DAQ

The input DAQ is a National Instruments NI-PXI-6251 series DAQ card. A summary of the important characteristics are found in Table 4-3.

Table 4-3: NI-PXI-6251 Characteristics [117].

Input Range	+/- 10 volts
Number of Bits	16
Resolution	0.305 mV
Random Noise Variance	280 μVrms
Gain Error	83e-6 V/V
Offset Error	20e-6 V/V
Gain Temperature Sensitivity	13e-6 V/(V°C)
Offset Temperature Sensitivity	21e-6 V/(V°C)
Reference Temperature Sensitivity	1e-6 V/(V°C)
Integral Non-Linearity Error	60e-6 V/V

4.6. LABVIEW Controller and Software

National Instruments' LabVIEW RT software is used to develop the controller architecture and user interface. There are several benefits to using LabVIEW RT.

LabVIEW provides an intuitive graphical-based method for the development of programs. There are several tools that allow for easy interface with the input and output boards. The interfacing is further simplified by the fact that the input and output boards and control processor are also manufactured by National Instruments. Many functions are also provided as standard features in the programming library, minimizing the amount of time required for writing and debugging code.

The additional benefit of LabVIEW RT is that it allows programs to be designed for and run in real time. This ensures that the program executes at a fixed time interval and that no control sampling cycles will be missed. A master-slave hardware setup is used to deploy the software. The time-critical code, written by the user, is executed on the slave under a real-time operating system, while two lower-priority programs, generated by LabVIEW, are used to pass data back and forth to the user interface via a TCP/IP connection.

The slave is a NI-PXI-8186 2.2 GHz processor board running the LabVIEW RT operating system. The master is an Intel Pentium 4 2.6 GHz personal computer running the Windows XP operating system.

Data is stored in an array while the program is running, the size of which depends on the number of variables being measured, the runtime of the experiment, and the sampling frequency.

The number of entries for each variable is fixed by the runtime and sampling rate at the start of the experiment, which means that data from the start of the experiment will be overwritten by newer data if the experiment runs longer than the specified runtime.

When the experiment ends the data is written to a comma separated value (CSV) file and saved on the hard disk of the slave. The CSV files can be transferred to the master via FTP, or the slave can be booted into Windows XP mode and the files can be transferred to a disk. CSV files can be opened by Microsoft Excel or MATLAB for inspection and plotting the data.

4.7. Output Cards

The three analog output cards are National Instruments NI-PXI-6733 series cards. Important characteristics are found in Table 3-4.

Table 4-4: Analogue output card characteristics [118].

Input Range	+/- 10 volts
Number of Bits	16
Resolution	0.305 mV

4.8. Power Supplies and Amplifier

Considering a power supply for the magnetic drive unit, both AC and DC power supplies can be used for magnetic levitation. However, due to the possible use of permanent magnets in the yoke (Section 4.2), a DC power supply is more appropriate to energize the electromagnets [133]. Also, due to the weight cancellation characteristic of the levitation system, presence of a positive current in electromagnets is always necessary to cancel the weight of the levitated object. Moreover, in magnetic levitation systems, DC current shows better stability than AC current. Therefore, a DC power supply was selected for energizing the levitation system.

Given all these considerations, two Sorensen DCS40-30E DC power supplies are used to provide power to the electromagnets. Each power supply is configured to provide power to up to twelve electromagnets. Only one of the power supplies is currently in use since only seven electromagnets are installed on the magnetic drive unit. The output voltage of the power supply is kept constant at 40 (v), with the output current drawn by supply is dependent on the voltage input by the controller. The maximum output current from the power supply is 30 (A). [119].

The amplifier was custom built by the Faculty of Science at the University of Waterloo. The amplifier has three input connectors to connect the cables from the controller output cards and 24 output channels for the electromagnets. The amplifier is designed to output a current based on the input voltage from the controller. The approximate gain equation mapping the input voltage v to the output current i for the amplifier is:

$$i = 0.355v \tag{4-9}$$

The typical input-output response of the amplifier is shown in Figure 4-11. Given the maximum input of 10(v), the maximum output current is 3.55(A). The maximum potential current that can be drawn by the current setup of the magnetic drive unit is approximately 20(A), which is within the output limits of the amplifiers.

The amplifier is a semi-active linear amplifier meaning that it can control the current increase in the coils but does not have any control on the power decrease in the coils. The current decrease in the coils takes place due to the dissipation of electrical energy through a diode circuit.

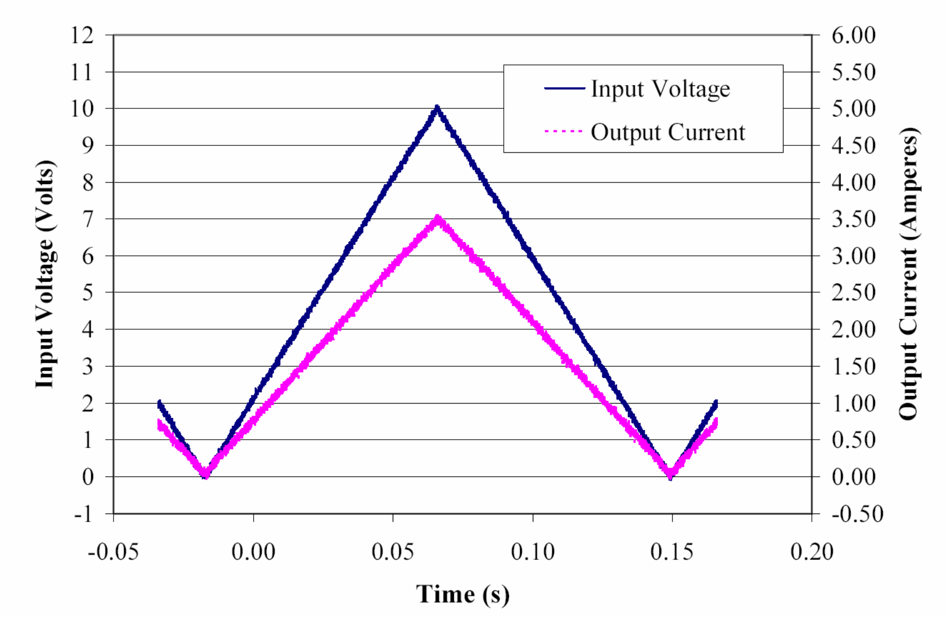

Figure 4-11: Input/Output response of channel 1 of the amplifier.

As stated before, the input to the amplifier is an analogue voltage ranging from 0 to 10 (v) which results in an analogue current in the coils ranging from 0 to 3.55(A).

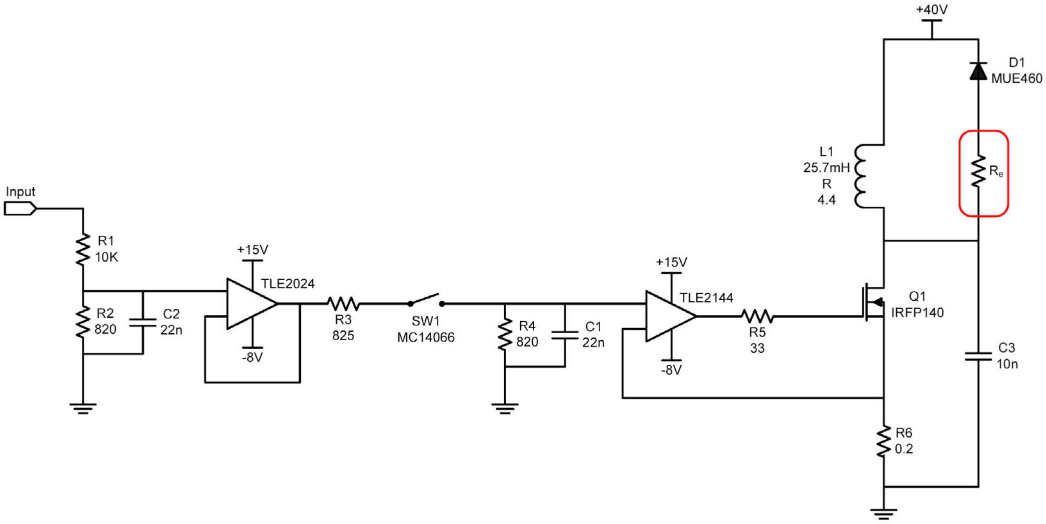

Figure 4-12: Schematic diagram of the amplifier circuit.

Since the amplifier is a semi-active type, there is no active control on the current at the time at which a current reduction is required. In order to improve the performance of the amplifier in current reduction cycles, an extra resistor R_e was added to the amplifier system as shown in Figure 4-12.

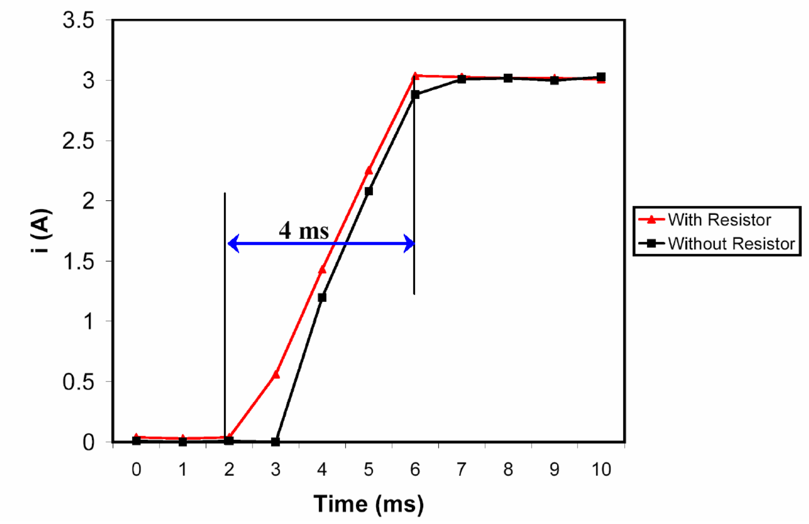

Figure 4-13: Experimental response of the amplifier in current raise from 0 to 3(A).

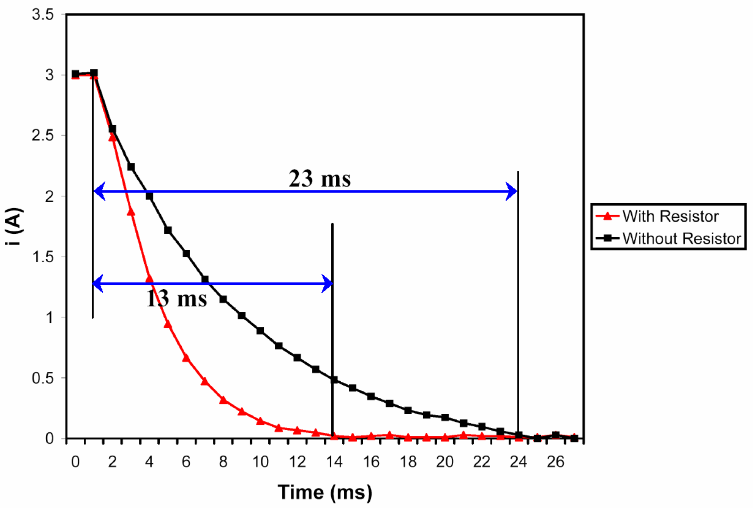

Figure 4-14: Experimental response of the amplifier in current fall from 3(A) to 0.

The effect of the extra resistor is shown in Figure 4-13 and Figure 4-14 in current rise and current fall cycles respectively. As illustrated in these figures, although the extra resistor significantly improved the performance of the system in current fall cycles, there is still a considerable difference between the amplifier's rise and fall cycles. This difference will slightly change the response of the levitating object in following positive and negative step commands which will be discussed in the next chapters. The performance characteristics of the individual channels of the amplifier is presented in Appendix C.

4.9. Levitated Object Properties

Two different objects were used in the experiments. Most of the experiments are performed using a cylindrical permanent magnet placed inside a light and thin plastic shield as shown in Figure 4-15. All the sizes are in millimetres.

The 10(mm) x 10(mm) neodymium magnet provides the dipole moment that interacts with the external field to produce the operating force. The plastic body is used to protect the neodymium magnet from damage due to falling out of the field or collision with the pole piece. The wider cylindrical portion at the top of the microrobot allows for a larger range of travel in the x and y directions. The remnant flux density of the magnet is 1.3(T), giving the microrobot a dipole moment of 0.813(Am^2). The total mass of the microrobot is 6.59 grams.

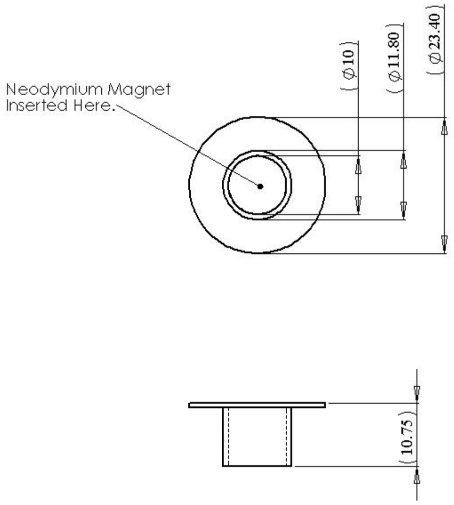

Figure 4-15: Permanent magnet prototype.

The second levitated object is a microrobot comprising two main parts; magnetic head and body. The magnetic head is made of nylon and holds three 10(mm) x 10(mm) neodymium magnets all with the same dipole direction. The magnetic head dimensions and geometry are shown in Figure 4-16. The permanent magnets are plugged into the magnet holes shown in the figure.

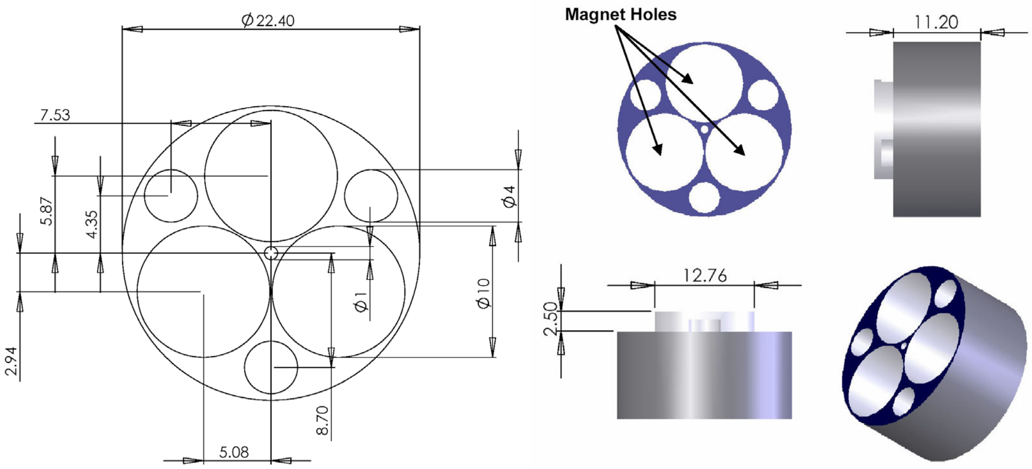

Figure 4-16: Schematic of the microrobot's magnetic head (all dimensions are in millimetres).

The body of the microrobot is a cylindrical tube made from nylon and holds the batteries, an electrical circuit and a micro gripper. There are three batteries installed in the microrobot. A 1.5(v) #357/303 bottom battery energises the micro gripper while two serial 1.5(v) # 384/392 bottom batteries are used to provide the power for the electrical circuits in the microrobot.

The electrical circuit is a remote infrared (IR) switch used to operate the micro gripper. When an external IR signal is detected by the circuit, it activates a connection between the battery and the micro gripper and hence turns it on. If there is no signal detected by the circuit, the battery is disconnected from the micro gripper and the micro gripper fingers are closed. Figure 4-17 shows a schematic of the IR circuit.

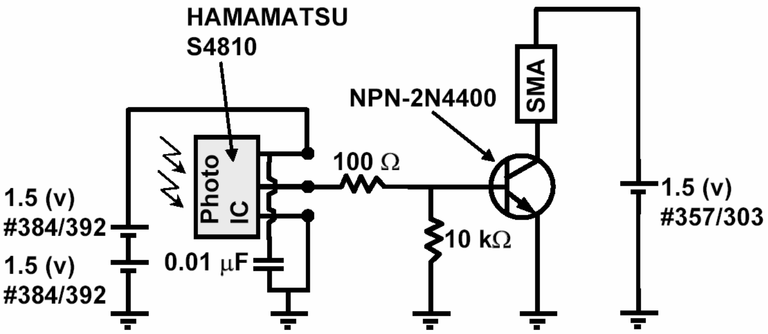

Figure 4-17: Schematic of the IR circuit.

The micro gripper is actuated using a 150μm shape memory alloy (SMA) spring. The fingers are made from 100μm music wire and are shaped in such a way that the gripper is passively closed as shown in Figure 4-18.

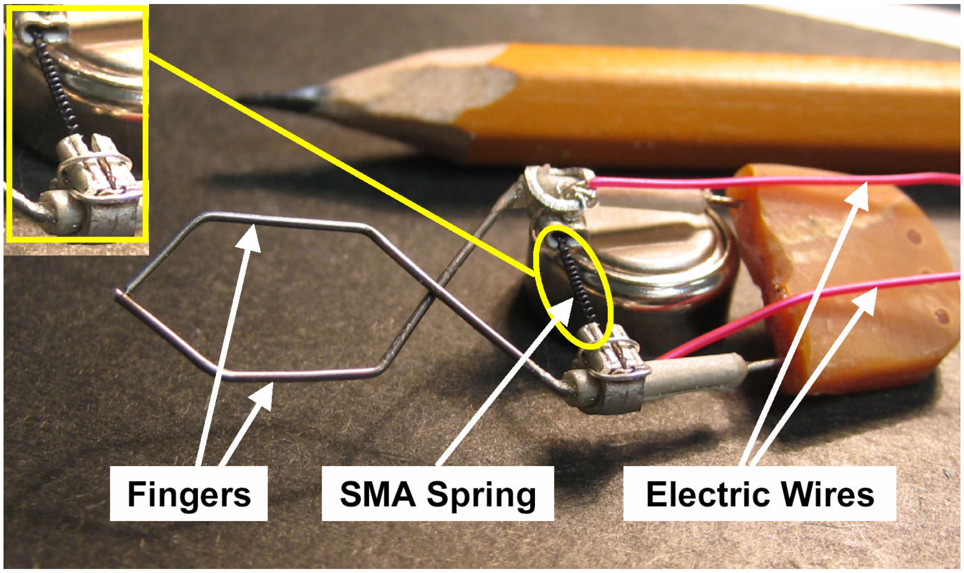

Figure 4-18: The micro gripper.

This increases the battery life as the gripper has to be activated only at the times of grasping and releasing. Figure 4-19 illustrates the fabricated microrobot.

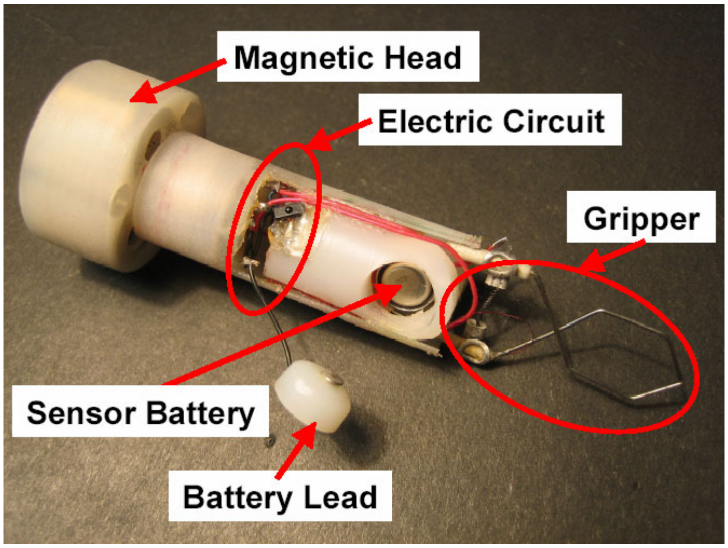

Figure 4-19: The fabricated microrobot.

The microrobot weights approximately 28 grams including its batteries. The gripper battery is installed on the top part of the microrobot body below the magnetic head as shown in Figure 4-20.

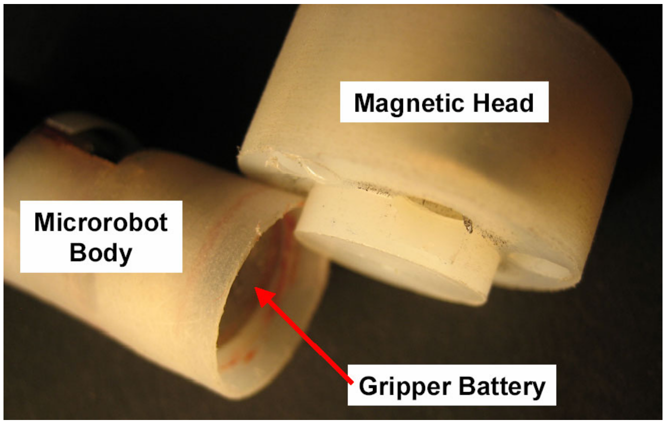

Figure 4-20: Installation of the gripper battery.

4.10. Theoretical Input Accuracy

The precision of the laser scanner is affected by the number of averaging measurements used to produce an output. The scanning rate is 1200(Hz), meaning one scan occurs every 0.833(ms).

While averaging more measurements will produce a more precise result, the trade-off is that it will take time to perform these measurements. For example, the Keyence system is capable of performing 6144 averaging measurements. This measurement will be extremely precise (on the order of 0.01 micrometers), but it will take 5.118 seconds to perform a single measurement. For a magnetic levitation system it is desired to have the sampling rate be as high as possible in order to maintain stability due to the fact that the levitated object is capable of moving at relatively high velocities and accelerations.

There is therefore a trade-off between increasing the precision of the system and increasing the the sampling rate. It has been observed that higher measurement accuracies yield lower sampling rates and hence, adversely affect the stability of the microrobot.

The system accuracy and precision is also significantly affected by object position and object alignment in the field. The object must be perfectly level in the measuring field in order to obtain the best possible measurement. Accuracy will also suffer if the object is located outside of the recommended measuring range as specified in Figure 4-6. As shown in this figure, the accuracy of the micrometer varies from 2 to 8(μm), depending on where the object is located in the micrometer's measuring field.

The resolution of the analog output board will also play a factor in determining the output of the system. Based on the data in Table 4-2, the equivalent position resolution of the analog output can be found by equating the voltage range to voltage resolution ratio (in volts) to the positional range resolution ratio (in mm). For the given system the equation is:

$$\frac{20}{0.005} = \frac{40}{x} \Rightarrow x = 0.010 \tag{4-10}$$

That is, the equivalent position resolution from the analog output is 0.01 mm.

4.11. DAQ Theoretical Accuracy

It is expected that the accuracy of the DAQ voltage will vary between 1850(μV) at a zero voltage reading and 2880(μV) at full scale. The basis for this calculation is discussed in [117] and presented in Appendix D.

Note that there is some uncertainty as to the values that should be used to account for changes in the ambient temperature. Given that the equipment is relatively new it was believed that there should be negligible temperature effects, although this may need to be investigated further in order to see if improvements can be made to the system. As with the laser micrometer, it is possible to obtain more accurate data by averaging the data input by the DAQ as opposed to averaging at the Keyence sensor.

4.12. Total Theoretical Input Accuracy

Based on the above information it is possible to get a rough idea of what the accuracy of an analog input measurement will be. For a given nominal position measurement, the laser system accuracy and analog resolution can be used to determine the range of the output voltage. This can then be converted to the actual input voltage seen by the DAQ, based on the resolution of the DAQ.

At this point the DAQ errors can be factored into the voltage and the measurement can be converted back into a position measurement and compared to what the nominal voltage should be. Calculation details are discussed in Appendix E and the net result is summarized in Table 4-5.

It is observed that the worst-case error is on the order of 15 micrometers, although error on the order of 6.6 micrometers may be more common.

Table 4-5: Sample error calculation series for a nominal measurement of 30.001 mm.

Measurement (mm)	Error (mm)
30.01586	-0.01486
30.00434	-0.00334
30.00610	-0.00510
29.99438	0.00662

In order to test the accuracy of the vertical position sensor, a one inch gauge block was placed on a platform inside the z position sensor's measuring field. Measurements are then made with and without the gauge block.

In each case the mean value of the measurements are found and the difference is calculated. It is expected that the net difference should be equal to 25.4(mm). The results are shown in Table 4-6. While the overall average measurement of the block height is fairly accurate, the standard deviation of the measurement indicates that there is a high degree of variation between individual measurements. This is not unexpected given the behaviour of the laser sensor.

Table 4-6: Measurements of a one inch gauge block using the laser micrometer.

Calculated Average Height (mm)	Standard Deviation (mm)	Error (µm)
25.3975	0.014813	2.5
25.40501	0.018662	5
25.40577	0.017287	5.8
25.40298	0.017874	3

The gauge block measurements indicated that the error should be significantly greater than what the theory indicates. A more accurate picture of the true sensor accuracy can be obtained by using the measurement hold feature on the Keyence sensor. This will eliminate any errors due to poor measurement repeatability.

The sensor will send a constant voltage to the DAQ, and the resulting variance in the measurement should be simply due to the accuracy of the DAQ. The resultant measured means and standard deviations for an arbitrary object in the measurement field are shown in Table 4-7. This standard deviation of the hold operation is more in line with what might be expected based on the theoretical error calculation shown in Table 4-5.

Based on this data it is apparent that a great deal of the measurement variance in the system is introduced directly by the laser sensor.

Table 4-7: Comparison of the mean and standard deviation produced by an object in the field.

	Mean (mm)	Standard Deviation (µm)
No Hold on Output	10.2883	12.987
Hold on Output	10.27829	6.384

In the first case, the output from the sensor is allowed to float, while in the latter case the output voltage is held constant. It is known that there is some sort of electric motor inside the laser sensor transmitter. The rotation of this motor may be causing small displacements of the sensor due to the fact that its mounting bracket is cantilevered.

These displacements are within the accepted mounting tolerance of the sensors, but do contribute to the increased variance of the system.

4.13. Output Accuracy

Unlike the input DAQ there is not as much information available regarding the accuracy of the output cards. Because they have the same range and resolution as the input cards, it is assumed that accuracy of the output voltage will be similar. That is, the output voltage will vary from 1850(μV) at zero output to 2880(μV) at full scale.

Chapter 5

Dynamic Modeling of Magnetic Force

5.1. Introduction

This chapter presents a dynamic model for the magnetic force experienced by the levitated object. A substantial part of the research on the magnetic levitation systems has been focused on the development of precise magnetic force models which led to the proposition of several force models over the past years. The proposed models are generally assuming a squared relationship between the electric current in the coil and the magnetic force.

Peterson et al in [120] proposed a static magnetic force model assuming that the force is proportional to the magnetic flux squared. Due to the linear relationship between the magnetic flux and electrical current in the coil, this assumption leads to a second order relationship between the magnetic force and the current.

The authors in [121]-[125] assumed that the magnetic force is directly proportional to the squared current in the coil and inversely proportional to the squared gap between the electromagnet and the object.

Lin et al [126] assumed that the magnetic force is linearly proportional to the current and inversely proportional to the forth power of distance.

In all of the above mentioned models, the proposed magnetic force model is static. This means that the delayed behavior of the magnetic force with respect to the control variable, i.e. the electric current, is not taken into account. In this chapter a modular approach is proposed to obtain the dynamic model of the magnetic force which includes a delay function for the time lag between the force and current.

Due to the intrinsic inductance effect in the magnetic materials, there is always a time lag between the current fed to the system and the magnetic field generated by the coils. This time lag introduces a delay in the generation of magnetic force and should be taken into account. A through dynamic model of the ML system should include the models of all the components of ML device.

In the next section, frequency response identification methods are applied on all the components of the system and the total magnetic force model is proposed.

5.2. Frequency Response Identification of the ML System

In this section, the frequency response identification technique is applied on all the composing modules of the ML device. The first component analyzed is the electric current power amplifier. Figure 5-1 shows the schematic layout of the amplifier.

The amplifier receives the input command from the controller and adjusts the currents in the electromagnets accordingly. The command from the controller is in the form of an analog voltage ranging from 0 to 10 volts.

A HP signal analyzer was used to get the sweep sine frequency response of the power amplifier and the coil. Figure 5-2 shows the frequency response of the amplifier when the output is set to be the current in the coil and the input is the controller command fed to the amplifier.

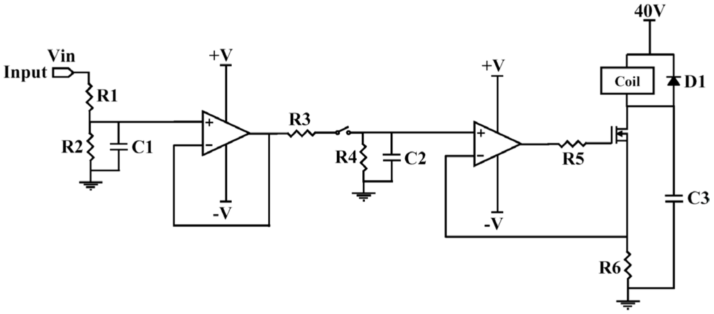

Figure 5-1: Schematic layout of the power amplifier circuit.

As it is seen in this figure, analyzing the frequency response data shows that the power amplifier can be assumed as a linear gain for frequencies up to 1.7(KHz) with magnitude descent of less than 0.7dB and phase lag of less than 8 degrees.

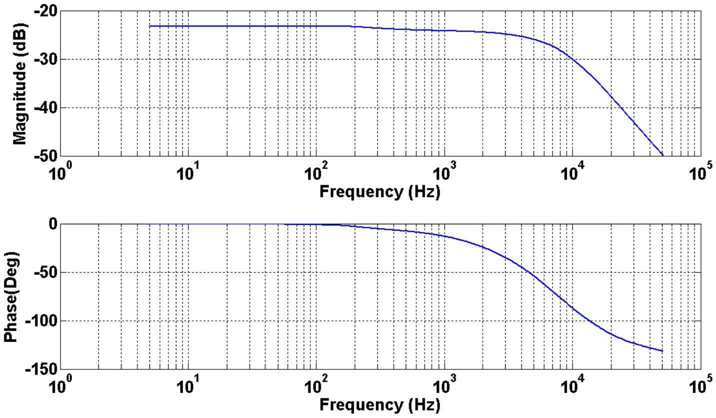

Figure 5-2: Frequency response of the amplifier circuit.

Since the sampling frequency of the control loop is 1.6(KHz), the maximum communication speed between the controller and the power amplifier is bounded to 1.6(KHz). This makes the assumption of a linear gain as the model of the amplifier reasonable. Thus, the amplifier's transfer function is obtained as

$$G_{amp}\left(s\right)=\frac{I\left(s\right)}{V\left(s\right)}=k_{amp} \tag{5-1}$$

where $I\left(s\right)$ is the current in the coil, $V\left(s\right)$ is the voltage fed to the amplifier and k_{amp} is a constant number called the amplifier gain.

Although the amplifier bears very little delay in adjusting the current in the coils, there is still a delay between the current fed to the coils and the field generated by the coils that has to be modeled. Since the levitation takes place in the vertical direction, the magnetic field identification was performed on the magnetic field in the z-direction i.e. B_z.

The field at each point within the air gap is a function of current in the coil and the distance from the coil. Therefore, the magnetic field model should include both distance and current.

In order to obtain the relationship between the distance and the field, a set of frequency response identifications were performed at different heights below the pole piece. In each experiment, a gauss meter probe was fixed at a certain height below the pole piece and the current-magnetic field relationship in frequency domain was measured using the HP signal analyzer.

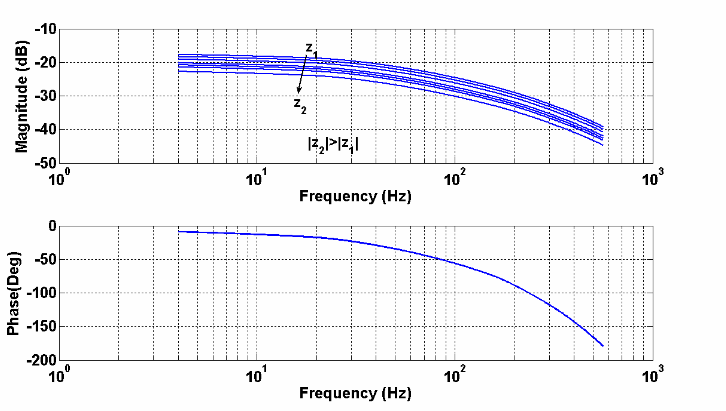

Figure 5-3: Frequency response of the magnetic field.

Figure 5-3 shows the frequency response of the magnetic field versus the current in the coils at different heights below the pole piece. As is seen in this figure, the height does not have any considerable effect on the phase of the field. The effect of height on the magnitude of the field shows itself as a varying gain k.

The parallel scheme of magnitude plots in Figure 5-3 suggests that the height can be decoupled from the magnetic field model. In other words, by using the separation of variable method, the field-current and field-distance relationships can be modeled separately to form the total field model components.

Figure 5-4 shows the magnetic field frequency response plots at 0.1(m) below the pole piece. Using the classic method of Bode plot identification [127], the corner frequency of magnitude plot was found at $f_c = 43\text{Hz}$. Since all the magnitude plots at different heights are parallel, this corner frequency will be the same for all the plots.

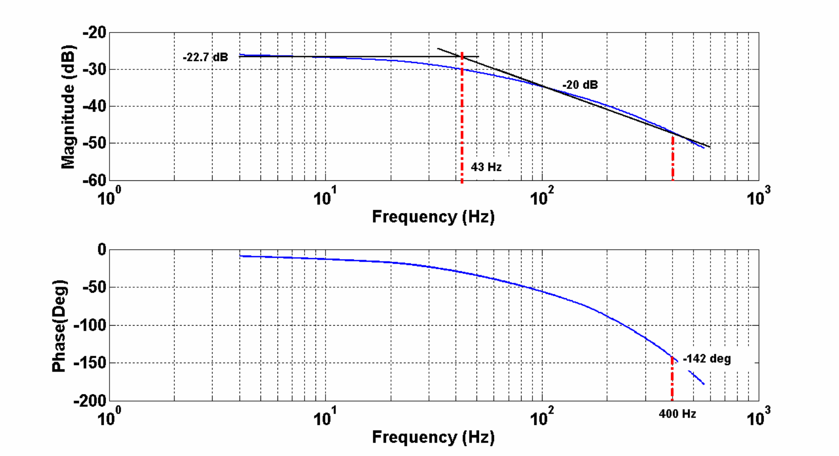

Figure 5-4: Frequency response of the magnetic field at 0.1m below the pole piece.

The magnitude plot shown in Figure 5-4 clearly shows a first order transfer function between the field and the current as:

$$G_B(s) = \frac{\mathrm{B_z}(s)}{\mathrm{I}(s)} = \frac{k}{1+\tau s} \tag{5-2}$$

where k and τ are two constant coefficients. According to the values shown in magnitude plot, k and τ are given as:

$$k = 10^{-22.742/20} = 0.073(\mathrm{T/A}) \tag{5-3}$$

$$\tau = \frac{1}{2\pi f_c} = \frac{1}{2\pi(43)} = 0.0037(\mathrm{s}) \tag{5-4}$$

where f_c is the corner frequency in Hz. Using Eqs.s (5-2) to (5-4) led to a very good match in the magnitude plots for the experimental data and the suggested transfer function. However, the phase plot does not show a good match (Figure 5-6).

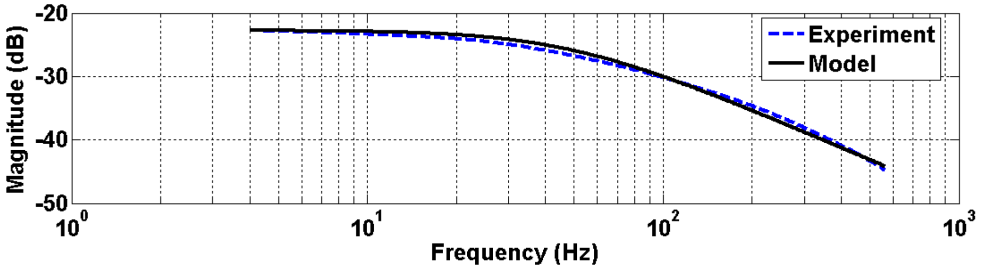

Figure 5-5: Comparison between the magnitude plots.

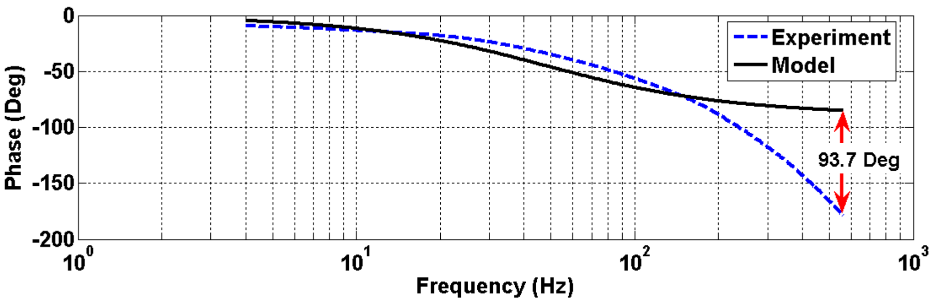

Figure 5-6: Comparison between the phase plots.

The phase plot shows a good match for frequencies less than 100Hz which is within the working frequency range of the ML device. Therefore, knowing that the operating frequency of the ML system won't pass 100Hz, the transfer function $G(s)$ in Eq. (5-2) is suitable for modeling the field-current relationship. Thus, the relationship between the magnetic field B_z and voltage V is obtained from Eqs.(5-1) and (5-2) as:

$$G_{field}(s)=\frac{B_z(s)}{V(s)}=\frac{k_{amp}k}{1+\tau s} \tag{5-5}$$

where G_{field} is the transfer function between the field and the voltage from the controller.

The next step towards getting the total magnetic field model is to recognize a relationship between the height and the gain k. Since all the magnitude plots in Figure 5-3 are parallel, they all have the same corner frequency and their only difference is in their gain k. Therefore, the relationship between the voltage, height and the field is in the form of:

$$G_{field}(s)=\frac{B_z(s)}{V(s)}=\frac{k_{amp}k(z)}{1+\tau s} \tag{5-6}$$

Figure 5-7 shows the relationship between the gain k and the distance. A second order polynomial was fit on the gain plot resulting in the general form of magnetic field model as:

$$G_{field}(s)=\frac{B_z(s)}{V(s)}=\frac{k_{amp}\left(c_1z^2+c_2z+c_3\right)}{1+\tau s} \tag{5-7}$$

where c_1, c_2 and c_3 are the polynomial coefficients and are found experimentally.

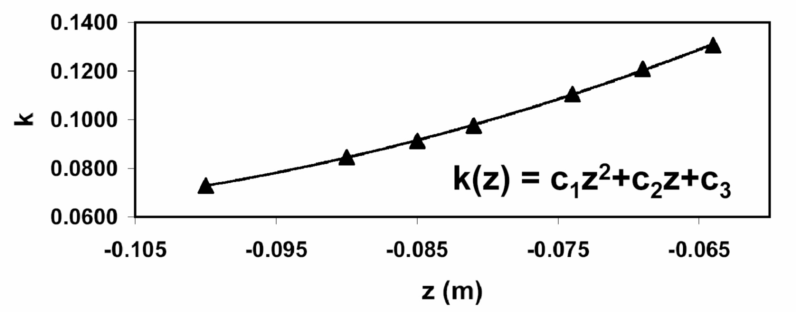

Figure 5-7: Relationship between gain k and distance.

Having the magnetic field model, the magnetic force can be found easily. As stated earlier, the magnetic force experienced by the levitated object is linearly related to the gradient of the magnetic field. Therefore, the vertical magnetic force model can be obtained as:

$$F_z(s) = |\mathbf{P}|\left(\frac{2c_1 z + c_2}{1+\tau s} k_{amp}\right) V(s) \tag{5-8}$$

where $|\mathbf{P}|$ is a constant number equal to the magnetic dipole moment of the levitated permanent magnet in the z direction. The magnetic force model can be rewritten as:

$$F_z(s) = (\alpha z + \beta)\left(\frac{V(s)}{s + 1/\tau}\right) \tag{5-9}$$

Coefficients α and β are defined as $\alpha = |\mathbf{P}|\left(2c_1 k_{amp}\right)/\tau$ and $\beta = |\mathbf{P}|\left(c_2 k_{amp}\right)/\tau$. By assuming that the input $V(s)$ is in the form of a step function with magnitude of V, the magnetic force in the time domain is calculated as:

$$F_z(t) = (\alpha z + \beta)\left(1 - e^{\frac{-1}{\tau}t}\right)V \qquad t \geq 0 \tag{5-10}$$

where V is the magnitude of controller command in terms of an analog voltage. The assumption of the input in the form of a step function is based on the fact that in discrete implementation of the physical system, the input value between two consecutive samplings is kept constant and is in the form of a step function.

The total equation of the motion for the levitated object is obtained through the application of Newton's second law. Figure 5-8 illustrates the free body diagram of a levitated permanent magnet.

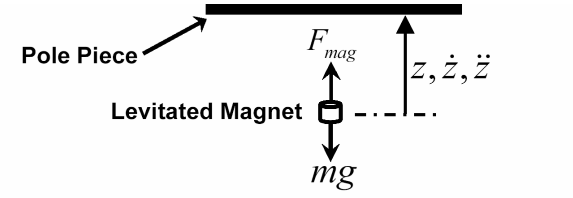

Figure 5-8: Free body diagram of the levitated permanent magnet.

The position of the levitated object is related to the magnetic force as:

$$F_{mag} - mg = m\ddot{z} \tag{5-11}$$

where g is the acceleration of earth gravity, m is the mass of the levitated object and z is the vertical distance of the levitated object from the pole piece. Substituting Eq. (5-10) into Eq.(5-11), the dynamic equation of motion is obtained as:

$$(\alpha z + \beta)\left(1 - e^{\frac{-1}{\tau}t}\right)V - mg = m\ddot{z} \tag{5-12}$$

By proper adjustment of voltage V in Eq. (5-12), the position and speed of the levitated object in the z direction can be controlled. This will be discussed in the next chapter.

In practice, the values of α and β obtained experimentally for a particular working range. In the next section the experimental procedure for estimating the values of α and β is presented.

5.3. Experimental Evaluation of Coefficients α and β

Accurate evaluation of coefficients α and β have an important effect on the performance of the control system. Due to the difficulties in calculating the dipole moment of the permanent magnets in the levitated object and the polynomial coefficients c_1 and c_2, an experimental procedure was utilized resulting in the calculation of α and β.

Assuming that the magnetic levitated object is in a steady-state situation, Eq. (5-12) yields:

$$(\alpha z + \beta)V = mg \tag{5-13}$$

Now, let define the operating point of the system as the pair (z_0, V_0) such that:

$$(\alpha z_0 + \beta)V_0 = mg \tag{5-14}$$

Although the system is inherently unstable and needs a closed loop control rule to be stabilized, the approximate operating point pair can be found through an open loop approach using the following procedure:

1. Place the object to be levitated on a stationary platform in the air gap and record the z.
2. Increase the voltage fed to the power amplifier by 0.1(v)
3. If the object is still sitting on the platform, repeat step 2.
4. If the object is levitated or is stuck to the top pole piece, record the voltage and go to step 5.
5. End.

Performing the above procedure at z_1 will result in the calculation of pair $\left(z_1, V_1\right)$ and performing it for z_2 will result in the calculation of $\left(z_2, V_2\right)$. In fact, these two pairs are approximate estimates of two operating points of the system.

The object will eventually stick to the top pole piece as soon as it experiences a force slightly bigger than its own weight. Since the voltage increment in each step is very small, estimation of the operating voltage is fairly accurate. Once the two operating pairs are found, the coefficients α and β for a working range within z_1 and z_2 are found through the formation of a system of simultaneous equations as:

$$\begin{aligned} \left(z_1 V_1\right)\alpha + \left(V_1\right)\beta &= mg \\ \left(z_2 V_2\right)\alpha + \left(V_2\right)\beta &= mg \end{aligned} \tag{5-15}$$

which results in the calculation of coefficients α and β as:

$$\alpha = \frac{mg\left(V_2 - V_1\right)}{V_1 V_2\left(z_1 - z_2\right)} \tag{5-16}$$

$$\beta = \frac{mg\left(z_1 V_1 - z_2 V_2\right)}{V_1 V_2\left(z_1 - z_2\right)} \tag{5-17}$$

More accurate results can be obtained using the closed loop control data. In the presence of a stabilizing closed loop controller, more accurate operating pairs can be calculated. This will increase the accuracy of α and β. In the next chapter, the controller design for the ML system will be presented.

Chapter 6

Vertical Position Control

6.1. Introduction

In this section, vertical position control of the object is discussed. In general, position control of the levitated object, is a challenging task. The levitation system is inherently an unstable system requiring closed-loop control rules to be stabilized [92]. Figure 6-1 provides the schematic of the closed loop position control system.

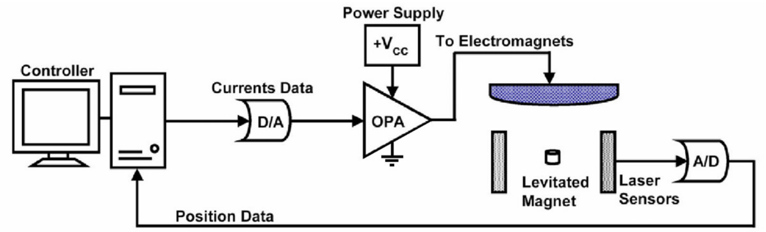

Figure 6-1: Schematic diagram of the closed loop control loop.

As mentioned in the experimental setup chapter, the controller receives the position of the levitated object from the laser position sensors. Based on the laser readings and the desired position of the levitated object, the controller calculates an appropriate control signal and sends it to the operational power amplifier (OPA) in the form of an analog voltage ranging between 0 to 10 volts. The OPA will adjust the electric currents in the coils accordingly. As mentioned in Chapter 4, the system is supplied with two DC power supplies assembled on the positive junction of the amplifier while the negative amplifier's junction is grounded. This results in a current variation between ranges of 0 to 3.55(A) in each electromagnet. Due to considerations such as cost and compatibility with other hardware, the amplifier is a semi-active non-inverting type with an active control on the positive current flow to the electromagnets. For higher accuracies, the amplifier can be upgraded to an active type with the ability to control both the positive and negative current flows to the coils. This would bring the ability to control both the upward and downward magnetic force and improve the control performance. At the current configuration, the only downward force acting of the levitated object is the gravity.

In the 3 dimensional (3D) position control, the controller receives three position commands corresponding to the desired position of the levitated object in the x, y, and z directions and separately adjusts electrical currents in multiple electromagnets. Such a system is called a multi-input-multi-output (MIMO) control system [127].

Although the final goal of the control design for the levitated object is to achieve an accurate positioning performance in three dimensions, in practice, the effort of the controller designs has to be focused on stabilizing the position of the levitated object in the vertical (z) direction.

Since the weight of the object is always opposing the magnetic force, practical observations showed that the controller design in the z direction is more challenging than the controller design in the x and y directions. Therefore, as a methodology of design, the design priority was given to stabilizing the system in the z direction. Once the controller was designed for the z direction, a mathematical method was employed to provide the ability to control the position of the object in the other two directions.

For the design in the z direction, the controller command is the desired position of the object in the z direction and the controller signal is one signal which is equally sent to all the electromagnets in the magnetic drive unit. Therefore, the system will be reduced to a single-input-single-output (SISO) [127] type. In the following sections, different controllers are mentioned and their performance is discussed. In all the experiments presented in this chapter, the levitated object is a small 1(cm) x 1(cm) cylindrical permanent magnet with the constant mass of 6.59(gr).

6.2. PID Control of the Levitated Object

A proportional-integral-derivative controller (PID controller) is an effective control strategy widely used in industrial control systems. A PID controller attempts to correct the error between a measured process variable and a desired set-point through closed loop calculation of the control signal.

Calculation of the control signal involves three separate parameters; the proportional gain K_p, the integral gain K_i, and derivative gain K_d. The control signal is a weighted sum of the error, its integral over the time and its derivative with respect to time as:

$$u(t) = K_p e(t) + K_i \int_0^t e(\tau) d\tau + K_d \left(\frac{d}{dt} e(t) \right) \tag{6-1}$$

where $e(t)$ is the error and $u(t)$ is the control signal. In the magnetic levitation device, the error $e(t)$ is calculated as:

$$e(t) = z_{cmd}(t) - z(t) \tag{6-2}$$

where z_{cmd} is the desired position command and z is the position of the levitated object read by the lasers.

Performance of the PID controller can be adjusted via tuning its three constants. One of the advantages of the PID controller is that its gain adjustment can be done without presence of the systems model. There are several methods for tuning a PID loop. The most effective methods generally involve the development of some form of process model, and adjusting gains K_p, K_i, and K_d based on the dynamic model parameters.

In practice, trial and error adjustment can be very useful although is not repeatable. An example of such adjustment is illustrated in Figure 6-2. Although the controller performance shown in this figure is not optimal, it shows the applicability of practical tuning of the controller gains. The gains found for this system are $K_p = 0.334$, $K_i = 0.007$, and $K_d = 0.001$.

The derivative gain K_d was found relatively smaller than the other two gains as the derivative term is very sensitive to the measurement error and can make the system unstable. The performances of the PID controller in tracking a negative step response and a ramp input command are shown in Figure 6-3 and Figure 6-4 respectively.

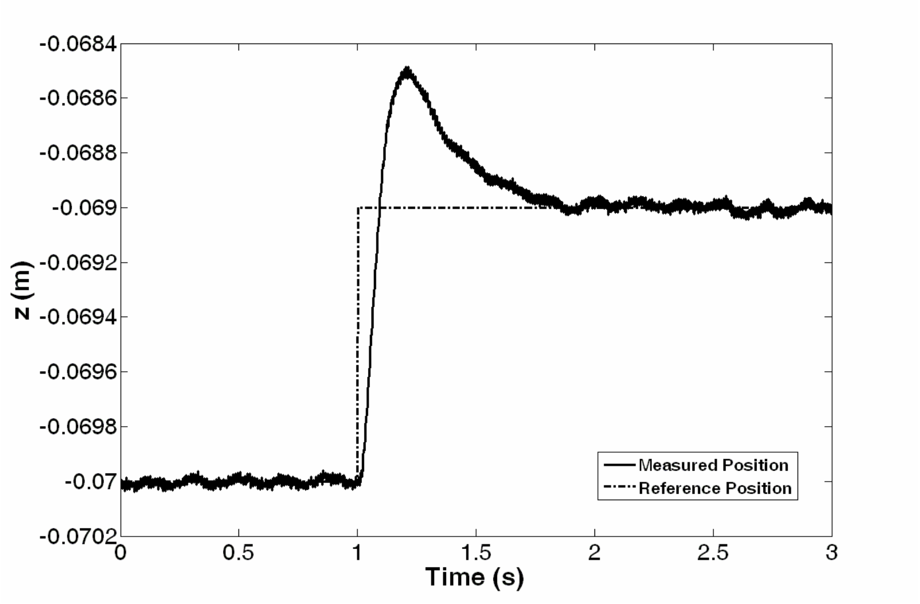

Figure 6-2: Step response of the system with PID controller for a positive step command.

(Kp = 0.334, Ki = 0.007 , Kd = 0.001)

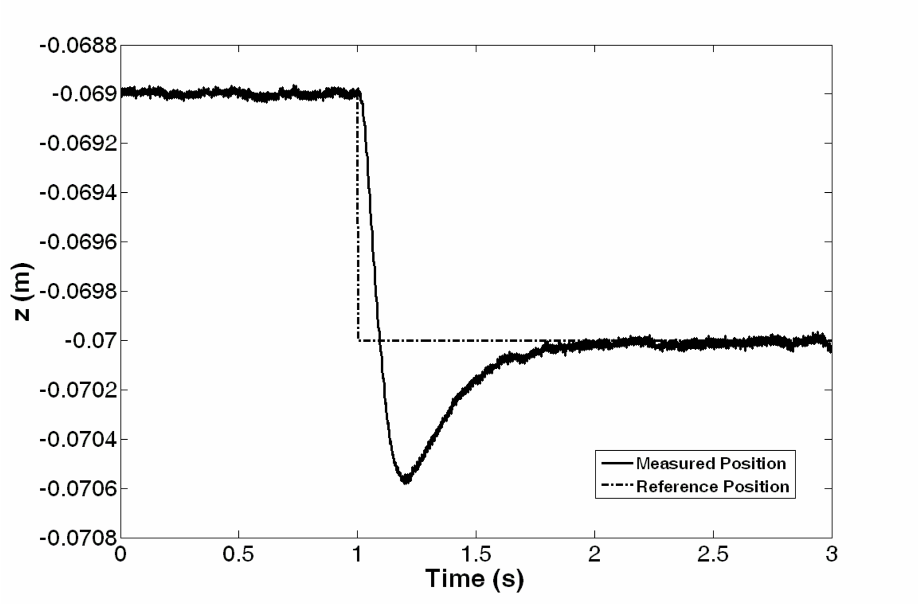

Figure 6-3: Step response of the system with PID controller for a negative step command.

(Kp = 0.334, Ki = 0.007 , Kd = 0.001)

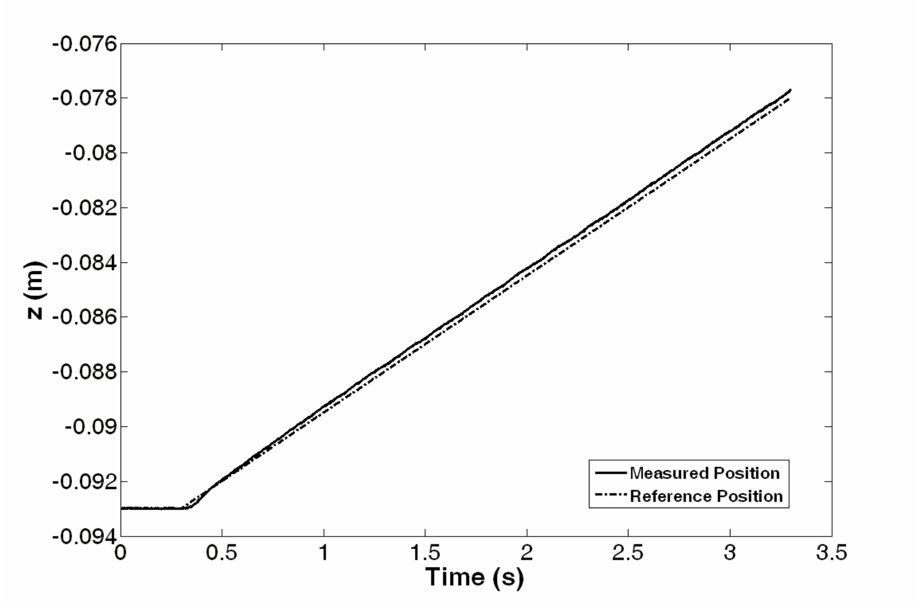

Figure 6-4: Ramp response of the system with PID controller (Kp = 0.334, Ki = 0.007 , Kd = 0.001).

In practice, when only the PID controller is used for the levitation system, it is seen that the system is very sensitive to the changes made in the controller gains. An effective method to increase the controller's performance and stability is to add the controller's signal to a feed-forward signal and use the combined signal as the control command.

The feed-forward value can provide a major portion of the control signal. The controller can then be used to compensate the remaining error between the desired set-point and the actual system's position.

Since the feed-forward output is not a function of the process feedback, it will not cause any oscillations or instability, thus improving the system response. In the next section, the feed-forward control will be presented.

6.3. Feed-Forward Control of the Levitated Object

In order to generate an appropriate feed-forward signal, a mathematical model of the system is required. The dynamic model of the system is recalled from the previous chapters as:

$$\left(\alpha z+\beta\right)\left(1-e^{\frac{-1}{\tau}t}\right)u-mg=m\ddot{z} \tag{6-3}$$

where α , β , and τ are three constant coefficients, m is the mass of the levitated object, g is the acceleration of gravity, z is the position of the levitated object, $\ddot{z}$ is the acceleration of the levitated object and u is the controller command. In the Laplace domain, the transfer function between the location of the levitated object, i.e. z, and the current in the coils, i.e. I, is obtained from Eq. (6-3) as:

$$G_p(s) = \frac{z(s)}{I(s)} = \frac{\alpha z_0 + \beta}{\left(ms^2 - \alpha I_0\right)(1+\tau s)} = \frac{C_1}{\left(ms^2 + C_2\right)(1+\tau s)} \tag{6-4}$$

where,

$$C_1 = \alpha z_0 + \beta \tag{6-5}$$

$$C_2 = -\alpha I_0 \tag{6-6}$$

and I_0 and z_0 represent the electric current and position of the levitated object at a steady state operating condition. The transfer function of a regular PID controller is given as:

$$G_c(s) = \frac{K_2 s^2 + K_1 s + K_I}{s} \tag{6-7}$$

where, K_1 is the proportional gain, K_2 is the derivative gain and K_I is the integrator gain. Using this PID controller, the closed-loop transfer function of the levitation system is obtained as:

$$G_{CL}(s) = \frac{C_1\left(K_2 s^2 + K_1 s + K_I\right)}{\tau m s^4 + m s^3 + \left(K_2 C_1 + \tau C_2\right)s^2 + \left(K_1 C_1 + C_2\right)s + C_1 K_I} \tag{6-8}$$

Where the values of gains K_1, K_2 and K_I should be adjusted so that the closed loop poles of the system are mapped to stable regions of the left half plane. In order to ease the control design process, Eq. (6-8) can be simplified by assuming $\tau = 0$. This assumption will simplify Eq. (6-3) to:

$$(\alpha z + \beta)u - mg = m\ddot{z} \tag{6-9}$$

The assumption of $\tau = 0$ will simplify the controller design process without a considerable effect on the overall performance of the closed loop system. For a position command z_c , we can define the state variables x_1 , x_2 , and x_3 as:

$$\begin{aligned} x_1 &= z - z_c \\ x_2 &= \dot{z} \\ x_3 &= \int \left(z - z_c \right) dt \end{aligned} \tag{6-10}$$

Therefore, the state space form of Eq. (6-9) can be written as:

$$\begin{aligned} \dot{x}_1 &= x_2 \\ \dot{x}_2 &= \frac{\alpha}{m}\left(x_1 + z_c \right) u + \frac{\beta}{m} u - g \\ \dot{x}_3 &= x_1 \end{aligned} \tag{6-11}$$

The equilibrium point of Eq. (6-11) is found as,

$$\begin{aligned} x_1 &= 0 \\ x_2 &= 0 \\ x_3 &= 0 \\ u_{ss} &= \frac{mg}{\alpha z_c + \beta} \end{aligned} \tag{6-12}$$

Where, u_{ss} is the steady-state value of the controller signal which takes the system into its equilibrium point. The state space realization of Eq. (6-11) is obtained by linearizing this equation [128] at an operating point of $u = u_0$ and $z = z_0$ as,

$$\mathbf{A} = \begin{bmatrix} 0 & 1 & 0 \\ \dfrac{\alpha g}{\alpha z_c + \beta} & 0 & 0 \\ 1 & 0 & 0 \end{bmatrix} \quad , \quad \mathbf{B} = \begin{bmatrix} 0 \\ \dfrac{\alpha z_c + \beta}{m} \\ 0 \end{bmatrix} \tag{6-13}$$

Using full state feedback gains, $\mathbf{K} = \left[K_1 \quad K_2 \quad K_I \right]$, the total controller signal is obtained as:

$$u = u_{ss} - \mathbf{KX} \tag{6-14}$$

where $\mathbf{X} = \left[x_1 \quad x_2 \quad x_3 \right]^T$ is the state vector. For the desired poles at σ_{d1}, σ_{d2}, and σ_{d3}, the pole placement controller design yields:

$$K_i = \frac{-m \ \sigma_{d1}\sigma_{d2}\sigma_{d3}}{C_1} \tag{6-15}$$

$$K_1 = \frac{m\left(\sigma_{d1}\sigma_{d2} + \sigma_{d1}\sigma_{d3} + \sigma_{d2}\sigma_{d3} \right) - C_2}{C_1} \tag{6-16}$$

$$K_2 = \frac{-m\left(\sigma_{d1} + \sigma_{d2} + \sigma_{d3}\right)}{C_1} \tag{6-17}$$

where,

$$C_1 = \alpha z_0 + \beta \tag{6-18}$$

and,

$$C_2 = -\alpha u_0 \tag{6-19}$$

In order to ensure that the simplifying assumption $\tau = 0$ does not jeopardize the stability of the control system, application of the Routh-Hurwitz stability criterion to Eq. (6-8) yields that:

$$K_2 > \tau K_1 \tag{6-20}$$

$$K_I < \frac{\left(K_1 C_1 + C_2\right)\left(K_2 - \tau K_1\right)}{m} \tag{6-21}$$

Equations(6-15), (6-16), and (6-17) are the pole placement relationships resulting in the calculation of the controller gains. A controller was designed for the desired poles of $\sigma_{d1} = -44$, $\sigma_{d2} = -8$ and $\sigma_{d3} = -0.6$ which resulted in the approximate controller gains of $K_1 = 65$, $K_2 = 6$, and $K_i = 25$.

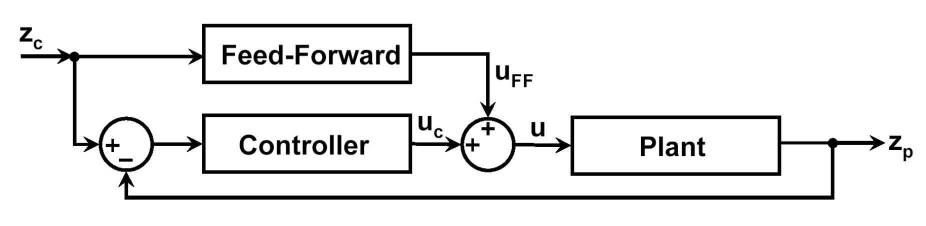

Figure 6-5: Schematic diagram of the feed-forward controller.

The u_{ss} signal can be generated as a feed-forward signal in the actual implementation of the controller i.e.:

$$u_{FF} = u_{ss} = \frac{mg}{\alpha z_c + \beta} \tag{6-22}$$

Figure 6-5 shows the schematic diagram of the feed-forward controller. The state variable x_3 is defined as the integral of the positioning error to cope with the steady state positioning of the control system. Figure 6-6 shows the response of the state feedback controller without an integrator effect in following a positive step command. As seen in this figure, since the system is type zero, there exists a steady-state error in the response of the system.

Another issue to be mentioned is the slight fall in the response of the system at the time at which the step command is issued. A step command from $z = -0.073(m)$ to $z = -0.070(m)$ will result in a sudden decrease in the feed-forward term. Eventually the control signal will fall momentarily and the levitated object will experience less magnetic force and starts to fall until the controller adjusts the signal.

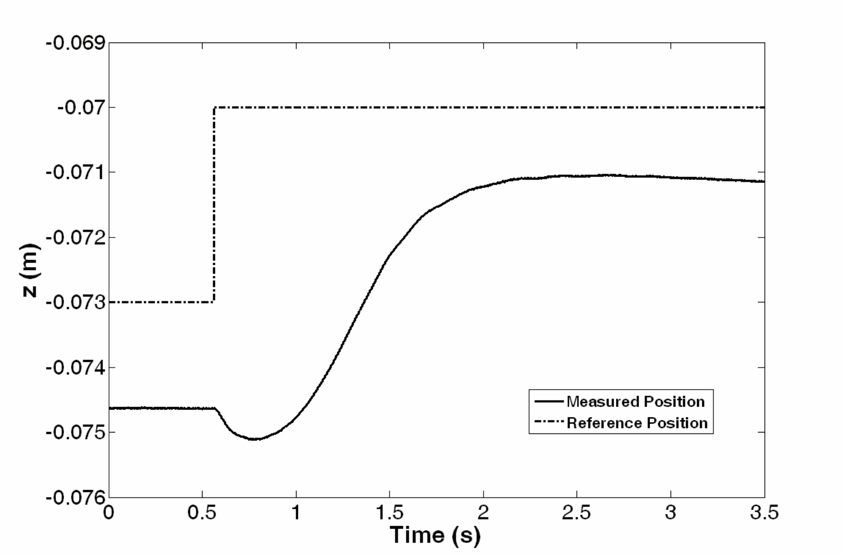

Figure 6-6: Step response of the system with state feedback controller for a positive step command.

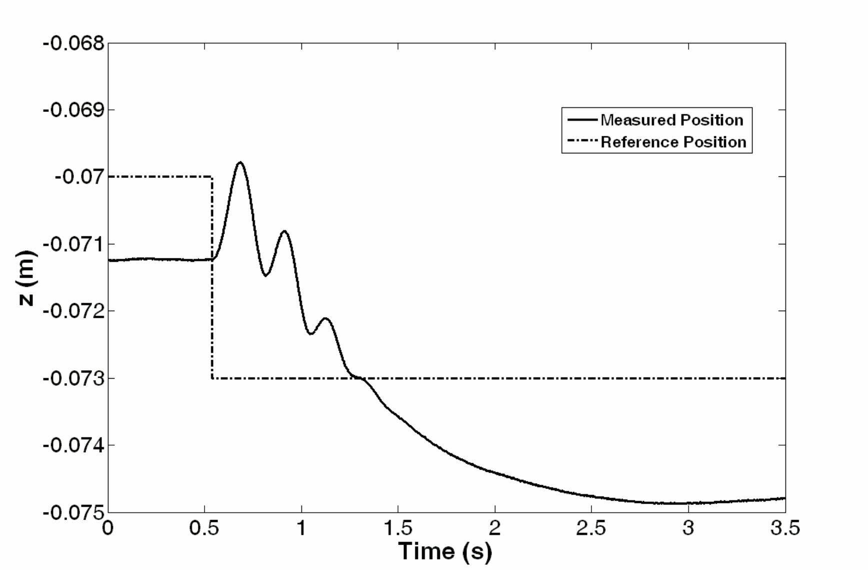

Figure 6-7: Step response of the system with state feedback controller for a negative step command.

Also, the feed-forward signal will encounter a sudden increase at a time of a negative step command. Figure 6-7 illustrates the response of the system to a step response from $z = -0.070(m)$ to $z = -0.073(m)$. Due to this sudden increase, the object will experience a higher magnetic force and will move up until the controller adjusts the signal.

In this case, in order to address this problem, the feed-forward term can be converted into a dynamic signal through pre-filtering the feed-forward signal or using a feedback linearization method. In the next section, a model-reference feed-forward controller is presented and its performance is discussed.

6.4. Model-Reference Feed-Forward Controller

Figure 6-8 illustrates the schematic of the model-reference feed-forward controller.

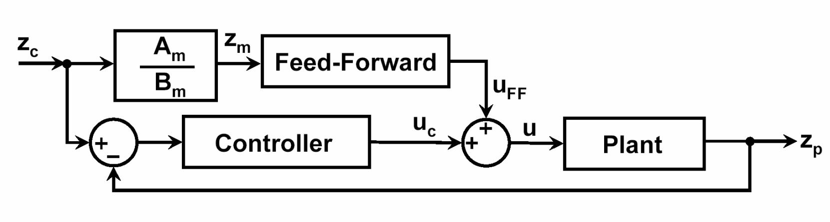

Figure 6-8: Schematic diagram of the model-reference feed-forward controller.

Polynomials $\mathrm{A_m}$ and $\mathrm{B_m}$ are the nominator and denominator of the reference model respectively. The choice of the reference model is based on the desired performance of the system as well as the maximum speed of the plant in following the reference model.

The transfer function of the reference model is selected to be a second order standard transfer function as:

$$\mathrm{M(s)}=\frac{\mathrm{A_m(s)}}{\mathrm{B_m(s)}}=\frac{\omega_n^2}{s^2+2\xi\omega_n s+\omega_n^2} \tag{6-23}$$

where ω_n and ξ are the natural frequency and damping ratio respectively. Assuming $\tau = 0$, the simplified form of Eq. (6-8) is obtained as:

$$\mathrm{G_c(s)} = \frac{C_1\left(K_2 s^2 + K_1 s + K_i\right)}{m s^3 + C_1 K_2 s^2 + \left(C_1 K_1 + C_2\right)s + C_1 K_i} \tag{6-24}$$

Figure 6-9 shows the step response simulation of the system in Eq. (6-24) for the values presented in Table 6-1.

Figure 6-10 compares the response of the simulated model with the response of the actual system. As seen in this figure, response characteristics such as overshoot, steady-state value, and settling time of both systems are very close. Both lines show an overshoot of approximately 50%. In terms of settling time, the actual system showed a settling time of 2.65(s) compared with the 3.8(s) of the simulated model. This difference between the actual and simulated system's performance has reasons such as un-modeled dynamics, feed-forward effect, delay in the coils and power amplifier, and nonlinearities in the actual system. However, the similarities in the performance of the two systems verify the validity of the assumption in neglecting the exponent term effect for the controller design process.

Table 6-1: The numerical values of the model and controller parameters.

Parameter	**Value**	**Description**
m	$0.00659(\mathrm{kg})$	Mass of the levitated object
α	$1.1112(\mathrm{N}\cdot\mathrm{A}^{-1}\cdot\mathrm{m}^{-1})$	Magnetic force coefficient
β	$0.1352(\mathrm{N}\cdot\mathrm{A}^{-1})$	Magnetic force coefficient
z_0	$-0.07(\mathrm{m})$	Operating point position
u_0	$1.126(\mathrm{A})$	Operating point current
K_1	$65(\mathrm{A}\cdot\mathrm{m}^{-1})$	Proportional gain
K_2	$6(\mathrm{A}\cdot\mathrm{s}\cdot\mathrm{m}^{-1})$	Derivative gain
K_i	$25(\mathrm{A}\cdot\mathrm{m}^{-1}\cdot\mathrm{s}^{-1})$	Integrator gain

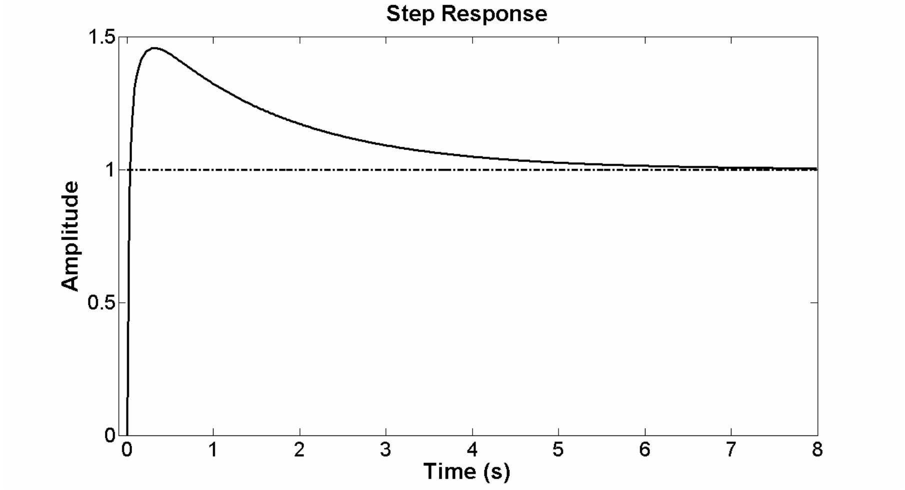

Figure 6-9: Step response simulation of the system for K_1=65, K_2=6 and K_i=25 in MATLAB.

For the actual controller implementation, the reference model characteristics have to be selected. The response characteristics of the reference model such as its settling time and its overshoot can be set through proper adjustment of ω_n and ξ.

If the reference model is too fast for the system to follow, the system will fall behind the model. For very slow reference models, the feed-forward will basically slow down the system and increase the settling time of the device.

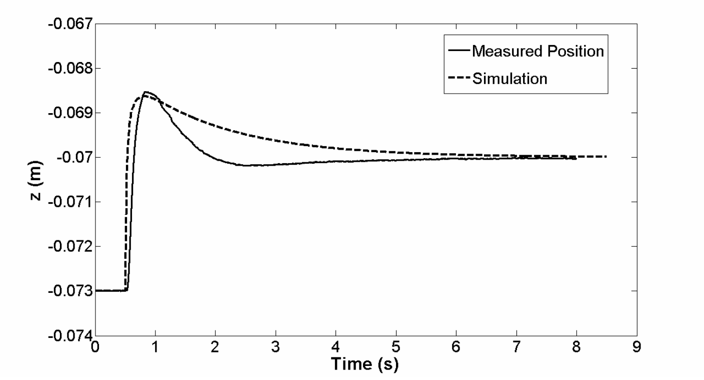

Figure 6-10: Comparison between the model and the actual system.

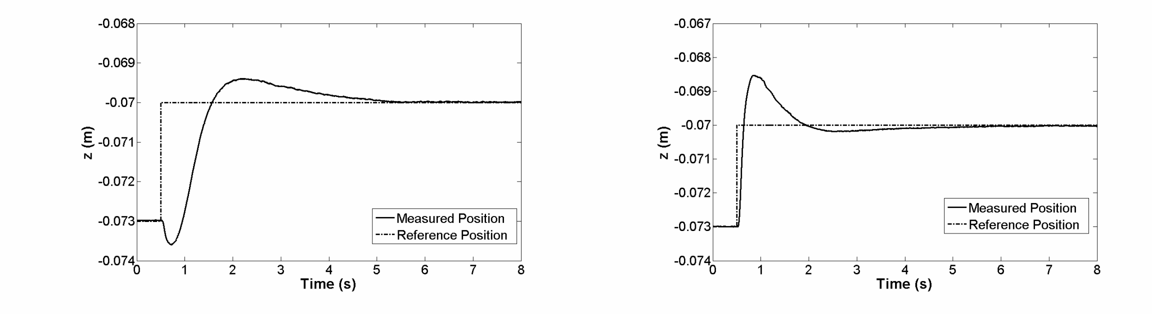

a) With out reference model. **b) With reference model.**

Figure 6-11: Step response of the feed-forward-PID controller for a positive step command.

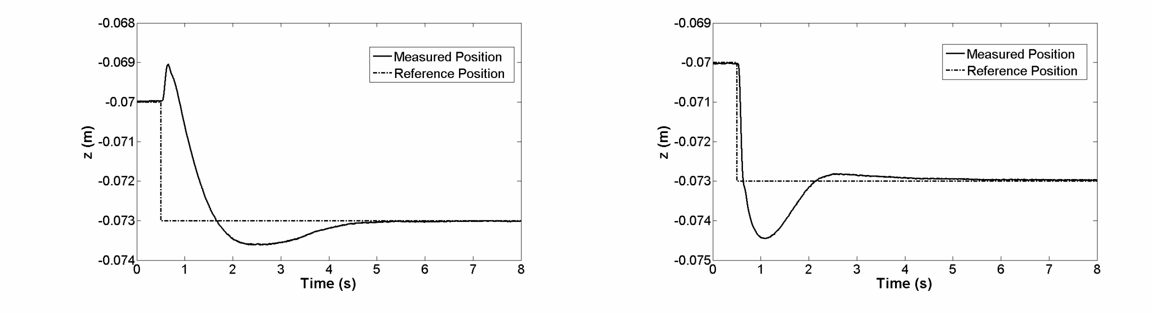

a) With out reference model. **b) With reference model.**

Figure 6-12: Step response of the feed-forward-PID controller for a negative step command.

Figure 6-11 demonstrates the performance of the actual system for the values listed in Table 6-1. The feed-forward signal is taken from a reference model with $\omega_n = 2.5\left(\text{rad/s}\right)$ and $\xi = 0.85$. In the absence of reference model, Figure 6-11(a), although the integrator gain compensates the steady-state error, the controller shows an undershoot at the time of a positive step command. In contrast, when the model reference is present, Figure 6-11(b), the undershoot issue in tracking a positive step command will be eliminated. As a result, the settling time of the system is reduced to less than half.

Figure 6-12 illustrates the positioning performance of the system for negative step commands. As it is seen in Figure 6-12(b), the model-reference feed-forward signal successfully eliminated the overshoot issue at the time of a negative step command.

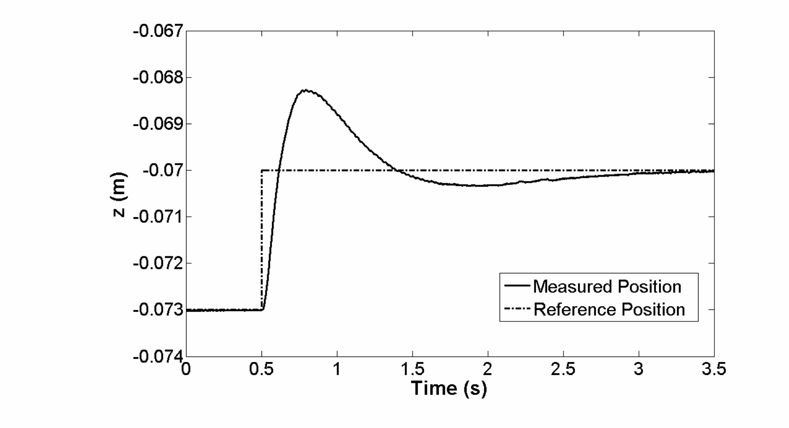

Figure 6-13: Step response of the feed-forward-PID controller for a positive step command.

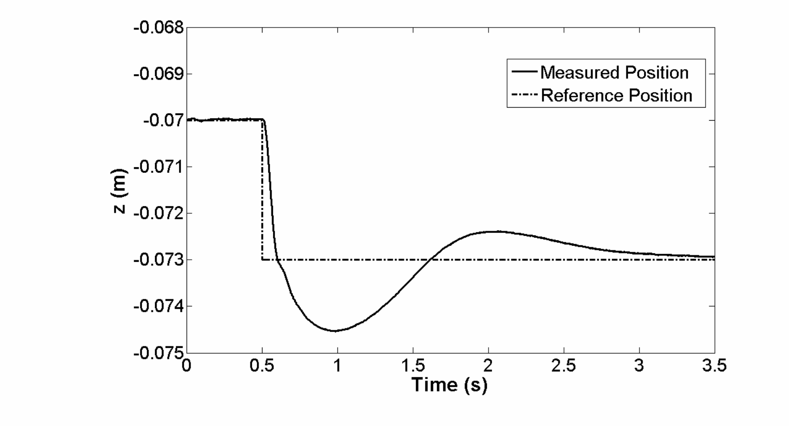

Figure 6-14: Step response of the feed-forward-PID controller for a negative step command.

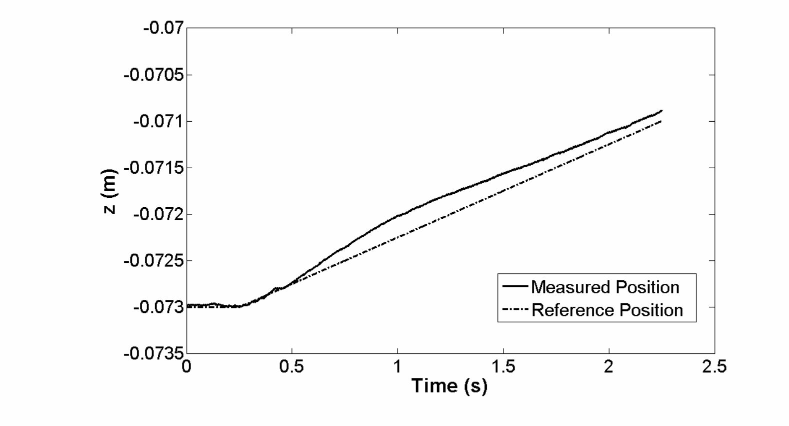

Figure 6-15: Ramp response of the feed-forward-PID controller.

Figure 6-13 and Figure 6-14 show the step response of the system for a controller with $K_1 = 65$, $K_2 = 6$, and $K_i = 100$. The feed-forward reference model characteristics are

$\omega_n = 2.5(\mathrm{rad/s})$ and $\xi = 0.85$. As it can be seen in these figures, there is a slight difference between the performance of the system in the positive and negative step responses. The difference is mainly due to the fact that the power amplifier used in the system has different response characteristics for positive and negative step responses.

Comparing the results in Figure 6-13 and Figure 6-11(b), it is inferred that increasing the integrator gain from $K_i = 25$ to $K_i = 100$, reduced the settling time of the system from 2.65 to 2.45 seconds. In contrast, it increased the overshoot from 49.1% to 57.3%. This settling time will result in a considerable error in the ramp response of the controller. The performance of the system in tracking ramp inputs is shown in Figure 6-15.

One method to increase the ramp performance is to reduce the settling time of the controller. This can be done through using higher integrator gains. However, the use of higher integrator gains will increase the overshoot of the controller which is not a desirable outcome.

In practice, the design of the controller is a compromise between faster settling behaviour or less over shoot. In the next two sections, two strategies are presented to either decrease the settling time or overshoot of the controller. Using a feedback linearization controller, the settling time is cut in half. Also, by utilizing a path planning model in commanding the feed-forward-PID controller, the overshoot is drastically reduced.

6.5. Feedback Linearization Controller

Feedback linearization is an approach used in controlling nonlinear systems. The idea of the feedback linearization is to use a proper feedback to cancel the nonlinear effects of the actual plant.

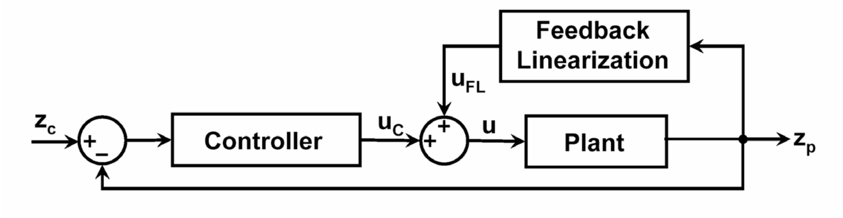

Figure 6-16: Schematic diagram of the feedback linearization controller.

The main identified nonlinearity in the system corresponds to the magnetic force which is obtained as:

$$F_{mag} = u\left(\alpha z + \beta\right) \tag{6-25}$$

In an ideal condition, where the system's model is perfect, the feedback linearization signal can be calculated as:

$$\mathrm{u}_{\mathrm{FL}} = \frac{mg}{\alpha z + \beta} \tag{6-26}$$

where z is the current position of the levitated object. Using this signal, the dynamic equation of the levitation in Eq. (6-3) will ideally reduce to:

$$\ddot{z} = 0 \tag{6-27}$$

However, since the model is not perfect, there is always a deviation between the actual system and the model. This will cause a positioning error in the control of the levitated object. If the model is fairly accurate, the feedback linearization signal will maintain a dominant portion of the actual controller signal required to stabilize the system.

In order to cope with the model inaccuracies, a PID controller is used in cooperation with the feedback linearization term. Let's call this controller FL-PID.

An experiment was performed to investigate the difference between the performance of the FL-PID controller with the performance of the model-reference feed-forward (FF-PID) controller.

In both experiments, the PID controller gains are set as $K_1 = 65$, $K_2 = 6$, and $K_i = 100$. The difference between the FF-PID and FL-PID controllers is the use of u_{FF} in Eq. (6-22) and u_{FL} in Eq. (6-26) respectively. Moreover, the FF-PID controller has a reference model with $\omega_n = 2.5\left(\mathrm{rad/s}\right)$ and $\xi = 0.85$ to eliminate the sudden changes in the feed-forward signal.

Figure 6-17 compares the performances of the FF-PID and FL-PID controllers for a positive step command. As seen in this figure, utilization of the feedback linearization term considerably reduced the overshoot and settling time of the system to 20.6% and 1.25(s) respectively.

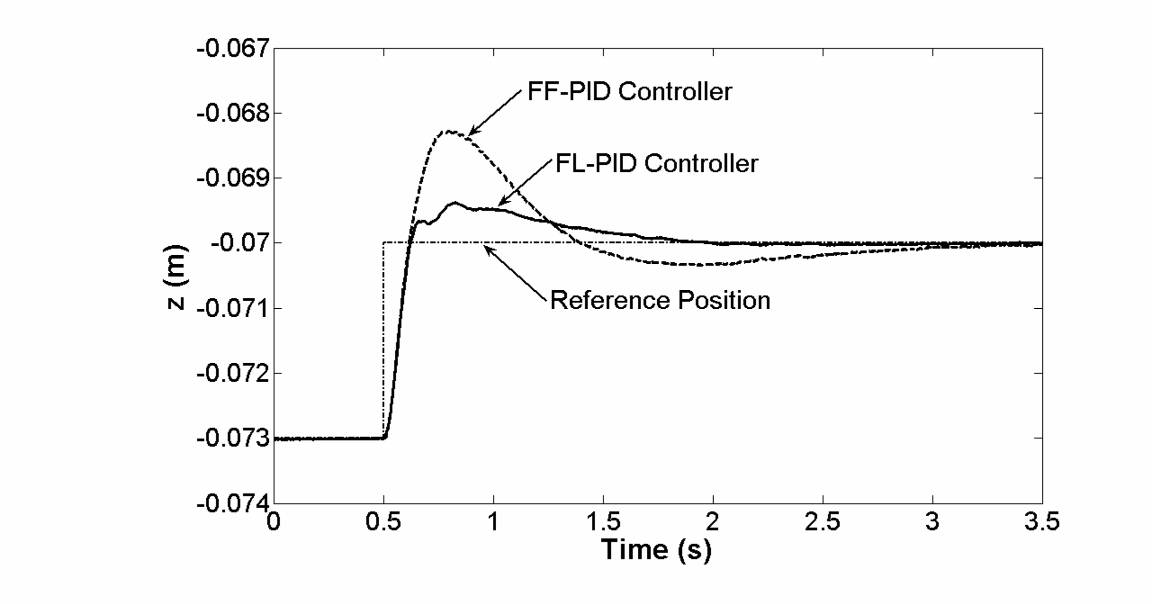

Figure 6-17: Comparison between the FL-PID and FF-PID controllers for a positive step response.

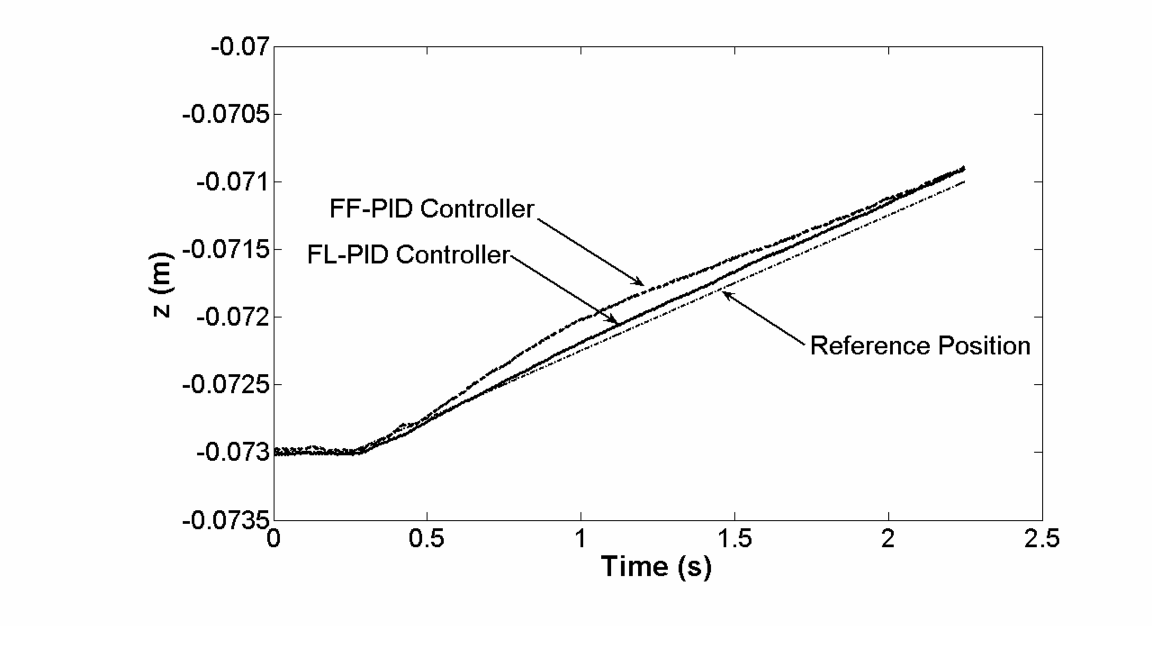

Figure 6-18: Comparison between the FL-PID and FF-PID controllers for a ramp response.

The FL-PID controller showed a significant advantage over the FF-PID controller in the ramp response too (Figure 6-18). Since the FL-PID controller has a smaller settling time, this controller has a better ramp response performance. In contrast, due to the dependency of the feedback linearization term to the position of the levitated object, the stability of the FL-PID controller has to be investigated considering u_{FF} as a component of the signal. This leads to a nonlinear stability analysis of the system which is presented in Appendix F.

6.6. Utilization of the Path-Planning Model in the Command Signal

As stated earlier, the controller design problem is usually a compromise between either a faster settling or less overshoot. If the overshoot factor is the dominant design criterion, an effective strategy to achieve a desired response is to utilize a path-planning model (PPM) in feeding the command signal to the system as shown in Figure 6-19.

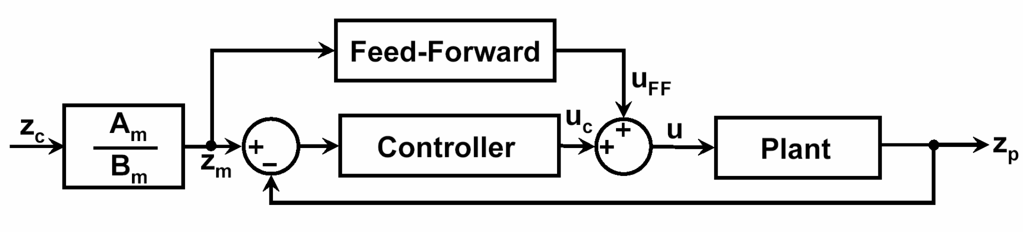

Figure 6-19: Utilization of the path planning in the command signal.

Let call the proposed controller as PPM-PID. This technique will significantly reduce the overshoot of the response however; the settling time will be adversely increased. The operator will send the command to PPM which eventually calculates the planned command and sends it to the system.

In order to minimize the overshoot of the response in the magnetic levitation device, the PPM was selected as an over damped second order system with $\omega_n = 5\left(\text{rad/s}\right)$ and $\xi = 1.05$ in Eq. (6-28).

$$G_{PPM}\left(s\right)=\frac{z_m\left(s\right)}{z_C\left(s\right)}=\frac{\omega_n^2}{s^2+2\xi\omega_n s+\omega_n^2} \tag{6-28}$$

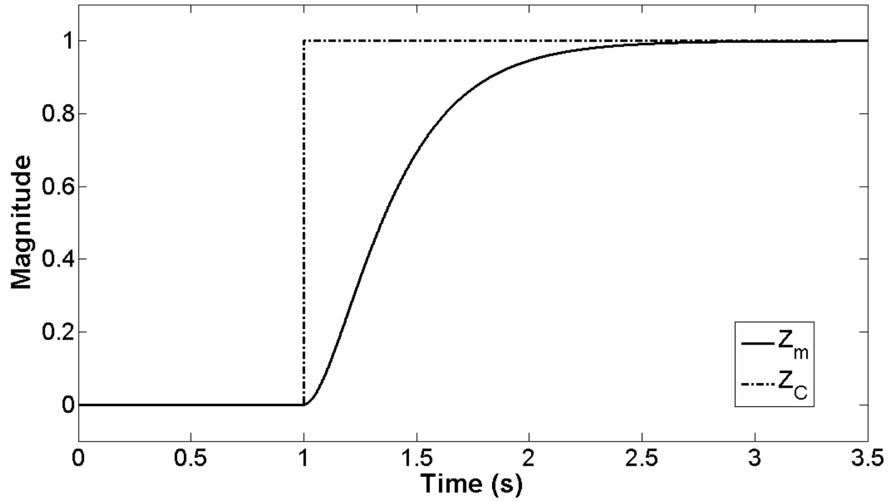

Figure 6-20: Step response of the path-planning model.

Figure 6-20 shows the step response of the path-planning model. As seen, the model has a settling time of 1(s) with no overshoot. As the PPM provides a smooth transition between the step commands, there is no need to include a separate model for the feed-forward signal.

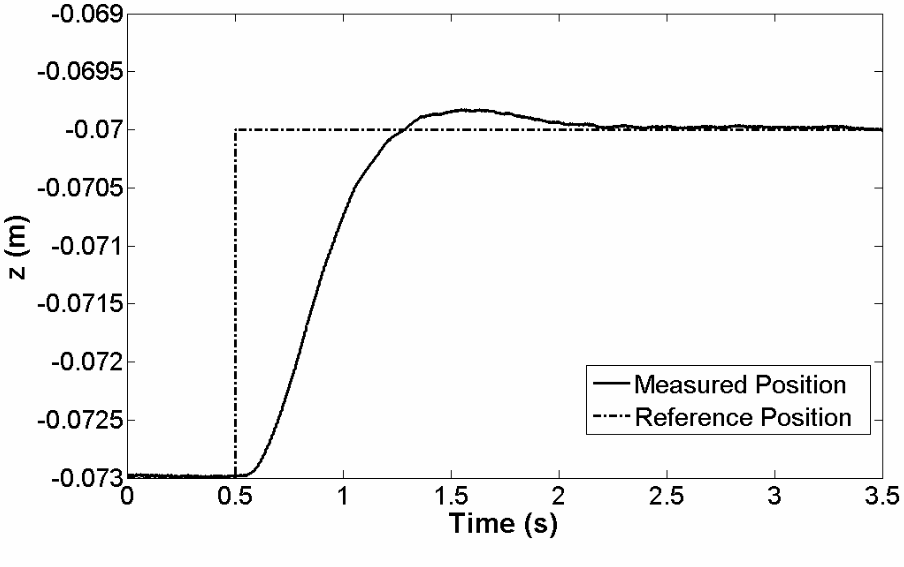

Figure 6-21: Step response of the PPM-PID controller for a positive step command.

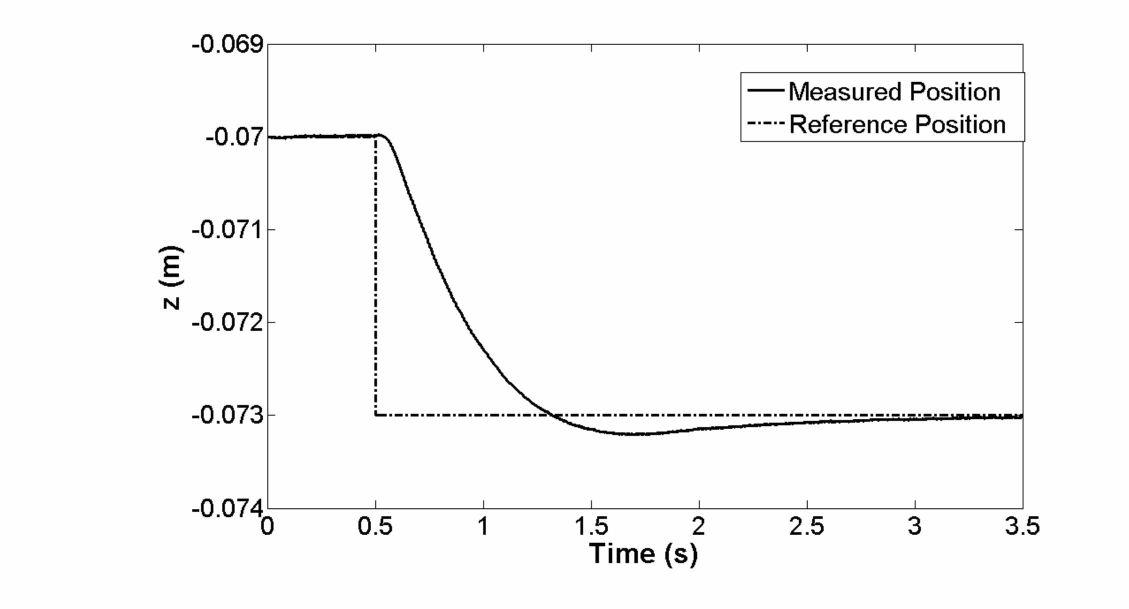

Figure 6-22: Step response of the PPM-PID controller for a negative step command.

Using the same controller gains as the previous section, the step response of the PPM-PID controller is shown in Figure 6-21 and Figure 6-22. The proposed controller has a settling time of 1.5(s) and overshoot of 7% compared with 1.25(s) and 20.6% for FL-PID and 2.45(s) and 57.3% for FF-PID controllers. Table 6-2 compares the settling time, overshoot and positioning RMS error of the proposed controllers for $K_1 = 65, K_2 = 6$, and $K_i = 100$.

Table 6-2: Comparison between the settling time and overshoot of the proposed controllers.

Controller Type:	**FF-PID**	**FL-PID**	**PPM-PID**
Settling time (s)	2.45	1.25	1.5
Overshoot (%)	57.3	20.6	7
RMS Error (μm)	18.04	11.56	8.67

6.7. Discussion

Three types of controllers are presented in this chapter. Although all of the methods were using the same PID controller, they illustrated different response characteristics in experiments, as shown in the following figures.

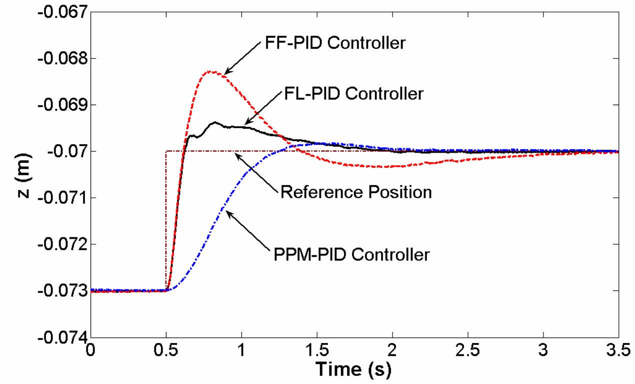

Figure 6-23: A comparison between the controllers' responses to a positive step command.

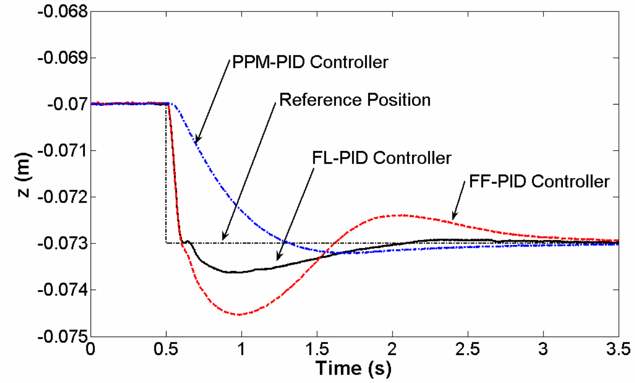

Figure 6-24: A comparison between the controllers' responses to a negative step command.

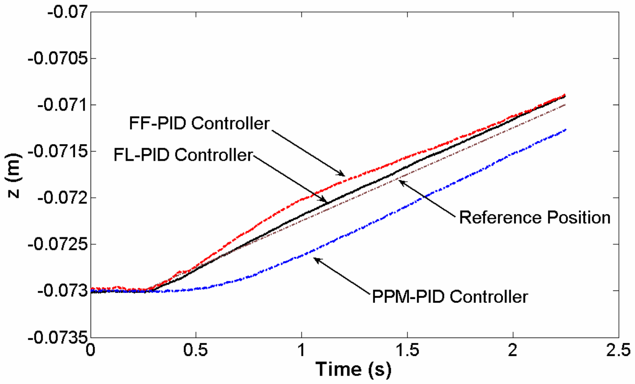

Figure 6-25: A comparison between the controllers' responses to a ramp command.

Comparing the three control methods, the FL-PID controller showed the fastest settling behaviour which led to the best ramp performance. On the other hand, this controller has a higher overshoot in comparison with PPM-PID. In terms of positioning accuracy, PPM-PID is the most accurate controller followed by FL-PID and FF-PID.

Considering both tracking performance and accuracy, the FL-PID controller was selected for the position control of the levitated microrobot.

It is important to note that the controllers presented in this chapter are suitable for the case in which the weight of the levitated object is constant. If the levitated object is a microrobot equipped with micro-grippers, it will experience a change in its weight during the time of grasping or releasing payloads.

In this case, controller parameters have to be adjusted in a way to compensate for the parameter change in the system and maintain the same level of accuracy.

Chapter 7

Adaptive Controller Design for the Levitated Object

7.1. Introduction

In this chapter an adaptive controller is designed for the magnetic levitation system. The levitated object in this article is a microrobot equipped with an infrared sensor and a micro-gripper. Based on the recommendation made in the previous chapter, a feedback linearization PID (FL-PID) controller was designed for positioning the micro-robot with and without a payload.

Model uncertainties and the change in the mass of the robot are addressed with a model reference adaptive feedback linearization (MRAFL) control law for vertical position control. Experimental results are presented that verify the performance using the adaptive controller.

It is shown that the MRAFL controller enables the micro-robot to pick up and transport a payload as heavy as 30% of its own weight while maintaining a high level of positioning accuracy.

In all the experiments presented in this chapter, the microrobot's weight was 28(gr) and the payload weighs 8(gr). A FL-PID controller was designed for the system and its performance was investigated with and without the payload. Figure 7-1 shows the performance of the proposed FL-PID controller when the payload is changed. A relatively large increase in the overshoot and settling time of the controller is seen in this case.

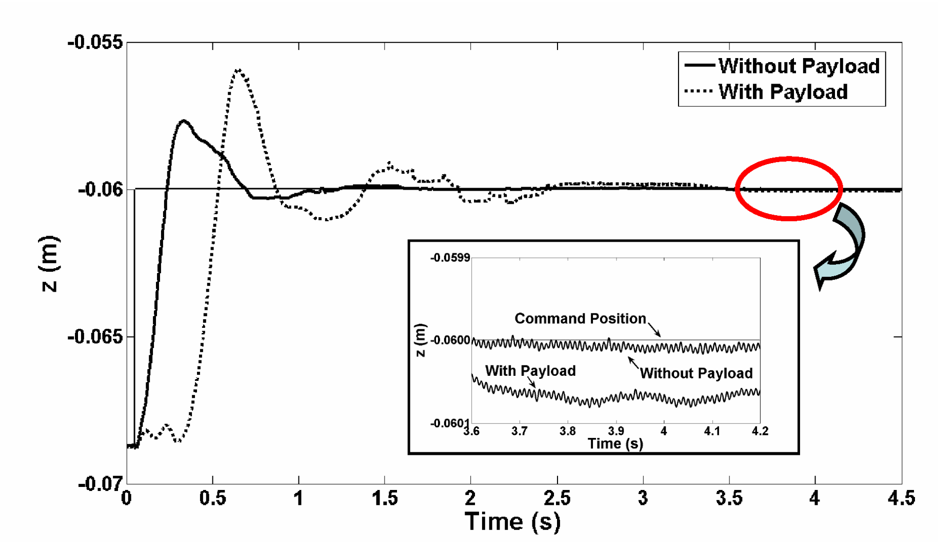

Figure 7-1: Performance of the FL controller when payload is changed.

As it is seen in Figure 7-1, for the parameters K_1, K_2 and K_i set as 40, 5 and 200 respectively, there is a satisfactory response in absence of a payload. However, the change in the mass of the microrobot degrades the accuracy of the feedback linearization and affects the overall positioning performance. In order to eliminate this problem, an adaptive control law was used which will be discussed in the next section.

7.2. Model Reference Adaptive Feedback Linearization (MRAFL) Controller

Investigating the control signal of the FL-PID controller, it is realized that in the absence of payload, approximately 85% of the control signal is due to the feedback linearization term. Figure 7-2 illustrates the contribution of the feedback linearization signal to the total control signal in the presence and absence of the payload.

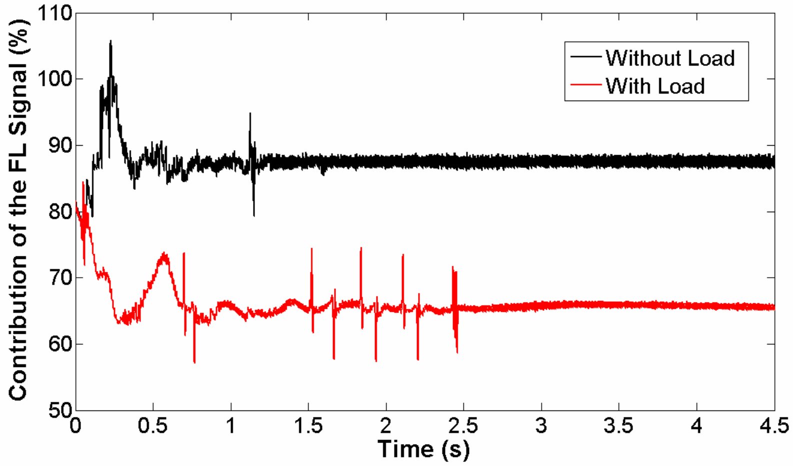

Figure 7-2: Contribution of the feedback linearization signal to the total control signal.

As is seen, by applying the payload, the feedback linearization contribution falls from 85% to 65%. This shows that the feedback linearization term has always a dominant effect in the total controller effort and hence, was chosen as the adaptation target.

Figure 7-3 shows the block diagram of a model reference adaptive control strategy applied to the system. The model reference adaptive system is one of the main approaches to adaptive control. In this technique, the desired performance of the system is expressed in terms of a reference model, which gives the desired response to a command signal [129]. The error ε is the difference between the outputs of the system and the reference model and is called the augmented error.

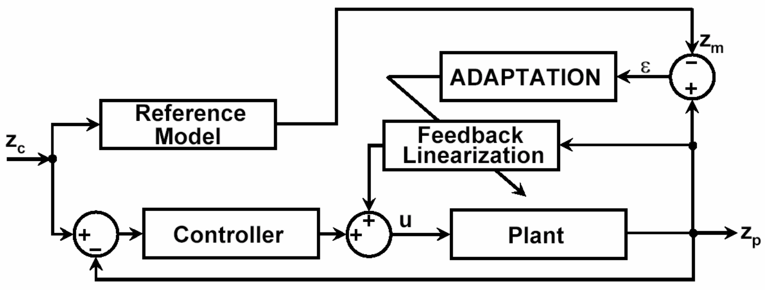

Figure 7-3: Block diagram of the MRAFL controller.

The adaptation of the controller parameters ϕ_i is made by implementation of a continuous hill-climbing technique [130]. The criterion to be minimized is:

$$I = \frac{1}{2}\int_{t}^{t+\Delta t} \varepsilon^2(\tau)\,d\tau \tag{7-1}$$

where $\varepsilon(\tau)$ is the augmented error at time τ and is defined as:

$$\varepsilon(\tau) = z_p(\tau) - z_m(\tau) \tag{7-2}$$

The adjustment of the controller parameters is made using the steepest descent technique:

$$\Delta\phi_i(t) = -\gamma_\phi \frac{\partial I}{\partial \phi_i} \tag{7-3}$$

where γ_ϕ is a constant number determining the rate of gradient adaptation and is called the adaptation constant. For an infinitesimal period of time and slow adaptation, Eq. (7-3) yields:

$$\dot{\phi}_i(t) = -\gamma_\phi \frac{\partial}{\partial t}\frac{\partial I}{\partial \phi_i} = -\gamma_\phi \frac{\partial}{\partial \phi_i}\frac{\partial I}{\partial t} \tag{7-4}$$

Combining Eq. (7-1) and (7-4) it follows that:

$$\dot{\phi}_i(t) = -\gamma_\phi \varepsilon(t)\frac{\partial z_p(t)}{\partial \phi_i} \tag{7-5}$$

where $\partial z_p(t)/\partial\phi_i$ is called the sensitivity function. Equivalently, the parameter adaptation law is written in the integral form as:

$$\phi_i(t) = -\gamma_\phi \int_0^t \varepsilon(t)\frac{\partial z_p}{\partial \phi_i}\,dt + \phi_i(0) \tag{7-6}$$

Since in the feedback linearization compensator, the most effective uncertainty is the mass of the microrobot, it was decided that the adaptation algorithm only updates the mass of the microrobot. The sensitivity of the ideal system's response to the mass variation can be calculated from the ideal steady-state controller signal. Recalling the steady-state equation of the system, if the nonlinear model is accurate, position of the levitated object will be obtained as:

$$z_p = \frac{mg}{\alpha u} - \frac{\beta}{\alpha} \tag{7-7}$$

Substituting Eq.(7-7) in Eq. (7-6), the mass adaptation law is obtained as:

$$m(t) = -\gamma \int_0^t \varepsilon(t)\frac{g}{\alpha V}\,dt + m(0) \tag{7-8}$$

where $m(0)$ is the initial value for the mass and was set equal to the mass of the robot without payload. The reference model was selected as a second order stable system:

$$G_m(s) = \frac{\omega_n^2}{s^2 + 2\xi\omega_n s + \omega_n^2} \tag{7-9}$$

where ξ and ω_n are the design parameters and determine the response characteristics of the reference model.

In general, increasing ω_n will result in a faster step response and increasing ξ will result in a slower step response and a smaller overshoot. It was seen that using reference models with very fast behaviors for the studied test rig will cause an improper performance of the adaptive system.

Figure 7-4 illustrates the parameter adaptation period of the MRAFL controller with design parameters $\omega_n = 2.85$, $\xi = 0.95$ and adaptation constant $\gamma = 0.65$. As is seen in this figure, in the presence of the payload of 8(gr), the system falls behind the command input until the adaptive controller adjusts the mass in the feedback linearization signal. This figure shows that the controller parameters are tuned real-time during the first step response to compensate the payload variation. In the second step input, the system accurately follows the step command regardless of the payload. The positioning error of Figure 7-4 is plotted in Figure 7-5 which shows the position errors are significantly reduced in the second step responses for both with and without a payload.

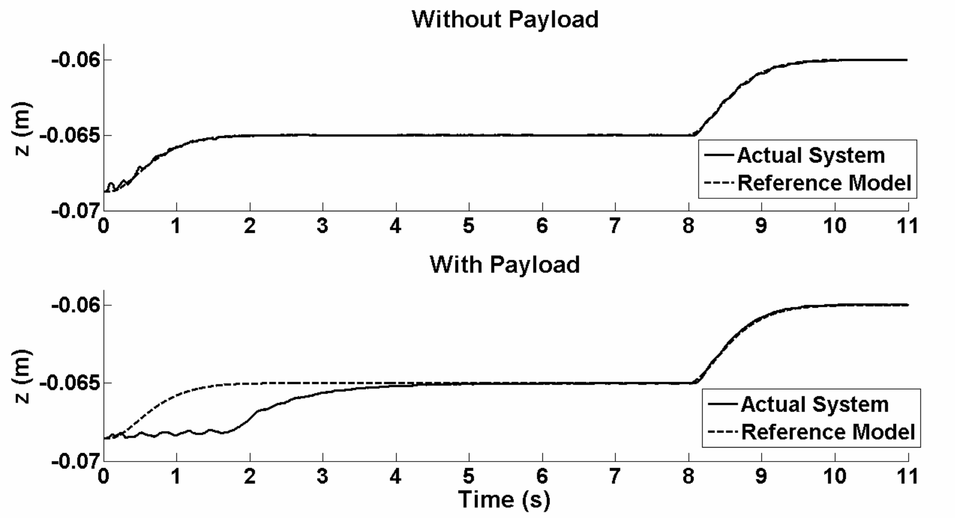

Figure 7-4: Step response of MRAFL controller during adaptation.

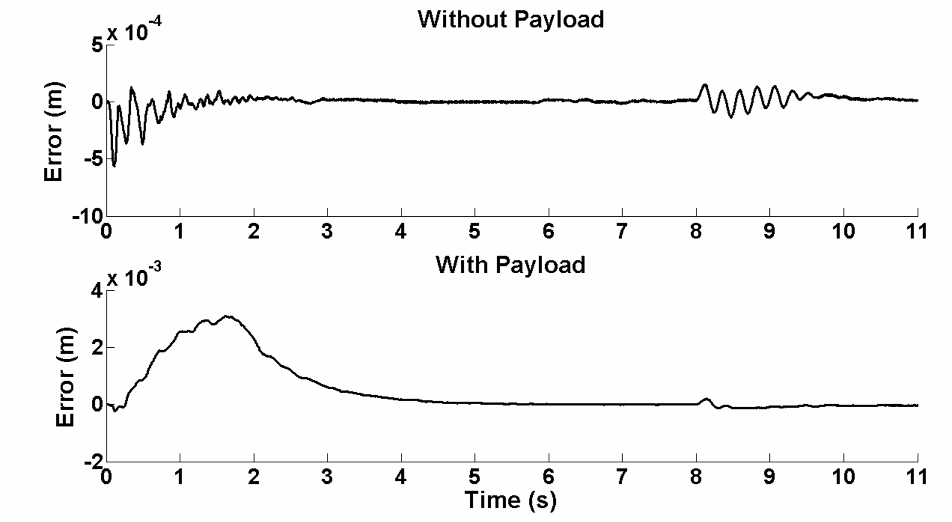

Figure 7-5: Positioning error of the step response in Figure 7-4.

The proposed adaptive controller has significantly reduced the percent of maximum overshoot (P.M.O.) and the percent of maximum undershoot (P.M.U.). Figure 7-6 shows that when the microrobot is carrying the payload, the adaptive controller is still maintaining an accurate positioning performance while tracking the model reference command. In another experiment, the capabilities of the MRAFL controller was examined in tracking a ramp input command as shown in Figure 7-7.

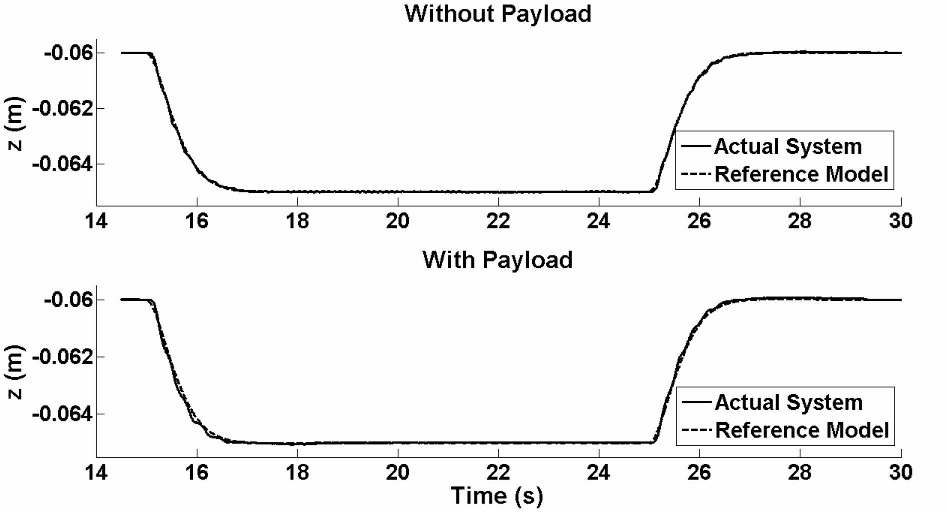

Figure 7-6: Step response of MRAFL controller after adaptation with and without a payload.

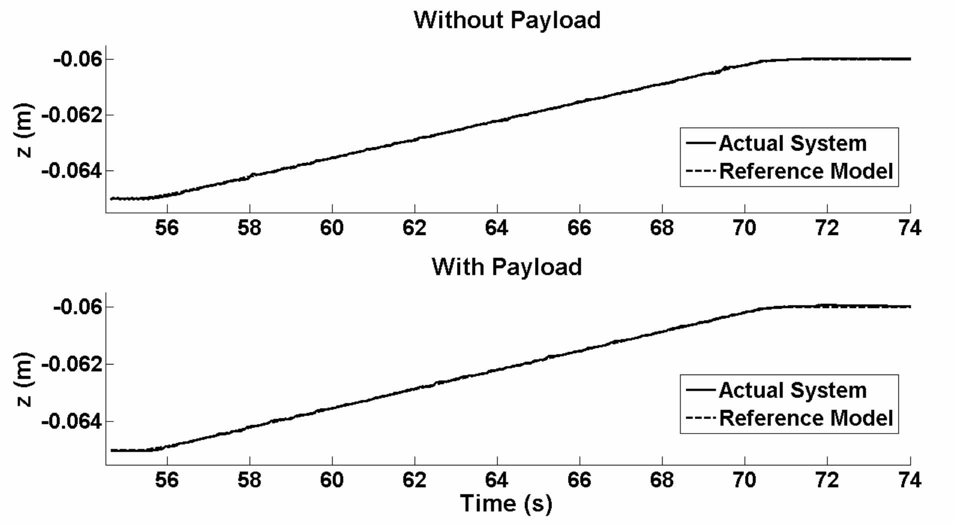

Figure 7-7: Ramp response of MRAFL controller after adaptation with and without a payload.

Table 7-1 compares the performance criteria of the proposed controllers when the payload is changed. The criteria listed in this table clearly show that the MRAFL controller's performance is slightly changed when the microrobot grabbed the payload.

While the rise time of the MRAFL controller in the presence of the payload is approximately eight times higher than the FL controller, the former has a faster settling behavior than the latter.

Although the settling time of the FL controller drastically changes with regard to the payload, the MRAFL's settling time did not show a considerable dependency to the payload. Moreover, the overshoot and under shoot of the MRAFL controller is poorly affected by the payload and is always less than 1.6%. This guarantees a smooth and accurate operation of the microrobot regardless of the payloads that it carries.

Table 7-1: Comparison of performance criteria for the proposed controller and adaptive controller.

Performance criteria	FL Control		MRAFL Control	
	With payload	Without	With payload	Without
$T_r(s)$	0.15	0.12	0.95	1
$T_s(s)$	2.4	1	1.3	1.36
P.M.O	55	30	1.6	0.6
P.M.U	70	50	1.2	0.6
RMS(mm)	0.0279	0.0097	0.0080	0.0057

In terms of the accuracy of positioning, the MRAFL showed a significant advantage over the FL controller in the presence of payload. Although the results presented in this table may not be optimal, they show the applicability of the proposed MRAFL strategy to tackle the weight variations and improve the performance of the system. In the next section, horizontal control of the object is addresses.

Chapter 8

Horizontal Position Control

8.1. Introduction

In this chapter, the horizontal position control of the levitated object will be addressed. All the horizontal positioning experiments conducted in this chapter were performed with the permanent magnet operating approximately 5mm above an aluminum block. This block was used as it was observed that the levitated object would start to vibrate and sway back and forth in the absence of the block.

It is believed that eddy currents produced in the aluminum block produce a damping effect in order to oppose the variations in the magnetic field. In [131] it is shown that the block does not significantly impact the dynamics of the vertical positioning system.

The three dimensional (3D) position control of the levitated object is performed based on two different control laws. While the first controller stabilizes the object in the vertical direction, the second controller adjusts the current ratios in the coils for the horizontal position control of the object.

In [93] Khamesee showed that if the total current sent to the coils is constant and the levitated object is in equilibrium, changing the ratio of the currents in the coils will affect the horizontal equilibrium point of that object without considerably affecting its vertical equilibrium characteristics. Figure 8-1 shows a schematic of the 3D position control system.

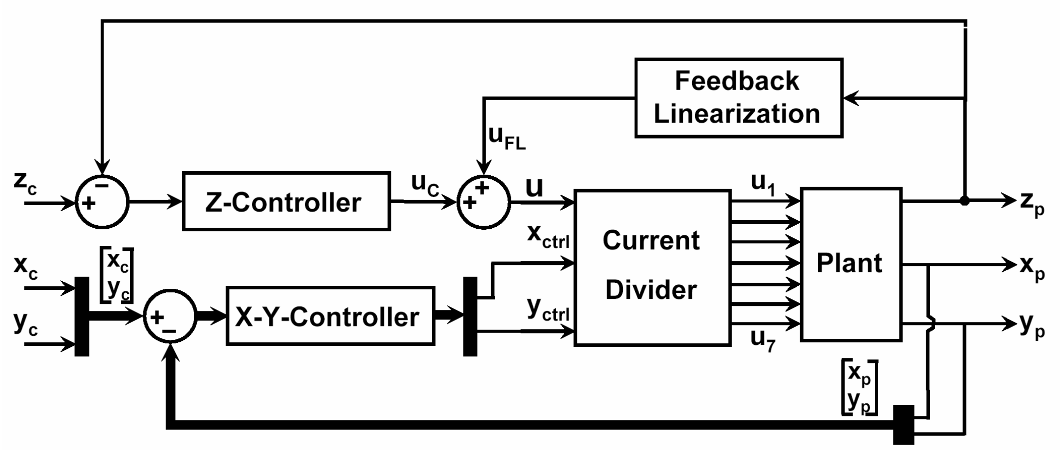

Figure 8-1: Schematic of the 3D position control system.

It is important to note that despite the unstable nature of the system in the vertical direction, the levitated object is stable in the x and y directions. Therefore, the controller design for the horizontal positioning of the object is a fairly simple task compared with the controller design for the vertical direction.

As seen in this figure, the horizontal position of the object is controlled through a feedback linearization signal u_{FL} added to signal u_C coming from the z-controller. In all the experimental results presented in this chapter, the z-controller uses a PID control law with the proportional, integrator and derivative gains of $K_p = 65$, $K_i = 100$ and $K_d = 6$.

The z-controller calculates the control signal u_C based on the vertical positioning error of the system. The total control signal u is calculated as the sum of the feedback linearization signal and the z-controller signal as:

$$u = u_{FL} + u_C \tag{8-1}$$

In the absence of any horizontal control, the calculated signal u in Eq. (8-1) will be directly sent to all the seven electromagnets in order to achieve the desired vertical position. Addition of horizontal control requires further manipulation of u after it has been calculated by the vertical position controller.

The x-y-controller will calculate two current ratio factors x_{ctrl} and y_{ctrl} based on the positioning error in the x and y directions.

The current divider block shown in Figure 8-1 is receiving the current ratio commands x_{ctrl} and y_{ctrl} and adjusts the currents in the electromagnets. Adjustment of the currents in the electromagnets is based of the desired direction of movement of the levitated object. In the next section the principle of current adjustment will be presented.

8.2. Principle of Current Adjustment

Figure 8-2 shows the layout of the electromagnets on the pole piece relative to the global coordinate frame. As a general rule, the levitated object tends to move towards the electromagnets which are fed with higher electrical currents.

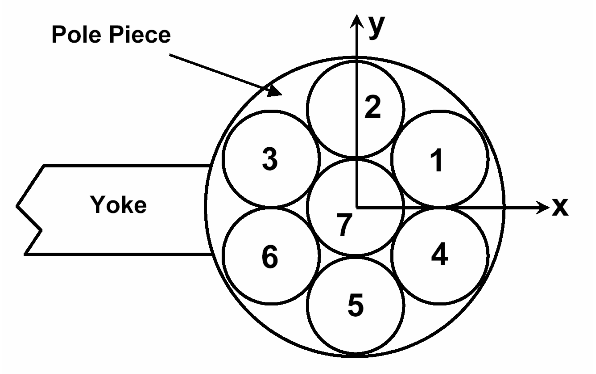

Figure 8-2: Layout of the pole piece electromagnets.

Based on this principle, Table 8-1 is suggesting a current adjustment scheme for producing the motion in a given direction.

Table 8-1: Current adjustment rules in the electromagnets for producing motion in a given direction.

Direction of Motion	**Increase current in electromagnets**	**Decrease current in electromagnets**
+x	1,4	3,6
−x	3,6	1,4
+y	1,2,3	4,5,6
−y	4,5,6	1,2,3

As stated in [93], the algorithm used to adjust the currents must ensure that the change in the currents is performed such that the sum of the currents sent to the coils remains constant and equal to u_{sum}. For the magnetic drive unit used in the experiments, the value of u_{sum} is calculated as:

$$u_{sum}=7u \tag{8-2}$$

where u is the vertical control signal calculated in Eq. (8-1). The current ratio algorithms governing the current divisions are selected as:

$$u_1 = u\left(1 + x_{ctrl}\right)\left(1 + y_{ctrl}\right) \tag{8-3}$$

$$u_3 = u\left(1 - x_{ctrl}\right)\left(1 + y_{ctrl}\right) \tag{8-4}$$

$$u_4 = u\left(1 + x_{ctrl}\right)\left(1 - y_{ctrl}\right) \tag{8-5}$$

$$u_6 = u\left(1 - x_{ctrl}\right)\left(1 - y_{ctrl}\right) \tag{8-6}$$

$$u_2 = \frac{\left(6u - u_1 - u_3 - u_4 - u_6\right)\left(1 + ny_{ctrl}\right)}{2} \tag{8-7}$$

$$u_5 = \frac{\left(6u - u_1 - u_3 - u_4 - u_6\right)\left(1 - ny_{ctrl}\right)}{2} \tag{8-8}$$

$$u_7 = u \tag{8-9}$$

where x_{ctrl} and y_{ctrl} are the current ratio factors and n is an arbitrary constant.

The value of n can be increased so that the currents in electromagnets 2 and 5 will change at a greater rate as y_{ctrl} is varied. The reason for using the arbitrary constant n is to compensate for the none-similar pattern of electromagnets arrangement with respect to the x and y directions.

In [131], Craig showed that for higher values of n it is possible to move the levitated object further for an equivalent y_{ctrl} signal. The tradeoff to this is that the output current to the electromagnet will saturate faster at higher values of n, producing more heat as the power is dissipated in the electromagnets. The range of n as stated in [131] varies between 1 and 1.5 depending on the vertical operating distance of the object from the pole piece. In the next section a PID controller is presented in order to adjust the current ratio factors x_{ctrl} and y_{ctrl}.

8.3. PID Control of the Horizontal Magnetic Levitation

As stated earlier in this chapter, horizontal control of the levitated object is a fairly simple task compared with the vertical control. As the levitated object always tends to move towards the maximum point of magnetic field, the levitation system in the horizontal direction is inherently stable.

Even an open loop controller can be used for the horizontal position control of the object. However, due to the modeling uncertainties and hysteresis effect, an open loop controller will introduce a steady state error in the positioning of the object.

In this section, a PID controller is utilized in an attempt to eliminate the steady state error and hysteresis effects. Using the PID control law, the current ratio factors $\mathrm{x}_{\mathrm{ctrl}}$ and $\mathrm{y}_{\mathrm{ctrl}}$ are calculated as:

$$\begin{bmatrix} x_{ctrl} \\ y_{ctrl} \end{bmatrix} = K_p^H \begin{bmatrix} x_c - x_p \\ y_c - y_p \end{bmatrix} + K_i^H \begin{bmatrix} \int_0^t \left(x_c - x_p \right) d\tau \\ \int_0^t \left(y_c - y_p \right) d\tau \end{bmatrix} + K_d^H \begin{bmatrix} \dot{x}_c - \dot{x}_p \\ \dot{y}_c - \dot{y}_p \end{bmatrix} \tag{8-10}$$

where K_p^H, K_i^H and K_d^H are the proportional, integral and derivative gains respectively. For all the experiments presented in this chapter, the horizontal PID control gains were set as:

$$K_p^H = 200 \quad , \quad K_i^H = 400 \quad , \quad K_d^H = 0.001 \tag{8-11}$$

Also, the value of n in equations (8-7) and (8-8) was set as $\mathrm{n}=1.25$ and all the horizontal movements were performed at $z = -0.067\left(\mathrm{m}\right)$ with the levitating permanent magnet operating approximately $5\left(\mathrm{mm}\right)$ above an aluminum block. In the next sections, the step response and trajectory tracing of the proposed PID controller are discussed.

8.4. Step and Ramp Responses

In this section, the position control formula in equation (8-10) is implemented to investigate the step and ramp responses of the system in the horizontal direction.

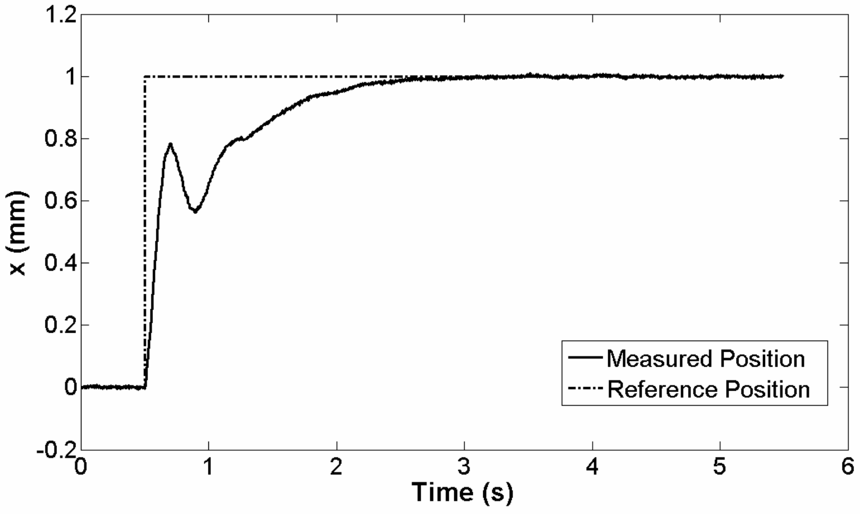

Figure 8-3: Step response of the levitation system for a positive step command in the x direction.

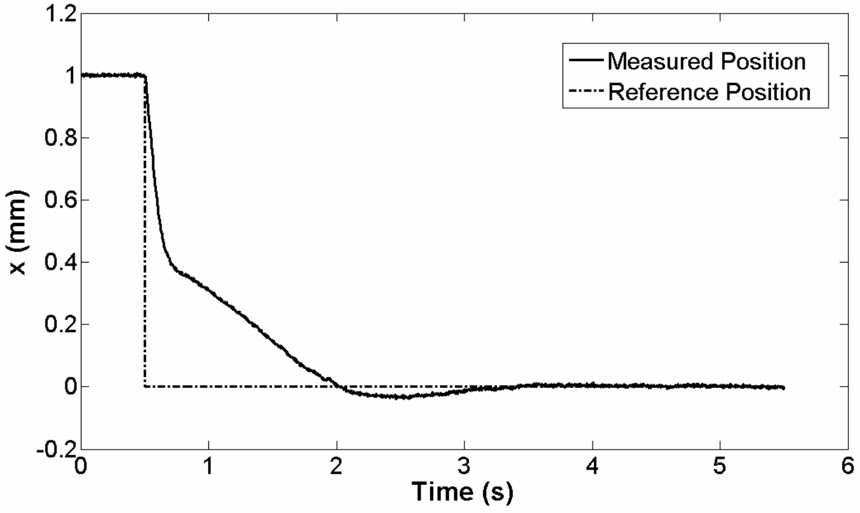

Figure 8-4: Step response of the levitation system for a negative step command in the x direction.

Figure 8-3 and Figure 8-4 show the step response of the system for positive and negative step commands along the x axis respectively. As is seen in these figures, the behavior of the system in following a positive step command is different from the behavior of the system in following a negative step command. This difference is due to the non-symmetrical geometry of the magnetic unit with respect to the y direction as shown in Figure 8-2.

Another issue to be addressed is the sudden decrease in the position of the levitated object approximately at time t=1(s) in Figure 8-3. It is believed that this behavior is caused by the eddy current effects produced in the aluminum block.

Elbunken [95] has shown that the eddy current effects of the aluminum block are generated in a way to oppose the movements of the levitated object. When a step command is issued, the aluminum block will start to generate a magnetic field to oppose the field change mainly due to the movement of the levitated object.

Although the sources of the eddy currents are the magnetic field of the magnetic drive unit and the local magnetic field of the levitated permanent magnet, due to the small distance between the aluminum block and the permanent magnet, the main source of the eddy currents in the block is the field of the permanent magnet.

The field of the resultant eddy currents will impose a magnetic force to the permanent magnet in an opposite direction of its motion. Since the dominant source of the eddy currents is the highly concentrated magnetic field of the permanent magnet and the source of the horizontal movement is the fairly concentrated field of the magnetic drive unit, it is possible that at some instances, the eddy current forces get bigger in magnitude than the horizontal force and pull the object back. This is believed to be the reason of the behavior seen in Figure 8-3.

Comparing Figure 8-3 and Figure 8-4 it is seen that the performance of the system for the positive and negative step commands is different. The reason is the existence of the yoke in the negative side of the x axis. As the yoke is made of a soft magnetic iron, the yoke side of the system has a higher capacity for magnetic field. In better words, the system can achieve higher magnetic field intensities and gradients in the yoke side. This is the reason why the eddy current pull back effect is not seen in Figure 8-4.

The situation is different in the y direction. Figure 8-5 and Figure 8-6 show the performance of the system in the y direction. Due to the symmetricity of the magnetic drive unit with respect to the x axis, the responses of the system to the positive and negative step commands are identical.

Moreover, since the yoke profile is not projected over the y direction, there is an eddy current pull back effect seen in the response of the levitated object.

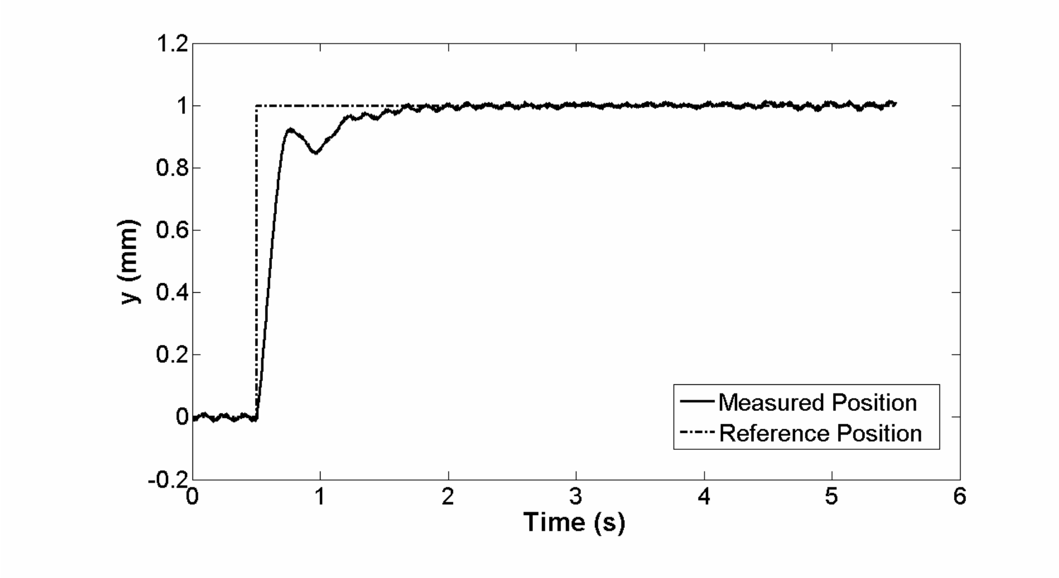

Figure 8-5: Step response of the levitation system for a positive step command in the y direction.

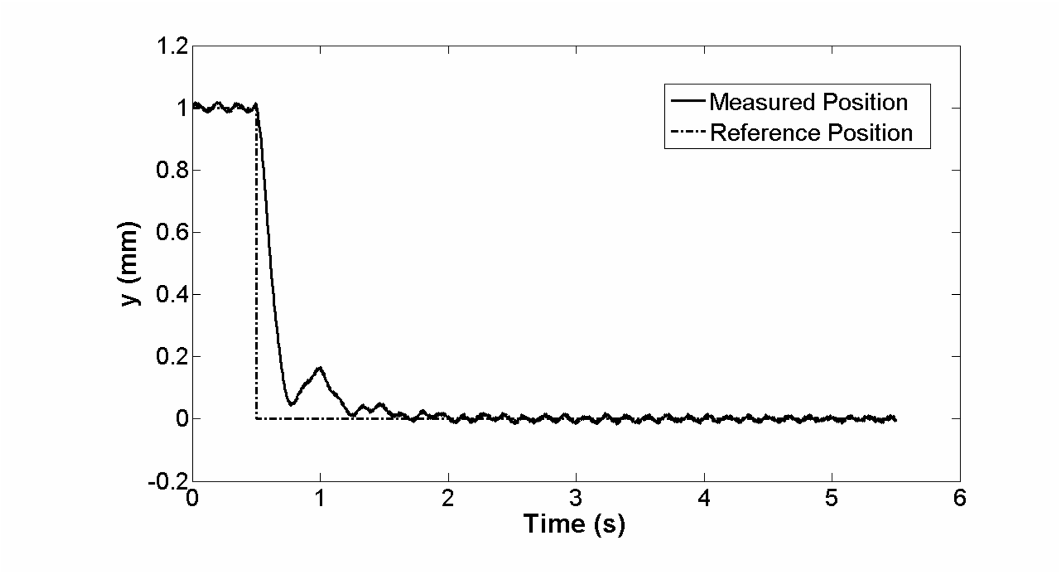

Figure 8-6: Step response of the levitation system for a negative step command in the y direction.

One issue to be addressed is the overall difference in the responses of the system along the x and y axes. As the electromagnets distribution is not similar in the x and y directions, the responses of the system will be a bit different along each axis.

As is seen in Figure 8-2, there are 4 electromagnets associated with the movement of the object in the x direction compared to 6 electromagnets related to the y direction. Therefore using the same PID gains for both directions, it was seen that the response of the levitated object is more sensitive to the commands along the y axis.

This higher sensitivity is increasing the speed of the controller in the y direction. However, it also increases the sensitivity of the system to the noise.

The ramp responses of the system are shown in Figure 8-9 and Figure 8-10. As seen in these figures, since the system has a faster response along the y axis, the ramp steady state error in the y direction is less than the x direction. In contrast, the levitated object demonstrated more sensitivity to the noise in the y direction and maintained a sustained vibration along this direction.

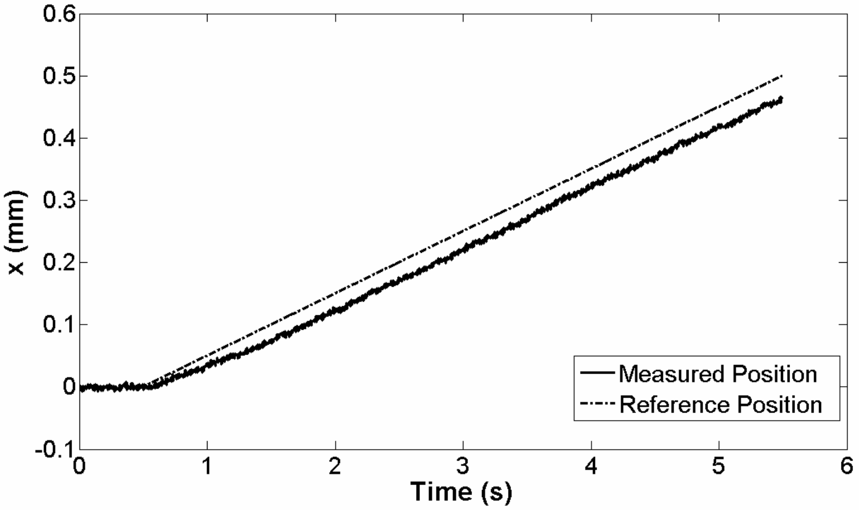

Figure 8-7: Ramp response of the levitation system in the x direction.

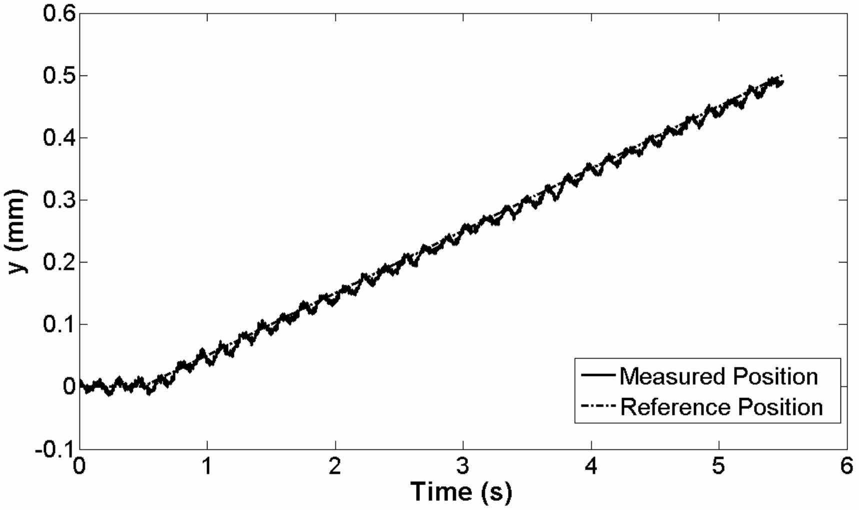

Figure 8-8: Ramp response of the levitation system in the y direction.

Table 8-2 compares the performance of the controller in the x and y directions. The comparison is performed in terms of settling time, percent of overshoot and root mean squared (RMS) error. As it is seen from the settling time, the controller in the y direction is up to 50% faster than the controller in the x direction. In contrast, the accuracy of the positioning system in the x direction is twice the accuracy in the y direction.

Table 8-2: Comparison of the controller's performance in the x and y directions.

Direction	**x**	**y**
Settling time (s)	1.51	0.98
Overshoot (%)	3.5	0
RMS Error (μm)	2.89	7.15

Both systems are highly damped due to the operation above the aluminum block and have a negligible percent of overshoot. However, for a negative step command along the x axis, an overshoot of 3.5% was observed due to the yoke effect.

A detailed discussion on the modeling and controller design for the horizontal positioning system is presented in the work of David Craig [131]. In the next section, the trajectory tracking problem in the horizontal direction is addressed.

8.5. Trajectory tracking in the horizontal direction

In order to perform useful operations, the levitation system needs to be capable of navigating along complex paths and trajectories. This section will discuss the performance of the microrobot as it traces out two different trajectories in the horizontal plane at a constant height z.

The first trajectory investigated was a circle in the horizontal plane with radius of 1(mm) and its centre on the z axis. Figure 8-9 and Figure 8-10 illustrate the motion of the levitated object in the x and y directions in following the circular trajectory.

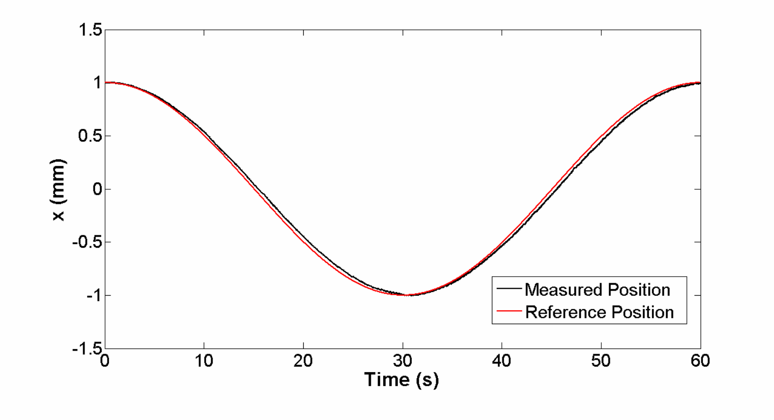

Figure 8-9: Motion of the magnet in the x direction in following a circular trajectory.

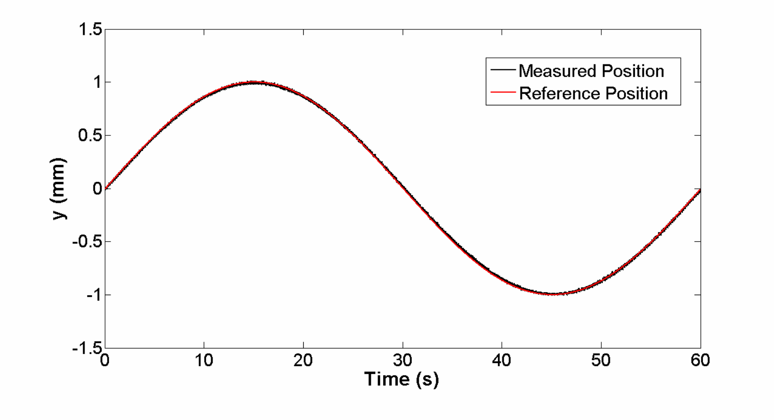

Figure 8-10: Motion of the magnet in the y direction in following a circular trajectory.

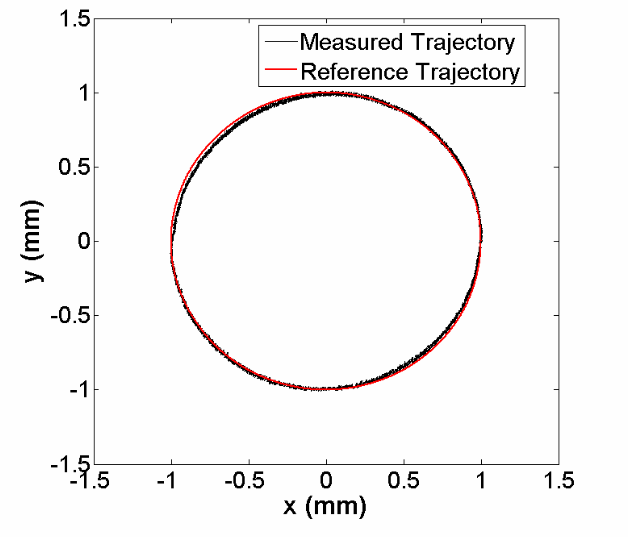

Figure 8-11: 1 mm radius circle trajectory traced with a rotational velocity of 0.1 rad/s.

The trajectory is generated such that the full circle is completed in 1 minute which yields to an approximate circular speed of $0.1(\mathrm{rad/s})$. As stated in the previous section, the horizontal control system is highly damped and therefore, high speed trajectories, will result in an increased trajectory tracking error. The total circular trajectory is illustrated in Figure 8-11.

The second trajectory was a spiral with final radius of 1(mm) and the total rotation angle of 4π radians. Figure 8-12 and Figure 8-13 illustrate the motion of the levitated object in the x and y directions in following the spiral trajectory. The total spiral trajectory is illustrated in Figure 8-14.

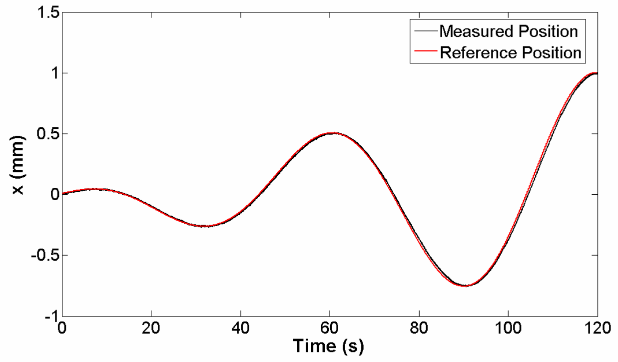

Figure 8-12: Motion of the magnet in the x direction in following a spiral trajectory.

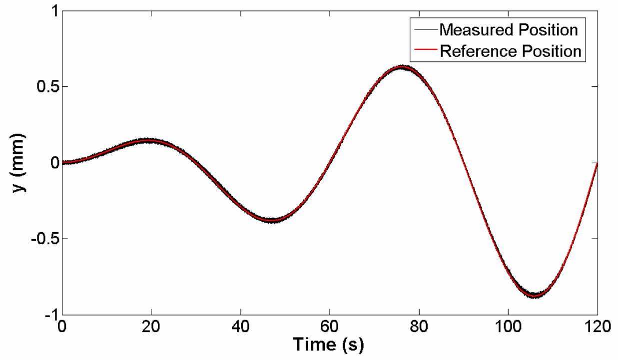

Figure 8-13: Motion of the magnet in the y direction in following a spiral trajectory.

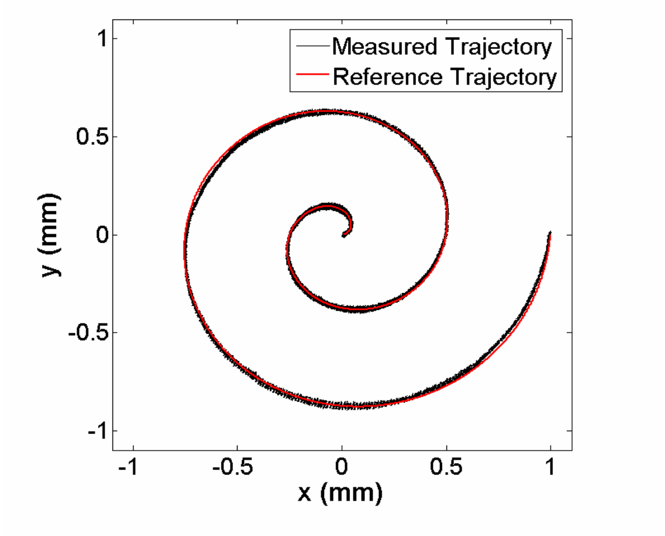

Figure 8-14: 1 mm radius spiral trajectory traced with a rotational velocity of 0.1 rad/s.

The spiral path was traced in the total time of 120(s) yielding an approximate rotational velocity of 0.1 rad/s.

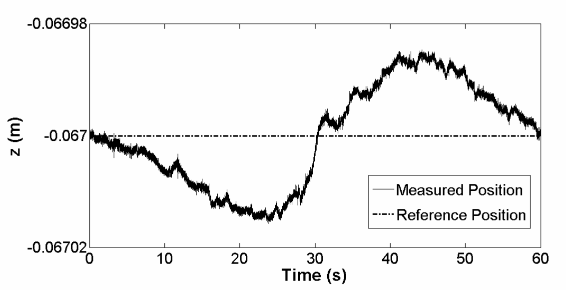

Figure 8-15: Vertical position of the magnet in the circular trajectory tracking.

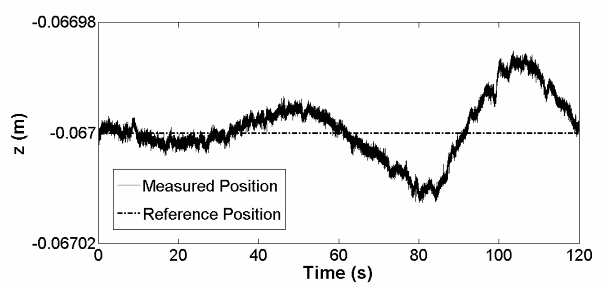

Figure 8-16: Vertical position of the magnet in the spiral trajectory pracking.

During the course of motion, the vertical position command was kept constant and equal to -0.067(m). Figure 8-15 and Figure 8-16 show the measured vertical position of the magnet during the trajectory tracking tasks. It is seen that although the change in the vertical position is very small, less than 20(μm), but there is a similarity between the vertical position of the object and the movement of the object in the horizontal direction.

This correlation between the directions of the motion is due to the fact that the magnetic levitation system has a single pole piece. In better words, the states of the system are not completely separable. However, due to the very weak dependency between the states of the system, the control design problem can be tackled in separate steps for each direction.

The total positioning error of the levitation system is obtained as:

$$e_{tot} = \sqrt{e_x^2 + e_y^2 + e_z^2} \tag{8-12}$$

Where e_x, e_y and e_z are the error values in the x, y and z directions.

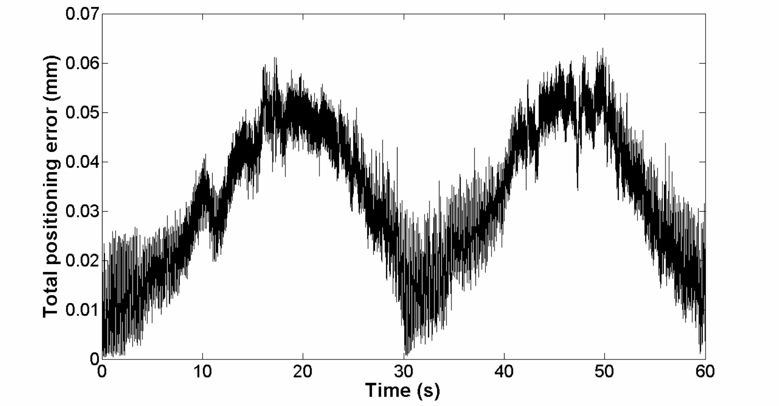

Figure 8-17: Total positioning error of the control system for the circular trajectory.

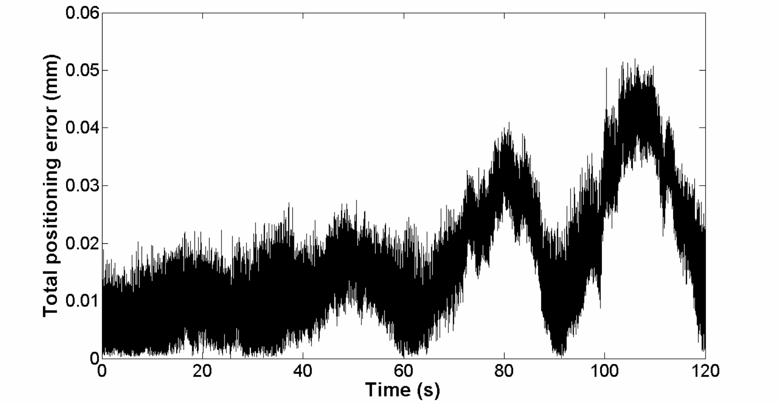

Figure 8-18: Total positioning error of the control system for the spiral trajectory.

Figure 8-17 and Figure 8-18 show the total positioning error in tracking the circular and spiral trajectories. As is seen in these figures, the maximum positioning error of the system is 60(μm). It is also seen that the value of the total error has a direct relationship with the position of the object in the y direction. For example, according to Figure 8-17, the maximum total error in the circular trajectory tracking happens approximately at times $t = 15(s)$ and $t = 45(s)$. As illustrated in Figure 8-10, at these times the object is levitated at the maximum y distance from the origin.

The reason for the relationship between the y and the total error is based on the fact that the horizontal movement of the levitated object in the y direction depends on six electromagnets i.e. 1, 2, 3, 4, 5, and 6. However, in the x direction there are only four electromagnets 1, 3, 4, and 6 that correspond to the displacement along this direction. Therefore, the movement of the object in the y direction affects six electromagnets out of seven electromagnets and dominates the pattern of the total positioning error.

In order to achieve higher positioning accuracies, an interconnecting control state can be added to equations of the system. This additional state should be defined in the form of a mathematical relationship based on the correlation between the behavior of the system in the horizontal direction, Figure 8-11 and Figure 8-14, and its performance in the vertical direction, Figure 8-15 and Figure 8-16. In this case, the 3D positioning ability of the system in tracking of the three dimensional non-planar trajectories will be highly improved.

Although this chapter showed the possibility of an accurate horizontal position control in the absence of a mathematical control model, in some cases it is highly desired to have a mathematical model of the horizontal behavior of the system. In the next chapter, a method is proposed for the development of a model for horizontal control.

Chapter 9

Pivot Point Method

9.1. Introduction

This chapter presents a mathematical model for predicting the position of the maximum point of magnetic field in the magnetic levitation device. Conventional field modeling methods generally involve numerical solution of differential equations of the field. This will take enormous computational time and makes these methods inefficient for real-time applications.

In this chapter, a fast mathematical model for the prediction of magnetic field is proposed and verified experimentally. The model is developed based on the geometry of the magnetic drive unit and its magnetization pattern. The accuracy of the model is verified experimentally. In the next section, the magnetization of the pole piece is addressed as the base of the pivot point method.

9.2. Pole Piece Magnetization

When the pole piece is placed in an externally applied magnetic field, the total magnetic field at an arbitrary position $\mathbf{r}$ can be written in the form of:

$$\mathbf{H}(\mathbf{r}) = \mathbf{H}_{ext}(\mathbf{r}) + \mathbf{H}_d(\mathbf{r}) \tag{9-1}$$

where $\mathbf{H}_{ext}$ and $\mathbf{H}_d$ are the external magnetic field and pole piece demagnetizing field respectively and are expressed in $(\mathrm{A/m})$.

The sources of $\mathbf{H}_d$ are volume divergences of magnetization vector $\mathbf{M}(\mathrm{A/m})$ and normal components ("surface magnetic charges") of $\mathbf{M}$ on the surface of the pole piece. The relationship between the external field $\mathbf{H}_{ext}$, magnetization vector $\mathbf{M}$ and demagnetizing field $\mathbf{H}_d$ is expressed as:

$$\mathbf{M} = \chi_m \mathbf{H} = \chi_m \left(\mathbf{H}_{ext} + \mathbf{H}_d \right) \tag{9-2}$$

where χ_m is the magnetic susceptibility of the pole piece.

In general, calculation of the magnetization profile in the pole piece is a challenging task and requires finite element solution. In order to get a physical insight of the pole piece magnetization, it is worthwhile to apply the magnetic flux continuity on the boundaries of the pole piece.

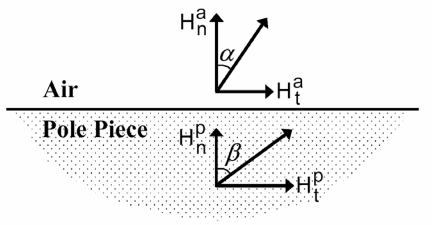

Figure 9-1: The continuity conditions at the boundary of the pole piece.

Figure 9-1 illustrates a graphical representation of the relations between the components of $\mathbf{H}$ at an interface between the air and pole piece. At this boundary, the normal flux density $\mu \mathbf{H}_n$ is continuous [109].

Since there is no surface current density associated with the pole piece, the tangential components of the magnetic flux density are also continuous [109]. Angles α and β in the figure are obtained as:

$$\tan\alpha = \frac{H_t^{\mathrm{a}}}{H_n^{\mathrm{a}}} \quad , \quad \tan\beta = \frac{H_t^p}{H_n^p} \tag{9-3}$$

The magnetic flux continuity condition in terms of the pole piece relative permeability μ_r yields that:

$$\tan\beta = \mu_r \tan\alpha \tag{9-4}$$

From Eq. (9-2) it is inferred that the magnetization vector and the total magnetic field vector are parallel. Therefore, Eq. (9-4) can be used for a qualitative analysis of the pole piece magnetization based on the external field inclination angle at the boundaries of the pole piece. Figure 9-2 demonstrates the relationship between the α and β angles for different pole piece permeabilities.

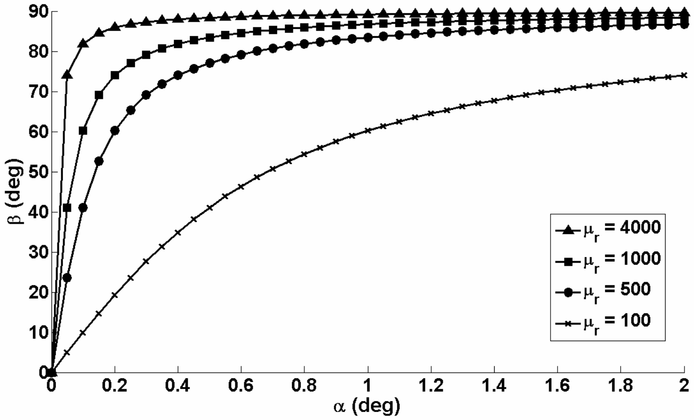

Figure 9-2: The inclination angle of magnetic field vector at the boundary of the pole piece.

Since the pole piece is made of soft magnetic iron, its relative permeability is more than 4000.

Assuming a relative permeability of $\mu_r = 4000$ for the pole piece, it is seen in Figure 9-2 that angle β tends to 90° degrees for very small values of inclination angle α. In fact, the pole piece extremely tends to align the magnetic field, hence the magnetization vector, parallel to its surface. Therefore, the penetration of the external field into the pole piece is only possible if the external field is perpendicular to the surface of the pole piece or has a very small deviation from the perpendicular direction.

Since the sources of the external magnetic field are the coils assembled on the top surface of the pole piece, the perpendicular magnetic field only exists in a very small area below the center of each coil. Therefore, the pole piece magnetization in the perpendicular direction will be concentrated below the center of electromagnets. This conclusion is consistent with the finite element results.

Figure 9-3 shows an axisymmetric view of an electromagnet installed on the top surface of a disk shaped pole piece.

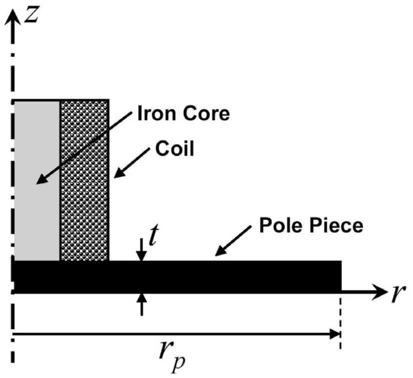

Figure 9-3: Geometry of the studied pole piece.

Finite element results showed that magnetization of the pole piece in the perpendicular direction is highly concentrated below the center of the coil. Also, it was seen that in general, the pole piece magnetization is highly correlated with the distribution of the externally applied magnetic field. Several pole piece simulations with different radius to thickness ratios revealed that increasing the radius to thickness ratio will increase the correlation between the pole piece magnetization and the external field.

A numerical simulation was performed for a pole piece with radius of $r_p = 0.066\left(\text{m}\right)$, thickness of $t = 0.00635\left(\text{m}\right)$, and relative permeability of $\mu = 4000$. The source of the external field is a solenoid with length of $l = 0.04\left(\text{m}\right)$, inside radius of $r_{in} = 0.01\left(\text{m}\right)$, outside radius of $r_{out} = 0.02\left(\text{m}\right)$ and $N_S = 840$ turns of wire.

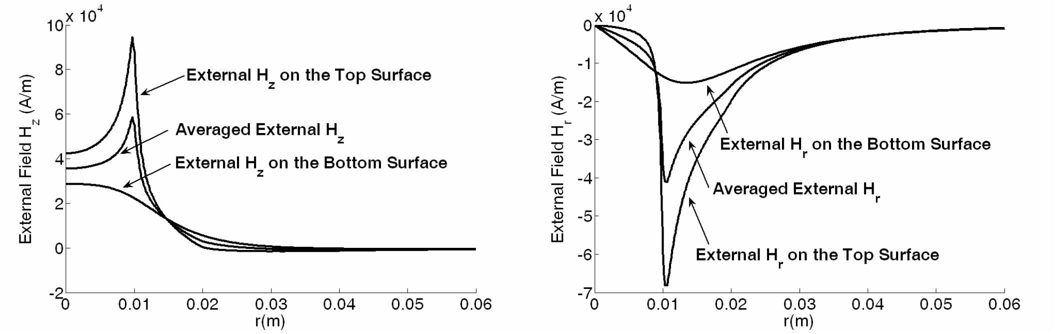

a) Normal field. **b) Radial field.**

Figure 9-4: Externally applied magnetic field.

Figure 9-4 illustrates the normal and radial components of the externally applied magnetic field on the top and bottom surfaces of the pole piece. As it can be seen in this figure both of the normal and radial fields are mainly concentrated at areas below the centre of the electromagnet.

As Figure 9-4(b) shows, the radial component of the external field within the range $r \in [0, 0.01](\mathrm{m})$ is negligible compared with the normal field. Hence the external field in this region is perpendicular to the pole piece and generates a considerable normal magnetization as shown in Figure 9-5(a). Similarly, the radial magnetization follows the same pattern as radial external field, Figure 9-5(b).

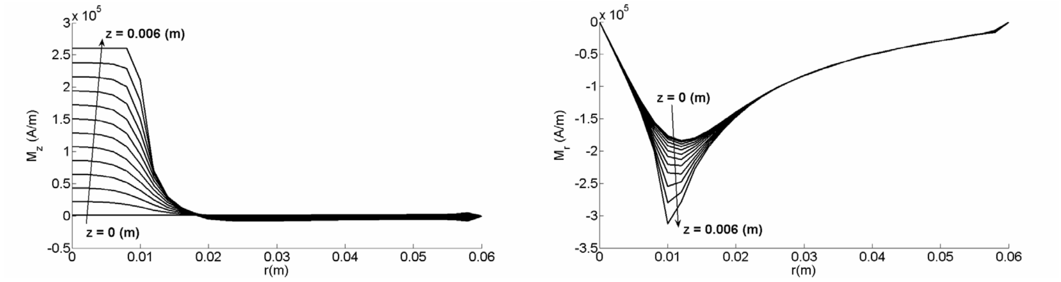

a) Normal magnetization. **b) Radial magnetization.**

Figure 9-5: Magnetization of the pole piece.

As mentioned earlier, the source of the demagnetizing field is pole piece magnetization. Thus, by superposing the effects of normal and radial magnetizations with the external field, the total field can be calculated. As inferred from Figure 9-5(a) and Figure 9-5(b), the maximum pole piece magnetization in both normal and radial directions is concentrated within the range $r \in [0, 0.02](\mathrm{m})$ which is the same size as the coil's outer diameter.

Therefore, as a simplifying assumption, the magnetization profile of the pole piece outside this range can be neglected with no considerable effect on the demagnetizing field. Figure 9-6 shows the normal field generated by the simplified pole piece magnetized in the radial direction. As illustrated in Figure 9-6(b), the radially magnetized pole piece will generate the maximum effect below the pole piece center.

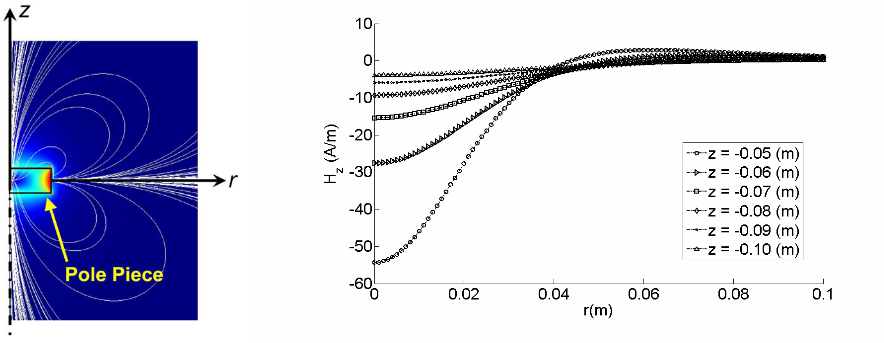

a) Magnetic field streamlines. **b) Normal magnetic field.**

Figure 9-6: Normal field of a radially magnetized disk.

The same pattern can be seen for a normally magnetized disk as shown in Figure 9-7. Comparing the magnetic field generated by the radially and normally magnetized pole piece reveals that the effect of normal magnetization on the normal demagnetizing field distribution is approximately five times higher than the effect of radial magnetization.

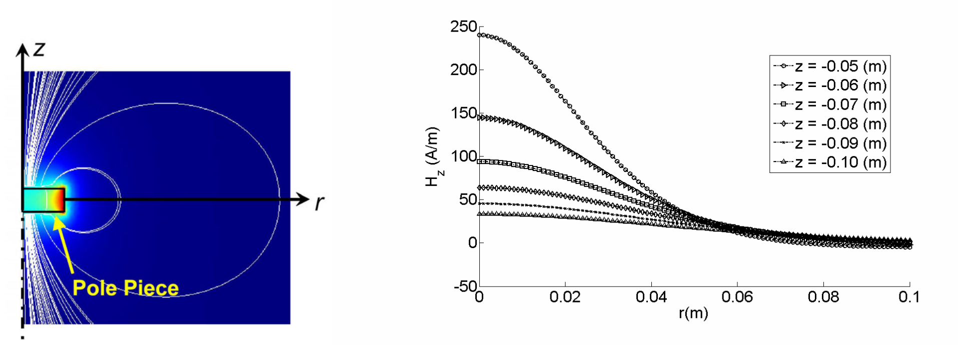

a) Magnetic field streamlines. **b) Normal magnetic field.**

Figure 9-7: Normal field of a normally magnetized disk.

This is due to the similarity in the direction of the desired field and the direction of the normal magnetization. Moreover, it is shown that both radial and normal magnetization profiles result in similar demagnetizing field distribution patterns.

By considering the Green function as:

$$G(\mathbf{r},\mathbf{r}') = \nabla \frac{1}{|\mathbf{r}-\mathbf{r}'|} = -\frac{\mathbf{r}-\mathbf{r}'}{\|\mathbf{r}-\mathbf{r}'\|^3} \tag{9-5}$$

it can be shown that the magnetic field distributions in the z direction can be represented by a series of green functions. In Cartesian coordinate, the position vectors $\mathbf{r}$ and $\mathbf{r}'$ are expressed as (x, y, z) and (x', y', z') respectively. Thus, the Green function is written as [109]:

$$\nabla \frac{1}{|\mathbf{r}-\mathbf{r}'|} = -\frac{(x-x')\hat{\mathbf{i}}+(y-y')\hat{\mathbf{j}}+(z-z')\hat{\mathbf{k}}}{\left[\sqrt{(x-x')^2+(y-y')^2+(z-z')^2}\right]^3} \tag{9-6}$$

Since all the composing components of the magnetic field including the external field, the demagnetizing field due to radial magnetization of the pole piece, and the demagnetizing field due to normal magnetization of the pole piece follow the same pattern as the Green function presented in Eq. (9-6), this function can be used as a core element in mathematical model of the total magnetic field. In this model, each green function has a pivot point represented with vector $\mathbf{r}'$.

The pivot point is defined as the three dimensional coordinates of the point at which the center of the electromagnet is attached to the pole piece. In the next section, the pivot point model will be introduced as a fast and reliable estimator for the location of $\mathbf{H}_{\max}$.

9.3. Introducing the Pivot Point Method (PPM)

In the PPM, each electromagnet is assigned with three identification properties i.e. the pivot point coordinate $\mathbf{r}_p$, the geometry factor κ and the electrical current $I(\mathrm{A})$ supplied to the electromagnet.

For a magnetic system like the one shown in Figure 9-8, the magnetic sum function (MSF) is defined as:

$$\mathrm{MSF}(x, y, z) = \sum_{j=1}^{n} \frac{\kappa(z-z_j)I_j}{\sqrt{(x-x_j)^2+(y-y_j)^2+\kappa^2(z-z_j)^2}^3} \tag{9-7}$$

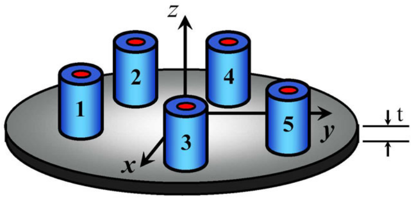

Figure 9-8: Magnetic stator system.

where, $\mathbf{r}=(x,y,z)$ is an arbitrary point in the space, $\mathbf{r}_p^j=(x_j,y_j,z_j)$ is the pivot point corresponding to the j^{th} electromagnet, I_j is the current in the j^{th} electromagnet, and κ is the geometry factor of the j^{th} electromagnet. The geometry factor κ is an experimental value that is a function of system's geometry. In practice, the geometry factor is obtained experimentally.

It can be shown that if the geometry factor is found properly, the (x,y) coordinates of the $\mathbf{H}_{\max}$ on a horizontal plane with distance h below the pole piece, can be accurately estimated by finding the pair (x_m,y_m) that maximizes $\mathrm{MSF}(x,y,h)$ in Eq. (9-7). This approach is called the pivot point method and is proposed for the first time in this thesis.

Decreasing the radius of the electromagnets will increase the accuracy of PPM. However, for electromagnets with bigger diameters, defining multiple pivot points for each electromagnet will significantly improve the PPM accuracy. In this case the pivot points have to be distributed over the surface at which the electromagnet is attached to the pole piece.

In terms of calculation speed, PPM is faster than the finite element method, as the finite element method requires the formation and solution of a large set of simultaneous equations so as to calculate the maximum point of magnetic field. In contrast, the PPM has to solve a single pre-formed equation in order to find the maximizing pair (x_m,y_m) for the MSF. This will significantly reduce the calculation time of the PPM as it eliminates the step in which the equations are formed and also reduces the number of equations to one. This advantage will provide the potential to utilize the PPM in real-time control applications for magnetic levitation systems. In the next section, an experiment with the magnetic levitation device is presented to verify the practical performance of the pivot point method.

9.4. Experimental Verification of the Pivot Point Method

The pivot point method was verified in an experiment with the magnetic levitation device.

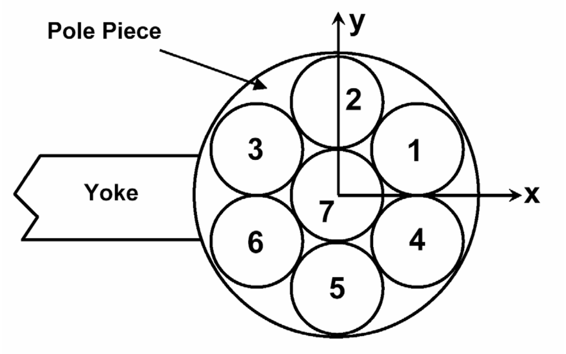

Figure 9-9: Layout of the pole piece and electromagnets.

The layout of the pole piece and the electromagnets is demonstrated in Figure 9-9. The verification experiment was performed along the y direction as the system is symmetric along this axis. The current ratio in the electromagnets is set as:

$$\frac{u_1}{u_4} = \frac{u_2}{u_5} = \frac{u_3}{u_6} = \frac{1+R}{1-R} \tag{9-8}$$

where R is called the current ratio factor. The current in electromagnet 7 is set as:

$$u_7 = \frac{u_1 + u_4}{2} \tag{9-9}$$

It is important to note that due to this current distribution, the position of the maximum point of magnetic field will move along the y axis and its x coordinate will be equal to zero.

Table 9-1: Numerical pivot point properties used in Eq. (9-7).

Electromagnet Index j	x_j **(m)**	y_j **(m)**	z_j **(m)**
1	0.0381	0.022	-0.0066
2	0	0.044	-0.0066
3	-0.0381	0.022	-0.0066
4	0.0381	-0.022	-0.0066
5	0	-0.044	-0.0066
6	-0.0381	-0.022	-0.0066
7	0	0	-0.0066

The first step in using the pivot point method is determining the number and locations of the pivot points. As there are seven operating electromagnets in the magnetic drive unit, the number of pivot points is seven. The location of each pivot point is the location at which its corresponding electromagnet is attached to the pole piece. Table 9-1 provides the numerical pivot point properties used for the experiment.

The second step is the calibration. In the calibration process a geometry factor k will be found for the pivot point formula in Eq. (9-7). A closed loop control method was used to stabilize the vertical position of the levitated object at z=0.055(m) i.e. 55(mm) below the bottom surface of the pole piece. Meanwhile, the current ratio factor R was manually changed to specific values and the shift in the position of the levitated object was recorded. As it was discussed in the previous chapters, since the levitated object will be stabilized at the maximum point of the magnetic field, measuring the steady state position of the levitated object will result in an accurate determination of the maximum point of magnetic field in the horizontal plane of levitation.

The process of manually changing the R and recording the shift in the position of the levitated object results in a set of data points that can be used in the calibration of the pivot point formula. Figure 9-10 shows the experimental data used in the calibration of the pivot point method.

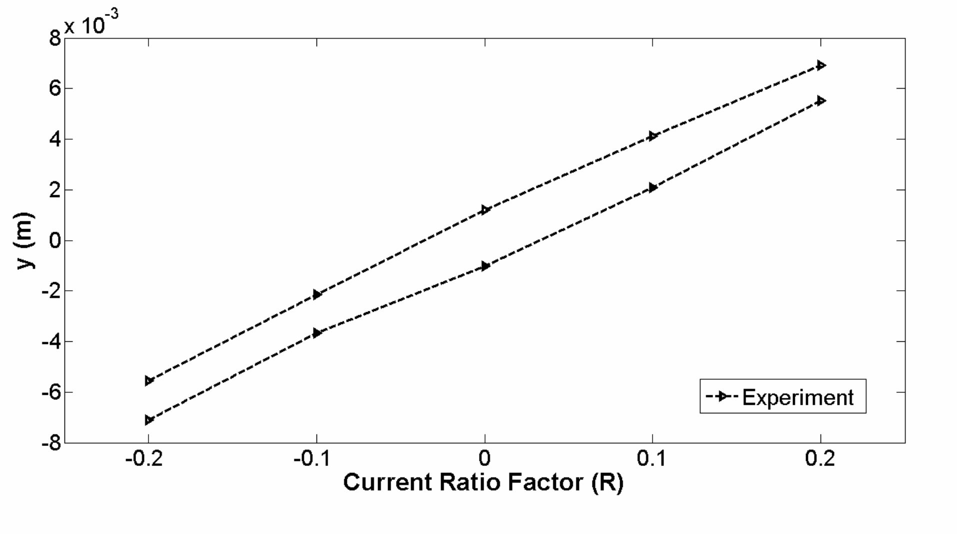

Figure 9-10: Experimental calibration data.

As seen in this figure, the levitation system will result in different maximum points of magnetic field for a fixed current ratio factor R. This phenomenon is a result of hysteresis effect in the magnetic levitation system and has been addressed in [131].

As a consequence of hysteresis in the system, the levitation device showed a slight dependency on the direction of the change in the current ratio factor. For a gradual current ratio factor change from -0.2 to 0.2, the data sets on the lower line of Figure 9-10 was recorded where as when R was gradually changed from 0.2 to -0.2, the data sets on the upper line was recorded.

In order to find the best geometry factor for the system, a one dimensional optimization on the pivot point method was performed. The function to be minimized in the optimization is called the error function and is defined as:

$$E_f = \sum_{i=1}^{N} \left[\left(x_m^i - x_i \right)^2 + \left(y_m^i - y_i \right)^2 \right] \tag{9-10}$$

where N is the number of data points, y_i is the calibration point corresponding to the case at which R is set as current ratio factor R_i, and y_m^i is the y location of the maximum point of magnetic field found by the pivot point method.

The error function was found for a number of geometry factors k ranging from 0.1 to 5, using the experimental data points of Figure 9-10.

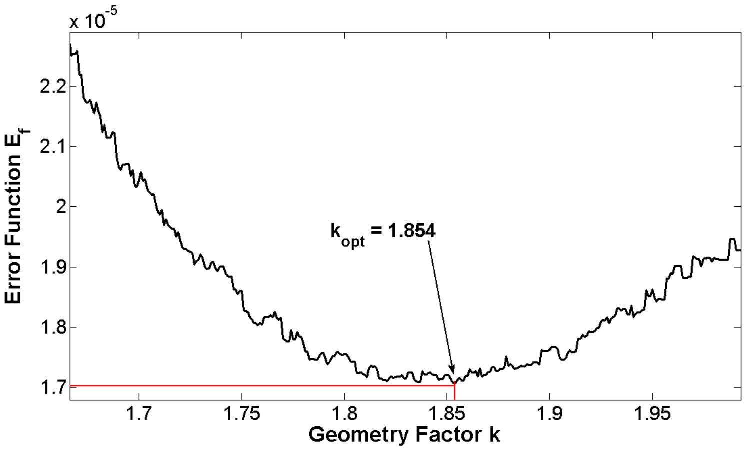

Figure 9-11: Determination of the optimum geometry factor.

Figure 9-11 shows the relationship between the error function E_f and the geometry factor k for the calibration data shown in Figure 9-10. As is seen in this figure, the choice of $k = 1.854$ will result in the minimum estimation error with the pivot point method.

For the verification of the pivot point method, the maximum point of the magnetic field was measured for different current ratio factors and the results where compared with the estimation results of pivot point method.

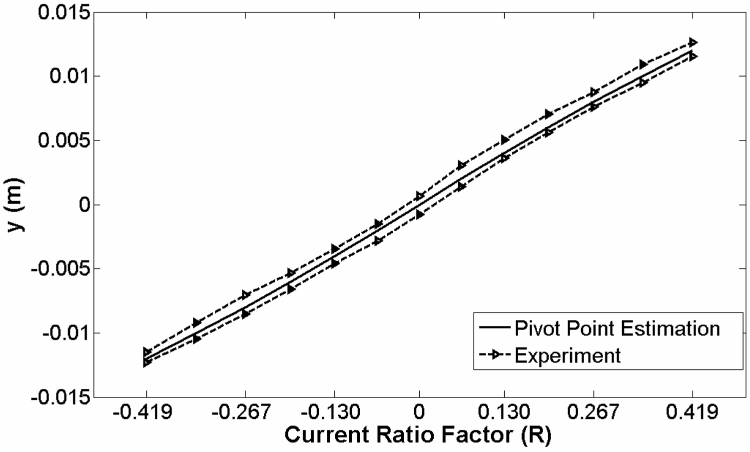

Figure 9-12: Experimental verification of pivot point method.

Figure 9-12 illustrates the comparison between the open loop shift in the location of the maximum point of the magnetic field and the pivot point estimation. As stated earlier, due to the hysteresis effects, in practice, multiple points were recorded for a particular ratio factor depending on the direction of change in the R.

For the experimental verification presented in this figure, the levitated object moves within the approximate range of -12(mm) to +12(mm) along the y axis. The maximum estimation error of PPM within this range was calculated as 1.06(mm) i.e. 8.8% with respect to traveling stroke of 12(mm).

Although the accuracy of the pivot point method at this stage is not optimal, it is capable of predicting the location of the maximum point of magnetic field with less than 10% of error. A better accuracy can be achieved through defining more pivot points for each electromagnet.

One of the practical applications of pivot point method can be open loop control of magnetic levitation system. While the PPM can predict the location of the maximum point of magnetic field for a given current ratio factor R, the inverse pivot point function can be used to calculate R for a desired shift in the position of the maximum point of magnetic field.

Although control is out of the scope of this chapter, in the next section utilization of the pivot point method in horizontal position control of the magnetic levitated object is addressed.

9.5. Magnetic Levitation Experiment

Presence of a mathematical model to predict the location of $\mathbf{H}_{\max}$ is an important factor in horizontal position control of the magnetically levitated object. Figure 9-13 illustrates the schematic of the closed loop control system used for position regulation of the levitated object. The input commands to the control loop contain the desired z location and y location of the levitated object.

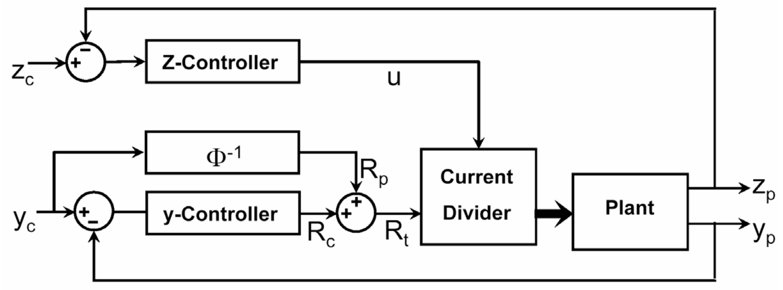

Figure 9-13: Schematic of the closed loop control system.

The z-controller is responsible for adjusting the vertical position of the levitated object through the calculation of un-weighted current command u. The y-controller is adjusting the position of the levitated object in the y direction through the calculation of appropriate current ratio factor R_c.

The Φ^{-1} block in Figure 9-13 represents the inverse of the pivot point formula and is used to calculate the appropriate current ratio factor R_p for a desired horizontal command signal $\mathrm{y_c}$. For this experiment, the Φ^{-1} function is a third order polynomial calculated through numerical curve fitting on the results of the pivot point method. The total current ratio factor, i.e. R_t, is calculated as the sum of the y-controller signal R_c and pivot point based signal R_p:

$$R_t = R_c + R_p \tag{9-11}$$

It should be noted that the R_p signal is a feedforward term based on the inverse pivot point model. This model will continuously calculate the appropriate current ratio that would take the levitated object to the command position $\mathrm{y_c}$. If the feedforward term was not based on the system's inverse model, it would deviate the system from the desired position command and consequently would reduce the accuracy of the positioning system. The current divider block will receive the un-weighted current command u and the total ratio factor R_t and adjust the currents in the coils as:

$$I_1 = I_2 = I_3 = \left(1 + R_t\right)\mathrm{u} \tag{9-12}$$

$$I_4 = I_5 = I_6 = \left(1 - R_t\right)\mathrm{u} \tag{9-13}$$

$$I_7 = \mathrm{u} \tag{9-14}$$

A simple PID controller was designed for the system and the effect of signal R_p on the control performance was investigated in two experiments. In the first experiment, only signal R_c was utilized in the current calculations in each coil. In the second experiment, the pivot point based ratio factor R_p was added to the controller command and signal R_t was used in the current calculation.

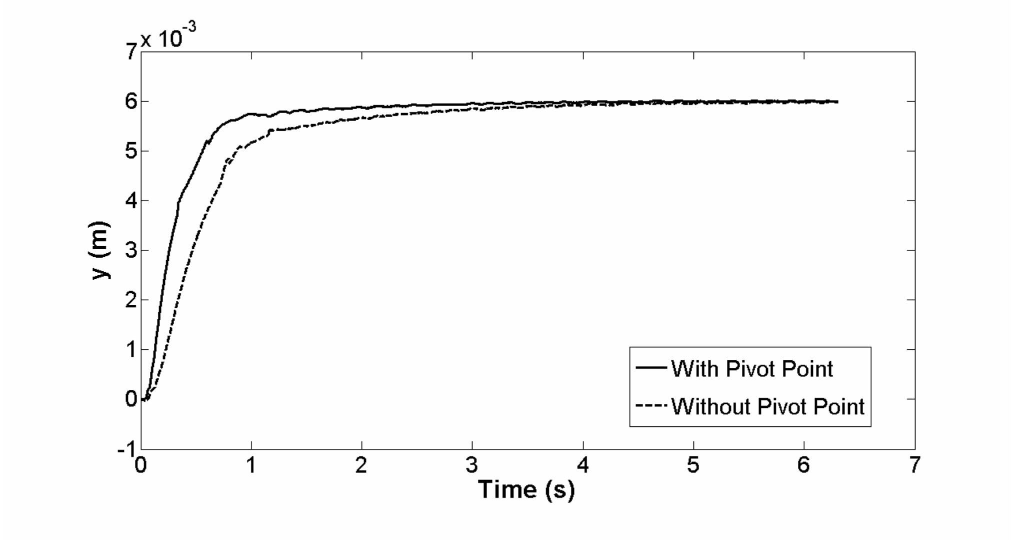

Figure 9-14: Pivot point effect in the horizontal position control of magnetic levitation system.

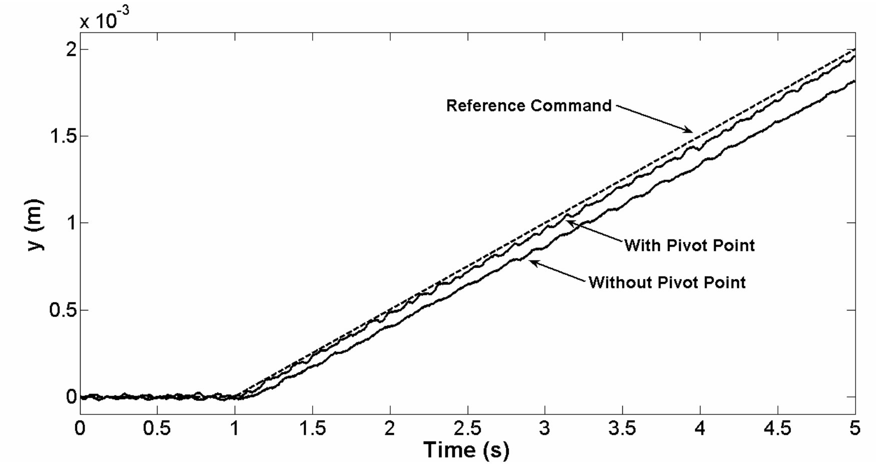

Figure 9-15: Pivot point effect in the ramp response during the horizontal position control.

Figure 9-14 compares the step responses of the control system with and without the use of pivot point based ratio factor R_p. As it can be seen in this figure, although the controller for both of the experiments was the same, the pivot point effect significantly improved the response of the system. Introducing the pivot point effect to the control system, the settling time of the response was reduced from 2.12(s) to 0.95(s). The pivot point effect also decreased the rise time of the system by approximately 0.3(s). Figure 9-15 illustrates the effect of inverse pivot point model in improving the ramp response characteristics of the horizontal position control system. The application of the pivot point based feedforward signal cut the steady state positioning error of the levitation system by three folds from $1.63\times10^{-4}\left(m\right)$ to $0.52\times10^{-4}\left(m\right)$.

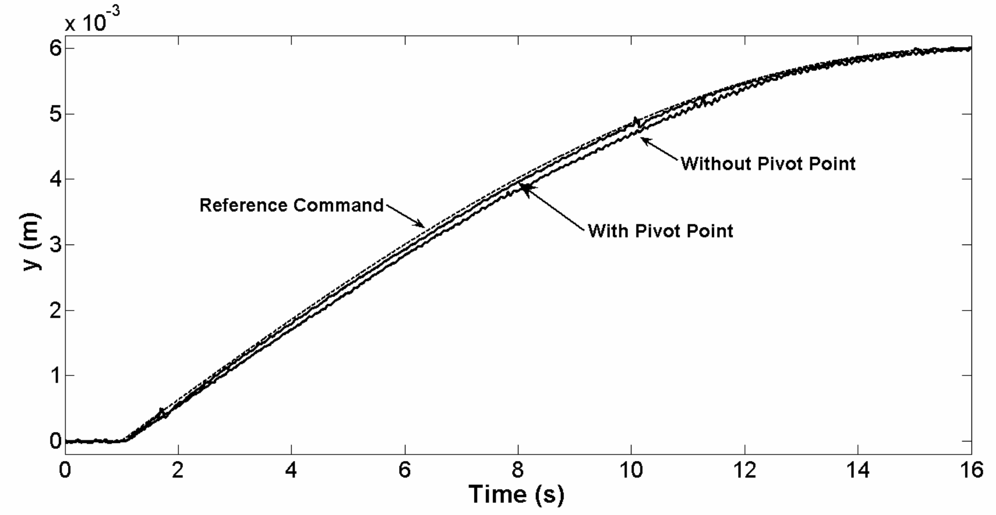

Figure 9-16: Pivot point effect in the trajectory tracking.

Application of the pivot point method also improved the accuracy of the trajectory tracking as shown in Figure 9-16. Table 9-2 provides the details of the improvements to the control system's performance obtained from Figure 9-14 and Figure 9-15. As it is seen in this table, the pivot point method reduced the settling time of the controller by 55%, the RMS positioning error by 58%, the steady state positioning error by 68%, and the rise time by 34%.

Table 9-2: The effect of pivot point method in the position control of the levitated object.

Property	**Without Pivot Point**	**With Pivot Point**
Settling time	2.12(s)	0.95(s)
RMS Error	19.3(μm)	8.1(μm)
Steady State Error	163(μm)	52(μm)
Rise time	0.87(s)	0.57(s)

Chapter 10

Conclusions and Recommendations

10.1. Conclusions

In this thesis, a large gap magnetic levitation system was entirely designed, fabricated and successfully tested at the Maglev Microrobotics Laboratory, University of Waterloo.

A compact mathematical model of the magnetic force was developed and several control strategies were proposed for the position control of the levitated object in three orthogonal directions. Experimental results showed that the proposed system is capable of positioning a levitated object with total positioning accuracy of 60 micrometers in complex trajectory tracking tasks.

One of the most important advantages of the magnetic levitation (maglev) systems compared to common actuation techniques is the lack of mechanical contact which makes maglev systems free of problems caused by friction, lubrication and sealing.

The concept of maglev systems is based on transferring magnetic energy from an outside source to magnetic susceptible objects enabling them to freely levitate against their weight. The outside source can be considered similar to the stator in electromagnetic machineries where as the magnetic levitated objects can be considered as the rotor.

In the proposed system, the external magnetic field is produced by magnetic drive unit (MDU). The MDU consists of three main parts i.e. electromagnets, pole piece and yoke.

There are seven electromagnets in the current design of the system responsible for converting the electrical current fed to the coils into magnetic field.

All the electromagnets are attached to a pole piece. The pole piece acts to unify the individual poles of the electromagnets in order to produce a unique point in a given horizontal plane where the magnetic force will counteract the weight of the levitated object.

The yoke is a C-shaped ferromagnetic piece used to generate a closed loop magnetic circuit. Levitation of the objects takes place in the air gap between the two yoke ends where the gradient of the magnetic field is highly increased due to the utilization of the yoke.

Vertical motion is achieved by changing the amount of power input to all of the electromagnets by an equal amount where as horizontal motion is achieved by varying the amount of power each electromagnet receives.

One of the challenges in the design of the maglev system is the highly nonlinear behavior of the magnetic materials in terms of magnetization pattern and hysteresis effect. With the aid of finite element method, a comprehensive finite element analysis was conducted aiming for the geometry design of the pole piece and yoke.

The design process followed by the detailed layout preparation of all the mechanical components and fabrication of the parts in Engineering Machine Shop, Department of Mechanical and Mechatronics Engineering, University of Waterloo.

Also, an extensive amount of instrument selection, interfacing and computer coding was completed to interface, debug and test all the electrical components of the magnetic levitation system and setup the test rig at its current level of operation.

As one of the essential steps towards obtaining the systems’ dynamic model, an accurate dynamic force model was developed for the levitation system. The model is capable of predicting the magnetic force experienced by the levitated object in terms of the current in the coils and the air gap.

With the aid of frequency response analysis, the individual mathematical models of the power amplifier and magnetic field were obtained. Combining these models resulted in the formation of a magnetic force model which takes the effect of the comprising parts of the maglev system into account.

In contrast with most of the proposed magnetic force models in the literature, the magnetic force equation obtained in this thesis assumes a linear relationship between the force and the electrical current in the coils. Moreover, the suggested model comprises a time dependant term which accounts for the delay due to the hysteresis in the magnetic parts and inductance in the coils.

The model was used in the controller design for the maglev system in the vertical direction. Three types of controllers were proposed i.e. feed forward PID (FF-PID), feedback linearization PID (FL-PID) and path planning model PID (PPM-PID).

The controller design process started with the implementation of a regular PID controller to prove the controllability of the levitation system. The gains of the PID controller were selected by trial and error.

In order to increase the stability of the PID controller, a feed forward compensator was added to the controller signal. This feed forward compensator is responsible to generate a signal which ideally would generate a magnetic force equal to the weight of the levitated object and cancel its effect.

The feed forward signal is calculated from the magnetic force model based on the steady state value of the electrical current required in the coils to produce a magnetic force equal to the weight of the levitated object positioned at the control set point.

As the first controller design attempt, the dynamic model of the levitation system was utilized in the design of a full state feedback controller with the desired closed loop poles of $\sigma_{d1} = -65$ and $\sigma_{d2} = -6$.

Due to modeling uncertainties, the state feedback controller showed a steady state error in the position control of the levitated object. Moreover, due to the discontinuity of the feed forward signal in step commands, the levitated object showed a sudden fall or rise at the time at which a positive or a negative step command was issued.

In order to eliminate the discontinuity in the feed forward signal and the steady state position error, two modifications were made. First the state feedback controller was replaced with a PID controller and second, a second order dynamic model was integrated in the feed forward calculation formula. The new controller was named as FF-PID.

The FF-PID controller significantly improved the response of the system compared to the state feedback controller.

In practice, it was seen that increasing the integrator gain in the FF-PID controller decreased the settling time of the controller, but inversely increased its overshoot. In order to improve both the overshoot and settling characteristics of the controller, a feed back linearization PID (FL-PID) controller was developed.

In the FL-PID controller, the inverse of magnetic force model is utilized in the calculation of the linearization signal aiming to cancel out the nonlinear effects of the levitation system.

Using similar PID controller gains for the FF-PID and FL-PID controllers, the FL-PID managed to reduce the settling time of the response from 2.45(s) to 1.25(s) which is equivalent to 49%. Also the overshoot of the response was reduced from 57.3% to 20.6%, equal to 64%. Improvement the FL-PID controller reduced the RMS positioning error of the FF-PID from 18.04(μm) to 11.56(μm), equal to 36%.

For the cases in which minimizing the overshoot of the system is the control objective, a path-planning model was implemented in the command signal. The controller is called PPM-PID.

The proposed controller significantly reduced the overshoot of the response. Compared with the FL-PID, the overshoot was reduced up to 66% from 20.6% to 7%. In terms of settling time, the PPM-PID controller showed a slower response compared with FL-PID resulting in an increase in the settling time.

Using the same PID gains as the FL-PID, the settling time of the PPM-PID was measured as 1.5 seconds which is 20% more than that of the FL-PID. The accuracy of positioning was also improved from 11.56(μm) for FL-PID to 8.67(μm) for PPM-PID which is equal to 25%. Table 10-1 compares the settling time, overshoot and positioning error of the FF-PID, FL-PID and PPM-PID controllers.

Table 10-1: Comparison between the settling time, overshoot and accuracy of the proposed controllers.

Controller Type:	**FF-PID**	**FL-PID**	**PPM-PID**
Settling time (s)	2.45	1.25	1.5
Overshoot (%)	57.3	20.6	7
RMS Error (μm)	18.04	11.56	8.67

In the design of all these three controllers, the levitated object was a 1(cm) x 1(cm) cylindrical permanent magnet with a constant mass of 6.59(gr).

In order to guarantee the accuracy and performance of the positioning system in levitating objects with variable mass, an adaptive controller was designed and implemented.

The adaptive controller uses a model reference adaptive feedback linearization (MRAFL) control law enabling the system to reject the effects caused by up to 30% of mass variations in the levitated object.

The levitated object is a microrobot equipped with a remote controlled gripper. The microrobot weighs approximately 28(gr) and is capable of lifting a payload as heavy as 8(gr).

In practice, it was seen that the proposed adaptive controller significantly improved the performance of the system in rejecting the mass variations. Experimental results showed that in the absence of payload, the FL-PID controller positioned the levitated microrobot with RMS error of 9.7(μm). In the presence of payload though, the FL-PID controller's accuracy degraded to 27.9(μm) due to the change in the mass of the object.

After applying the payload, it was seen that the variation in the accuracy of the MRAFL controller was far less than the FL-PID's accuracy variations. In the absence of the payload, the MRAFL controller positioned the microrobot with RMS error of 5.7(μm). In the presence of the payload, the accuracy of the MRAFL controller was measured as 8(μm).

The problem of three dimensional (3D) position control of the levitated object was tackled in two steps; vertical position control and horizontal position control. First, a FL-PID control law was used to stabilize the system at the desired distance below the pole piece. The signal calculated by the FL-PID controller was then used in a signal dividing formula to calculate the required current in each individual coil.

The location of the object in the horizontal plane was controlled using a regular PID controller. The levitated object in this case was a cylindrical 1(cm) x 1(cm) neodymium magnet with a remnant flux density of 1.3 Tesla. Several experiments were performed to test the performance of the proposed 3D controller.

Due to the uneven geometry of the levitation system with respect to the y axis, the proposed controller showed different step response characteristics along the positive and negative directions of the x axis.

The system showed promising results in positioning the object at a stationary point. For this case the positioning error in the x and y directions was recorded as 2.89(μm) and 7.15(μm) respectively.

Two trajectories were generated in the horizontal plane and the performance of the 3D control system was investigated. Experimental results showed that the proposed system is capable of performing a trajectory tracking task with overall accuracy of 60(μm).

Finally, a mathematical model was proposed so as to estimate the location of the maximum point of magnetic field for a given current distribution fed to the coils. The proposed model was experimentally verified and implemented is a position control task in horizontal direction.

10.2. Recommendations and Future Work

In practice it was seen that the use of seven electromagnets in the magnetic drive unit makes the system behavior in the x direction different from its behavior in the y direction. This problem happens as a result of unequal coil arrangement in each direction.

As a solution for this issue, it is suggested that the magnetic drive unit be redesigned so as to distribute the electromagnets in an even pattern with respect to x and y directions.

This might require a through redesign of pole piece, electromagnets and the power amplifier as the current of the power amplifier is limited to 3.55(A).

The redesign of the pole piece should also aim for finding a way to increase the lateral gradient of the magnetic field. Due to the fairly low gradients of the field in the horizontal plane, the amount of horizontal force experienced by the levitated object is very low.

Another recommendation is to use an active power amplifier. As mentioned in the previous chapters, the present power amplifier is a semi-active system meaning that it has no control over the current reduction in the coils. This will make an uneven effect on the response of the system to the positive and negative step commands.

In the modeling and control section, the identified system models serve as a suitable starting point for modeling the system. In this thesis the effect of delay in the electromagnets and hysteresis are neglected in the controller design process. The vertical system model can be improved by incorporating the electromagnet currents and magnetic field measurements into the closed loop system response. This will depend on the ability to obtain a suitable current signal from the amplifier of the system and an accurate magnetic field measurement in the air gap.

In order to improve the horizontal performance of the system, the damping effect of the aluminium block should be investigated in more detail. Also a dynamic horizontal force model should be obtained. This may require FEM modeling to determine the exact nature of how the eddy currents affect the system performance and how the magnetic field is shifted in horizontal directions. Also a model can be developed based on the correlation between the positioning performance of the system in vertical and horizontal directions to improve the overall positioning performance of the levitation system.

Another important step is to increase the degrees of freedom of the levitation system. This requires the redesign of the magnetic drive unit and the levitated object.

Appendix A

List of Publications

A.1. Journal Articles

[1] Ehsan Shameli , M.B. Khamesee, J.P. Huissoon, "Nonlinear controller design for a magnetic levitation device", Journal of Microsystems Technologies, Vol. 13, No. 8-10, 2007, pp. 831-835.

[2] E. Shameli, D.G. Craig, M.B. Khamesee, "Design and implementation of a magnetically suspended microrobotic pick-and-place system", Journal of Applied Physics, Vol. 99, No. 8, 2006, pp. 509-517.

[3] Caglar Elbuken, Ehsan Shameli, Mir Behrad Khamesee, "Modeling and analysis of eddy current damping for high precision magnetic levitation of a small magnet", IEEE Transactions on Magnetics, Vol. 43, No. 1, 2007, pp. 26-32.

[4] Mir Behrad Khamesee, Ehsan Shameli, "Pole piece effect on improvement of magnetic controllability for none-contact micromanipulation", IEEE Transactions on Magnetics, Vol. 43, No. 2, 2007, pp. 533-542.

[5] M.B. Khamesee, E. Shameli, "Regulation technique for a large gap magnetic field for 3D non-contact manipulation", Journal of Mechatronics, Vol. 15, Issue 9, Nov. 2005, pp. 1073-1087.

A.2. Refereed Conference Papers

[6] Ehsan Shameli, Mir Behrad Khamesee, Jan Paul Huissoon, "Frequency response identification and dynamic modeling of a magnetic levitation device", Proceedings of the 2007 ASME International Mechanical Engineering Congress and Exposition (IMECE 2007), Seattle, WA, USA, November 11-15, 2007.

[7] Ehsan Shameli , Mir Behrad Khamesee , Javed Ally , A. Amirfazli, "Modeling and Analysis of a Magnetic Positioning Device for Aerosol Particles Targeting in Biomedical Applications", Proceedings of the 6th International conference on Scientific and Clinical Applications of Magnetic Carriers, Krems, Austria, May 17-20, 2006.

Appendix B

Introduction to Electromagnetics

B.1. Review of Electromagnetic Theory

The whole subject of electromagnetics (EM) theory is based on Maxwell's four field equations and three medium-dependent equations. Before we briefly review these equations, it is helpful to state two important theorems commonly used in EM. These are the divergence (or Gauss's) theorem:

$$\oint_S \mathbf{F} \cdot d\mathbf{S} = \int_v \nabla \cdot \mathbf{F}\, dv \tag{B-1}$$

and Stokes's theorem:

$$\oint_L \mathbf{F} \cdot d\mathbf{l} = \int_S \nabla \times \mathbf{F} \cdot d\mathbf{S} \tag{B-2}$$

EM theory can be introduced as the study of fields produced by electric charges at rest and in motion [109]. Electrostatic fields are usually produced by static electric charges, whereas magnetostatic fields are due to motion of electric charges with uniform velocity (direct current). Dynamic or time-varying fields are usually due to accelerated charges or time-varying currents.

B.1.1. Electrostatic Fields

As mentioned, electrostatic fields are generated as a result of static electric charges. The two fundamental laws governing this type of field are Gauss's law:

$$\oint \mathbf{D} \cdot d\mathbf{S} = \int \rho_v\, dv \tag{B-3}$$

which is a direct consequence of Coulomb's force law, and the law describing electrostatic fields as conservative:

$$\oint \mathbf{E} \cdot d\mathbf{l} = 0 \tag{B-4}$$

In Eqs. (B-3) and (B-4), $\mathbf{D}$ is the electric flux density (in coulombs/meter^2), ρ_v is the volume charge density (in coulombs/meter^3) and $\mathbf{E}$ is the electric field intensity (in volts/meter). The integral form of the laws in Eqs. (B-3) and (B-4) can be expressed in the differential form by applying Eq. (B-1) to Eq. (B-3) and Eq. (B-2) to Eq. (B-4). We obtain:

$$\nabla \cdot \mathbf{D} = \rho_v \tag{B-5}$$

and,

$$\nabla \times \mathbf{E} = 0 \tag{B-6}$$

The vector fields $\mathbf{D}$ and $\mathbf{E}$ are related as:

$$\mathbf{D} = \varepsilon \mathbf{E} \tag{B-7}$$

where ε is the dielectric permittivity (in farads/meter) of the medium. In terms of the electric potential V (in volts), $\mathbf{E}$ is expressed as:

$$\mathbf{E} = -\nabla V \tag{B-8}$$

or

$$V = -\int \mathbf{E} \cdot d\mathbf{l} \tag{B-9}$$

Combining Eqs. (B-5), (B-7), and (B-8) gives Poisson's equation:

$$\nabla \cdot \varepsilon \nabla V = -\rho_v \tag{B-10).a}$$

or, if ε is constant:

$$\nabla^2 V = \frac{-\rho_v}{\varepsilon} \tag{2-10).b}$$

When $\rho_v = 0$, Eq. (B-10) becomes Laplace's equation:

$$\nabla \cdot \varepsilon \nabla V = 0 \tag{B-11).a}$$

or for constant ε :

$$\nabla^2 V = 0 \tag{2-11).b}$$

B.1.2. Magnetostatic Fields

Magnetostatic fields are produced due to motion of electric charges with uniform velocity. The basic laws of such fields are Ampere's law:

$$\oint_L \mathbf{H} \cdot d\mathbf{l} = \int_S \mathbf{J} \cdot d\mathbf{S} \tag{B-12}$$

and the law of conservation of magnetic flux (also called Gauss's law for magnetostatics):

$$\oint \mathbf{B} \cdot d\mathbf{S} = 0 \tag{B-13}$$

where $\mathbf{H}$ is the magnetic field intensity (in amperes/meter), $\mathbf{J}$ is the electric current density (in amperes/meter^2) and $\mathbf{B}$ is the magnetic flux density (in tesla or webers/meter^2).

Applying Eq. (B-2) to Eq. (B-11) and Eq. (B-1) to Eq. (B-13)yields their differential form as:

$$\nabla \times \mathbf{H} = \mathbf{J} \tag{B-14}$$

and,

$$\nabla \cdot \mathbf{B} = 0 \tag{B-15}$$

The vector fields $\mathbf{B}$ and $\mathbf{H}$ are related through the permeability μ (in henries/meter) of the medium as:

$$\mathbf{B} = \mu \mathbf{H} \tag{B-16}$$

Also, $\mathbf{J}$ is related to $\mathbf{E}$ through the conductivity σ (in mhos/meter) of the medium as:

$$\mathbf{J} = \sigma \mathbf{E} \tag{B-17}$$

This is usually referred to as Ohm's law. In terms of the magnetic vector potential $\mathbf{A}$ (in Wb/meter) [109]:

$$\mathbf{B} = \nabla \times \mathbf{A} \tag{B-18}$$

Applying the vector identity [110]:

$$\nabla \times \left(\nabla \times \mathbf{F} \right) = \nabla \left(\nabla \cdot \mathbf{F} \right) - \nabla^2 \mathbf{F} \tag{B-19}$$

to Eqs. (B-14) and (B-18) leads to Poisson's equation for magnetostatic fields:

$$\nabla^2 \mathbf{A} = -\mu \mathbf{J} \tag{B-20}$$

When $\mathbf{J} = 0$, Eq. (B-20) becomes Laplace's equation

$$\nabla^2 \mathbf{A} = 0 \tag{B-21}$$

B.1.3. Time-varying Fields

Dynamic or time-varying fields are usually due to accelerated charges or time-varying currents. In this case, electric and magnetic fields exist simultaneously. Equations (B-5) and (B-15) remain the same whereas Eqs. (B-6) and (B-14) require some modification for dynamic fields.

Modification of Eq. (B-6) is necessary to incorporate Faraday's law of induction, and that of Eq. (B-14) is warranted to allow for displacement current. The time-varying EM fields are governed by physical laws expressed mathematically as [109]:

$$\begin{aligned} \nabla \cdot \mathbf{D} &= \rho_v && (a) \\ \nabla \cdot \mathbf{B} &= 0 && (b) \\ \nabla \times \mathbf{E} &= -\frac{\partial \mathbf{B}}{\partial t} && (c) \\ \nabla \times \mathbf{H} &= \mathbf{J} + \frac{\partial \mathbf{D}}{\partial t} && (d) \end{aligned} \tag{B-22}$$

These equations are referred to as Maxwell's equations in the generalized form. They are first-order linear coupled differential equations relating the vector field quantities to each other. The equivalent integral form of Eq. (B-22) is:

$$\begin{aligned} &\oint_S \mathbf{D} \cdot d\mathbf{S} = \int_v \rho_v dv \\ &\oint_S \mathbf{B} \cdot d\mathbf{S} = 0 \\ &\oint_L \mathbf{E} \cdot d\mathbf{l} = -\int_S \frac{\partial \mathbf{B}}{\partial t} \cdot d\mathbf{S} \\ &\oint_L \mathbf{H} \cdot d\mathbf{l} = -\int_S \left(\mathbf{J} + \frac{\partial \mathbf{D}}{\partial t} \right) \cdot d\mathbf{S} \end{aligned} \tag{B-23}$$

In addition to these four Maxwell's equations, there are three medium-dependent equations:

$$\begin{aligned} \mathbf{D} &= \varepsilon \mathbf{E} \\ \mathbf{E} &= \mu \mathbf{H} \\ \mathbf{J} &= \sigma \mathbf{E} \end{aligned} \tag{B-24}$$

These are called constitutive relations for the medium in which the fields exist. Equations (B-22) and (B-24) form the seven postulated equations on which EM theory is based on. We must note that in the region where Maxwellian fields exist, the fields are assumed to be (a): single valued, (b): bounded, and (c): continuous functions of space and time with continuous derivatives.

It is worthwhile to mention two other fundamental equations that go hand in hand with Maxwell's equations. One is the Lorentz force equation:

$$\mathbf{F} = Q\left(\mathbf{E} + \mathbf{u} \times \mathbf{B}\right) \tag{B-25}$$

where $\mathbf{F}$ is the force exerted to a particle with charge Q moving at velocity $\mathbf{u}$ in an EM field; the Lorentz force equation constitutes a link between EM and mechanics.

The second equation is the continuity equation:

$$\nabla \cdot \mathbf{J} = -\frac{\partial \rho_v}{\partial t} \tag{B-26}$$

which expresses the conservation of electric charge. For each solution region, the EM equations will be solved subject to the boundary conditions imposed to the boundaries of that region.

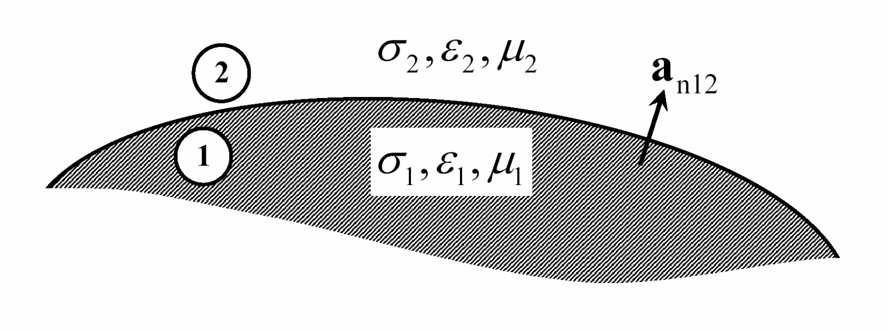

Figure B-1: Interface between two media.

B.1.4. Boundary Conditions

The material medium in which an EM field exists is usually characterized by its constitutive parameters σ, ε and μ. The medium is said to be linear if σ, ε and μ are independent of $\mathbf{E}$ and $\mathbf{H}$ or nonlinear otherwise. It is homogeneous if σ, ε and μ are not functions of space variables or inhomogeneous otherwise. It is isotropic if σ, ε and μ are independent of direction (scalars) or anisotropic otherwise.

The boundary conditions at the interface separating two different media 1 and 2, with parameters $(\sigma_1, \varepsilon_1, \mu_1)$ and $(\sigma_2, \varepsilon_2, \mu_2)$ as shown in Figure B-1, are easily derived from the integral form of Maxwell's equations.

They are:

$$\begin{aligned}
&E_{1t} - E_{2t} = 0 \quad &&or \quad (\mathbf{E}_1 - \mathbf{E}_2) \times \mathbf{a}_{n12} = 0 \\
&H_{1t} = H_{2t} = \mathrm{K} \quad &&or \quad (\mathbf{H}_1 - \mathbf{H}_2) \times \mathbf{a}_{n12} = \mathrm{K} \\
&D_{1n} - D_{2n} = \rho_S \quad &&or \quad (\mathbf{D}_1 - \mathbf{D}_2) \times \mathbf{a}_{n12} = \rho_S \\
&B_{1n} - B_{2n} = 0 \quad &&or \quad (\mathbf{B}_1 - \mathbf{B}_2) \times \mathbf{a}_{n12} = 0
\end{aligned} \tag{B-27}$$

where $\mathbf{a}$ is a unit normal vector directed from medium 1 to medium 2, subscripts 1 and 2 denote fields in regions 1 and 2, and subscripts t and n respectively denote tangent and normal components of the fields.

Equation (B-27) states that the tangential components of $\mathbf{E}$ and the normal components of $\mathbf{B}$ are continuous across the boundary. The tangential component of $\mathbf{H}$ is discontinuous by the surface current density K on the boundary.

This equation also states that the discontinuity in the normal component of $\mathbf{D}$ is the same as the surface charge density ρ_S on the boundary.

In practice, when a medium is source-free $(\mathbf{J} = 0, \rho_v = 0)$, only two of Maxwell's equations are used (Eqs. (B-22).c,d) since the other two are implied.

Also, in practice, it is sufficient to make the tangential components of the fields satisfy the necessary boundary conditions since the normal components implicitly satisfy their corresponding boundary conditions.

Since the solution of the Maxwell's equation in the coupled form is difficult, a useful trick is to decouple these equations to obtain a second-order differential equation that is easier to implement. This leads to the second-order EM equations.

B.2. Second-Order EM equations

As mentioned in the previous section, Maxwell's equations are coupled first-order differential equations which are difficult to apply when solving boundary-value problems. The difficulty is overcome by decoupling the first-order equations, thereby obtaining the wave equation, a second-order differential equation which is useful for solving problems [109].

B.2.1. Wave Equations

To obtain the wave equation for a linear, isotropic, homogeneous, source-free medium $\left(\mathbf{J}=0, \rho_v=0\right)$, from Eq. (B-22).c, we take the curl of both sides. This gives [109]:

$$\nabla \times \nabla \times \mathbf{E} = -\mu \frac{\partial}{\partial t}\left(\nabla \times \mathbf{H}\right) \tag{B-28}$$

From Eq. (B-22).d, we have:

$$\nabla \times \mathbf{H} = \varepsilon \frac{\partial \mathbf{E}}{\partial t}$$

since $\mathbf{J}=0$, so that Eq. (B-28) becomes:

$$\nabla \times \nabla \times \mathbf{E} = -\mu\varepsilon \frac{\partial^2 \mathbf{E}}{\partial t^2} \tag{B-29}$$

Applying the vector identity:

$$\nabla \times \left(\nabla \times \mathbf{F}\right) = \nabla\left(\nabla \cdot \mathbf{F}\right) - \nabla^2 \mathbf{F} \tag{B-30}$$

in Eq. (B-29), we have:

$$\nabla\left(\nabla \cdot \mathbf{E}\right) - \nabla^2 \mathbf{E} = -\mu\varepsilon \frac{\partial^2 \mathbf{E}}{\partial t^2}$$

Since $\rho_v = 0$, $\nabla \cdot \mathbf{E} = 0$ from Eq. (B-22).a, and hence we obtain:

$$\nabla^2 \mathbf{E} - \mu\varepsilon \frac{\partial^2 \mathbf{E}}{\partial t^2} = 0 \tag{B-31}$$

which is the time-dependent vector Helmholtz equation or simply wave equation.

If we had started the derivation with Eq. (B-22).d, we would obtain the wave equation for $\mathbf{H}$ as:

$$\nabla^2 \mathbf{H} - \mu\varepsilon \frac{\partial^2 \mathbf{H}}{\partial t^2} = 0 \tag{B-32}$$

Equations (B-31) and (B-32) are the equations of motion of EM waves in the medium under consideration. These waves are represented by the coupled $\mathbf{E}$ and $\mathbf{H}$ fields. The velocity (in m/s) of wave propagation is:

$$u = \frac{1}{\sqrt{\mu\varepsilon}} \tag{B-33}$$

where $u = c \approx 3\times 10^8 \ \left(m/s\right)$ in free space.

It should be noted that each of the vector equations in (B-31) and (B-32) has three scalar components, so that altogether we have six scalar equations for $E_x, E_y, E_z, H_x, H_y,$ and H_z. Thus each component of the wave equations has the form of [109]:

$$\nabla^2\Psi - \frac{1}{u^2}\frac{\partial^2\Psi}{\partial t^2} = 0 \qquad \text{(B-34)}$$

which is the scalar wave equation. If the medium is not source-free $\left(\mathbf{J} \neq 0, \rho_v \neq 0\right)$, the inhomogeneous form of wave equation will be implemented. This is done through the application of auxiliary time-varying potentials.

B.2.2. Time-varying Potentials

Generally speaking, we are often interested in electric and magnetic field intensities ($\mathbf{E}$ and $\mathbf{H}$), which are physically measurable quantities. However, it is often convenient to use auxiliary functions in analyzing an EM field. These auxiliary functions are the scalar electric potential V and vector magnetic potential $\mathbf{A}$ [110].

Although these potential functions are arbitrary, they are required to satisfy Maxwell's equations. Their derivation is based on two fundamental vector identities:

$$\nabla \times \nabla\Phi = 0 \qquad \text{(B-35)}$$

and,

$$\nabla \cdot \nabla \times \mathbf{F} = 0 \qquad \text{(B-36)}$$

which an arbitrary scalar field Φ and vector field $\mathbf{F}$ must satisfy.

Maxwell's equation (B-22).b along with Eq. (B-36) is satisfied if we define $\mathbf{A}$ such that:

$$\mathbf{B} = \nabla\times\mathbf{A} \qquad \text{(B-37)}$$

Substituting this into Eq. (B-22).c gives:

$$-\nabla\times\left(\mathbf{E} + \frac{\partial \mathbf{A}}{\partial t}\right) = 0$$

Since this equation has to be compatible with Eq. (B-35), we can choose the scalar field V such that:

$$\mathbf{E}+\frac{\partial \mathbf{A}}{\partial t}=-\nabla V$$

or,

$$\mathbf{E}=-\nabla V-\frac{\partial \mathbf{A}}{\partial t} \tag{B-38}$$

Thus, if we knew the potential functions V and $\mathbf{A}$, the fields $\mathbf{E}$ and $\mathbf{B}$ could be obtained from Eqs. (B-37) and (B-38). However, we still need to find the solution for the potential functions.

Substituting Eqs. (B-37) and (B-38) into Eq. (B-22).d and assuming linear, homogeneous medium, we have [109]:

$$\nabla \times \nabla \times \mathbf{A}=\mu \mathbf{J}+\varepsilon \mu \frac{\partial}{\partial t}\left(-\nabla V-\frac{\partial \mathbf{A}}{\partial t}\right)$$

Applying the vector identity in Eq. (B-30) leads to:

$$\nabla^2 \mathbf{A}-\nabla(\nabla \cdot \mathbf{A})=-\mu \mathbf{J}+\varepsilon \mu \nabla \frac{\partial^2 \mathbf{A}}{\partial t^2}+\varepsilon \mu \nabla \frac{\partial V}{\partial t} \tag{B-39}$$

Substituting Eq. (B-38) into Eq. (B-22).a gives:

$$\nabla^2 V+\frac{\partial}{\partial t} \nabla \cdot \mathbf{A}=-\frac{\rho_v}{\varepsilon} \tag{B-40}$$

According to the Helmholtz theorem of vector analysis, a vector is uniquely defined if and only if both its curl and divergence are specified. We have only specified the curl of $\mathbf{A}$ in Eq. (B-37); we may choose the divergence of $\mathbf{A}$ so that the differential equations (B-39) and (B-40) have the simplest forms possible. We achieve this in the so-called Lorentz condition:

$$\nabla \cdot \mathbf{A}=-\mu \varepsilon \frac{\partial V}{\partial t} \tag{B-41}$$

Incorporating this condition into Eqs. (B-39) and (B-40) results in:

$$\nabla^2 \mathbf{A}-\mu \varepsilon \frac{\partial^2 \mathbf{A}}{\partial t^2}=-\mu \mathbf{J} \tag{B-42}$$

and,

$$\nabla^2 V-\mu \varepsilon \frac{\partial^2 V}{\partial t^2}=-\frac{\rho_v}{\varepsilon} \tag{B-43}$$

which are inhomogeneous wave equations. Thus Maxwell's equations in terms of the potentials V and $\mathbf{A}$ reduce to the three equations (B-41) to (B-43).

In other words, the three equations are equivalent to the ordinary form of Maxwell's equations in that potentials satisfying these equations always lead to a solution of Maxwell's equations for $\mathbf{E}$ and $\mathbf{B}$ when used with Eqs. (B-37) and (B-38).

Integral solutions to Eqs. (B-42) and (B-43) are the so-called retarded potentials [109]:

$$\mathbf{A} = \int \frac{\mu[\mathbf{J}]dv}{4\pi R} \tag{B-44}$$

and,

$$V = \int \frac{[\rho_v]dv}{4\pi\varepsilon R} \tag{B-45}$$

where R is the distance from the source point to the field point, and the square brackets denote ρ_v and $\mathbf{J}$ are specified at a time $R(\mu\varepsilon)^{1/2}$ earlier than for which $\mathbf{A}$ or V is being determined.

B.2.3. Time-harmonic Fields

Up to this point, we have considered the general case of arbitrary time variation of EM fields. In many practical situations, especially at low frequencies, it is sufficient to deal with only the steady-state (or equilibrium) solution of EM fields when produced by sinusoidal currents.

Such fields are said to be sinusoidal time-varying or time-harmonic, that is, they vary at a sinusoidal frequency ω. An arbitrary time-dependent field $\mathbf{F}(x,y,z,t)$ or $\mathbf{F}(\mathbf{r},t)$ can be expressed as:

$$\mathbf{F}(\mathbf{r},t) = \mathrm{Re}\left[\mathbf{F}_S(\mathbf{r})e^{j\omega t}\right] \tag{B-46}$$

where $\mathbf{F}_S(\mathbf{r})$ is the phasor form of $\mathbf{F}(\mathbf{r},t)$ and is in general complex and ω is the angular frequency (in rad/s) of the sinusoidal excitation. The EM field quantities can be represented in phasor notation as [109]:

$$\begin{bmatrix} \mathbf{E}(\mathbf{r},t) \\ \mathbf{D}(\mathbf{r},t) \\ \mathbf{H}(\mathbf{r},t) \\ \mathbf{B}(\mathbf{r},t) \end{bmatrix} = \begin{bmatrix} \mathbf{E}_S(\mathbf{r}) \\ \mathbf{D}_S(\mathbf{r}) \\ \mathbf{H}_S(\mathbf{r}) \\ \mathbf{B}_S(\mathbf{r}) \end{bmatrix} e^{j\omega t} \tag{B-47}$$

Using the phasor representation allows us to replace the time derivations $\partial/\partial t$ by $j\omega$ since:

$$\frac{\partial e^{j\omega t}}{\partial t} = j\omega e^{j\omega t}$$

thus Maxwell's equations, in sinusoidal steady state, become:

$$\begin{aligned} \nabla \cdot \mathbf{D}_S &= \rho_{vS} && (a) \\ \nabla \cdot \mathbf{B}_S &= 0 && (b) \\ \nabla \times \mathbf{E}_S &= -j\omega \mathbf{B}_S && (c) \\ \nabla \times \mathbf{H}_S &= \mathbf{J}_S + j\omega \mathbf{D}_S && (d) \end{aligned} \tag{B-48}$$

We should observe that the effect of the time-harmonic assumption is to eliminate the time dependence from Maxwell's equations, thereby reducing the time-space dependence to space dependence only. A non-sinusoidal field can be represented as:

$$\mathbf{F}(\mathbf{r},t) = \mathrm{Re}\left[\int_{-\infty}^{\infty} \mathbf{F}_S(\mathbf{r},\omega) e^{j\omega t} d\omega\right] \tag{B-49}$$

Thus the solutions to Maxwell's equations for a non-sinusoidal field can be obtained by summing all the Fourier components $\mathbf{F}_S(\mathbf{r},\omega)$ over ω.

Replacing the time derivative in Eq. (B-34) by $(j\omega)^2$ yields the scalar wave equation in phasor representation as:

$$\nabla^2\Psi + k^2\Psi = 0 \tag{B-50}$$

where k is the propagation constant (in rad/m), given by:

$$k = \frac{\omega}{u} = \frac{2\pi f}{u} = \frac{2\pi}{\lambda} \tag{B-51}$$

We recall that Eqs. (B-31)-(B-34) are obtained assuming that $\rho_v = 0 = \mathbf{J}$. If $\rho_v \neq 0 \neq \mathbf{J}$, Eq. (B-50) will have the general form of:

$$\nabla^2\Psi + k^2\Psi = g \tag{B-52}$$

We notice that this Helmholtz equation reduces to either Poisson's equation:

$$\nabla^2\Psi = g \tag{B-53}$$

when k = 0 (i.e., $\omega = 0$ for static case) or Laplace's equation:

$$\nabla^2\Psi = 0 \tag{B-54}$$

when $k = 0 = g$.

Thus Poisson's and Laplace's equations are special cases of the Helmholtz equation. Note that function Ψ is said to be harmonic if it satisfies Laplace's equation.

B.3. Classification of EM Problems

Problem classification is an important concept because the general theory and methods of solution usually apply only to a given class of problems. Classifying EM problems will help us later to answer the question of what method is best for solving a given problem.

Continuum problems are categorized differently depending on the particular item of interest, which could be one of these:

(1) the solution region of the problem,

(2) the nature of the equation describing the problem,

(3) the associated boundary conditions.

It will be seen that these classifications are sometimes not independent of each other.

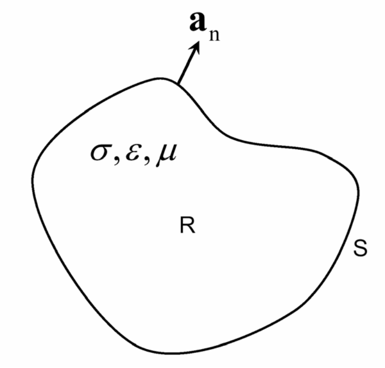

Figure B-2: Solution region R with boundary S.

B.3.1. Classification of Solution Regions

In terms of the solution region or problem domain, the problem could be an interior problem, also variably called an inner, closed, or bounded problem, or an exterior problem, also variably called an outer, open, or unbounded problem.

Consider the solution region R with boundary S, as shown in Figure B-2. If part or all of S is at infinity, R is open; otherwise R is closed.

For example, wave propagation in a waveguide is an interior problem, whereas wave propagation in free space, scattering of EM waves by raindrops and radiation from a dipole antenna are exterior.

A problem can also be classified in terms of the electrical, constitutive properties $(\sigma, \varepsilon, \mu)$ of the solution region. As mentioned in section B.1.4, the solution region could be linear (or nonlinear), homogeneous (or inhomogeneous), and isotropic (or anisotropic).

B.3.2. Classification of Differential Equations

EM problems are classified in terms of the equations describing them. The equations could be differential or integral or both. Most EM problems can be stated in terms of an operator equation:

$$L\Phi = g \tag{B-55}$$

where L is an operator (differential, integral, or integro-differential), g is the known excitation or source, and Φ is the unknown function to be determined.

A typical example is the electrostatic problem involving Poisson's equation. In differential form, Eq. (B-55) becomes:

$$-\nabla^2 V = \frac{\rho_v}{\varepsilon} \tag{B-56}$$

so that $L = -\nabla^2$ is the Laplacian operator, $g = \rho_v / \varepsilon$ is the source term, and $\Phi = V$ is the electric potential. In integral form, Poisson's equation is of the form

$$V = \int \frac{\rho_v dv}{4\pi\varepsilon r^2} \tag{B-57}$$

so that:

$$L = \int \frac{dv}{4\pi r^2} \quad , \quad g = V \quad , \quad \Phi = \rho_v / \varepsilon$$

As observed in Eqs. (B-52) to (B-54), EM problems involve linear, second-order differential equations. In general, a second-order partial differential equation (PDE) is given by:

$$a\Phi_{xx} + b\Phi_{xy} + c\Phi_{yy} + d\Phi_x + e\Phi_y + f\Phi = g \tag{B-58}$$

The coefficients a, b and c in general are functions of x and y; they may also depend on Φ itself, in which case the PDE is said to be nonlinear. Since most EM problems involve linear PDE, a, b and c will be regarded as constants.

A PDE in which g(x,y) in Eq. (B-58) equals zero is named homogeneous; it is inhomogeneous if $g(x, y) \neq 0$. It is important to note that Eq. (B-58) has the same form as Eq. (B-55), where L is now a differential operator given by:

$$L = a\frac{\partial^2}{\partial x^2} + b\frac{\partial^2}{\partial x \partial y} + c\frac{\partial^2}{\partial y^2} + d\frac{\partial}{\partial x} + e\frac{\partial}{\partial y} + f \tag{B-59}$$

A PDE in general can have both boundary values and initial values. PDEs whose boundary conditions are specified are called steady-state equations. If only initial values are specified, they are called transient equations.

Any linear second-order PDE can be classified as elliptic, hyperbolic, or parabolic depending on the coefficients a, b and c. Equation (B-58) is said to be:

$$\begin{aligned} &elliptic && if; \quad b^2 - 4ac < 0 \\ &hyperbolic && if; \quad b^2 - 4ac > 0 \\ &parabolic && if; \quad b^2 - 4ac = 0 \end{aligned} \tag{B-60}$$

The terms hyperbolic, parabolic, and elliptic are derived from the fact that the quadratic equation:

$$ax^2 + bxy + cy^2 + dx + ey + f = 0 \tag{B-61}$$

represents a hyperbola, parabola, or ellipse if $\left(b^2 - 4ac\right)$ is positive, zero, or negative, respectively [109].

In each of these categories, there are PDEs that model certain physical phenomena. Such phenomena are not limited to EM but extend to almost all areas of science and engineering.

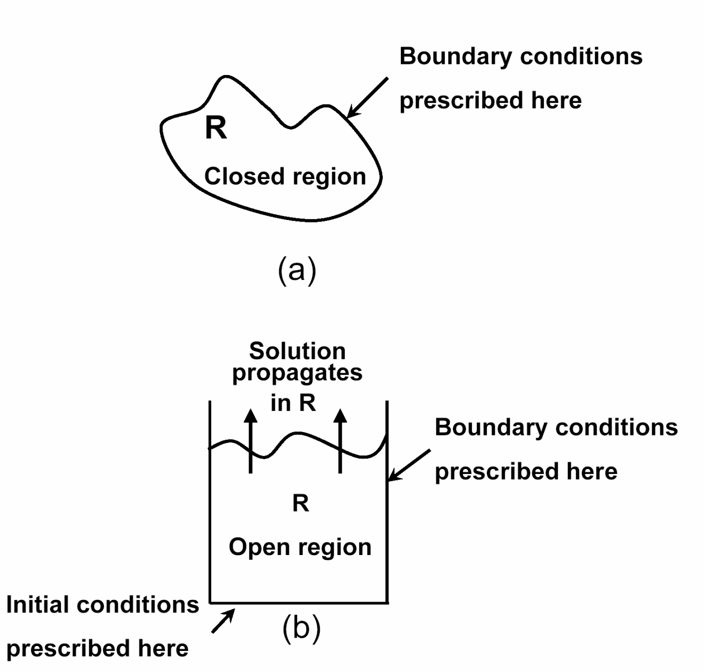

Figure B-3: (a) Elliptic, (b) parabolic or hyperbolic problem.

Thus the mathematical model specified in Eq. (B-58) arises in problems involving heat transfer, boundary-layer flow, vibrations, elasticity, electrostatic, wave propagation, and so on [109].

Elliptic PDEs are associated with steady-state phenomena, i.e., boundary-value problems. Typical examples of this type of PDE include Laplace's equation:

$$\frac{\partial^2 \Phi}{\partial x^2} + \frac{\partial^2 \Phi}{\partial y^2} = 0 \tag{B-62}$$

and Poisson's equation:

$$\frac{\partial^2 \Phi}{\partial x^2} + \frac{\partial^2 \Phi}{\partial y^2} = g\left(x, y\right) \tag{B-63}$$

where in both cases $a = c = 1, b = 0$. An elliptic PDE usually models an interior problem, and hence the solution region is usually closed or bounded as in Figure B-3(a).

Hyperbolic PDEs arise in propagation problems. The solution region is usually open so that a solution advances outward indefinitely from initial conditions while always satisfying specified boundary conditions. A typical example of hyperbolic PDE is the wave equation in one dimension [109]:

$$\frac{\partial^2\Phi}{\partial x^2} = \frac{1}{u^2}\frac{\partial^2\Phi}{\partial t^2} \tag{B-64}$$

where $a = u^2$, $b = 0$, $c = -1$. It is important to note that the wave equation in (B-50) is not hyperbolic but elliptic, since the time-dependence has been suppressed and the equation is merely the steady-state solution of Eq. (B-34).

Parabolic PDEs are generally associated with problems in which the quantity of interest varies slowly in comparison with the random motions which produce the variations.

The most common parabolic PDE is the diffusion (or heat) equation in one dimension:

$$\frac{\partial^2\Phi}{\partial x^2} = k\frac{\partial\Phi}{\partial t} \tag{B-65}$$

where $a = 1$, $b = 0 = c$. Like hyperbolic PDE, the solution region for parabolic PDE is usually open, as in Figure B-3(b).

The initial and boundary conditions typically associated with parabolic equations resemble those for hyperbolic problems except that only one initial condition at t = 0 is necessary since Eq. (1.64) is only first order in time.

Also, parabolic and hyperbolic equations are solved using similar techniques, whereas elliptic equations are usually more difficult and require different techniques.

It should be noted that: (1) since the coefficients a, b and c are in general functions of x and y, the classification of Eq. (B-58) may change from point to point in the solution region, and (2) PDEs with more than two independent variables $(x, y, z, t, ...)$ may not fit as neatly into the classification above.

A summary of the discussion in this section is shown in Table B-1. The type of problem represented by Eq. (B-55) is said to be deterministic, since the quantity of interest can be determined directly.

Another type of problem where the quantity is found indirectly is called nondeterministic or eigenvalue. The standard eigen problem is of the form,

$$L\Phi = \lambda\Phi \tag{B-66}$$

where the source term in Eq. (B-55) has been replaced by $\lambda\Phi$.

A more general version is the generalized eigenproblem having the form of:

$$L\Phi = \lambda M\Phi \tag{B-67}$$

where M , like L , is a linear operator for EM problems.

In Eqs. (B-66) and (B-67), only some particular values of λ called eigenvalues are permissible; associated with these values are the corresponding solutions Φ called eigenfunctions.

Eigenproblems are usually encountered in vibration and waveguide problems where the eigenvalues λ correspond to physical quantities such as resonance and cutoff frequencies, respectively.

Table B-1: Classification of Partial Differential Equations.

Type	**Sign of** b^2-4ac	**Example**	**Solution region**
Elliptic	−	Laplace's Equation: $\Phi_{xx}+\Phi_{yy}=0$	Closed
Hyperbolic	+	Wave Equation: $u^2\Phi_{xx}=\Phi_{tt}$	Open
Parabolic	0	Diffusion Equation: $\Phi_{xx}=k\Phi_t$	Open

B.3.3. Classification of Boundary Conditions

Our problem consists of finding the unknown function Φ of a partial differential equation. In addition to the fact that Φ satisfies Eq. (B-55) within a prescribed solution region R, Φ must satisfy certain conditions on S, the boundary of R.

Usually these boundary conditions are of the Dirichlet and Neumann types. Where a boundary condition has both, a mixed boundary condition is said to exist.

(1) Dirichlet Boundary Condition:

$$\Phi(r)=0 \quad , \quad r \text{ on } S \tag{B-68}$$

(2) Neumann Boundary Condition:

$$\frac{\partial \Phi(r)}{\partial n} = 0 \quad , \quad r \text{ on } S \tag{B-69}$$

(3) Mixed Boundary Condition:

$$\frac{\partial \Phi(r)}{\partial n} + h(r)\Phi(r) = 0 \quad , \quad r \text{ on } S \tag{B-70}$$

where $h(r)$ is a known function and is the directional derivative of Φ along the outward normal to the boundary S, i.e.,

$$\frac{\partial \Phi}{\partial n} = \nabla \Phi \cdot \mathbf{a}_n \tag{B-71}$$

where $\mathbf{a}_n$ is a unit normal directed out of R, as shown in Figure B-2.

Note that the Neumann boundary condition is a special case of the mixed condition with $h(r) = 0$. The conditions in Eq. (B-68) to (B-70) are called homogeneous boundary conditions. The more general ones are the inhomogeneous:

(1) Inhomogeneous Dirichlet:

$$\Phi(r) = p(r) \quad , \quad r \text{ on } S \tag{B-72}$$

(2) Inhomogeneous Neumann:

$$\frac{\partial \Phi(r)}{\partial n} = q(r) \quad , \quad r \text{ on } S \tag{B-73}$$

(3) Inhomogeneous Mixed:

$$\frac{\partial \Phi(r)}{\partial n} + h(r)\Phi(r) = w(r) \quad , \quad r \text{ on } S \tag{B-74}$$

where $p(r)$, $q(r)$, and $w(r)$ are explicitly known functions on the boundary S.

For example, $\Phi(0) = 1$ is an inhomogeneous Dirichlet boundary condition, and the associated homogeneous counterpart is $\Phi(0) = 0$. Also $\Phi'(1) = 2$ and $\Phi'(1) = 0$ are, respectively, inhomogeneous and homogeneous Neumann boundary conditions.

In electrostatics, for example, if the value of electric potential is specified on S, we have Dirichlet boundary condition, whereas if the surface charge $\left(\rho_S = D_n = \varepsilon \frac{\partial V}{\partial n} \right)$ is specified, the boundary condition is Neumann.

The problem of finding a function Φ that is harmonic in a region is called Dirichlet problem (or Neumann problem) if Φ (or $\frac{\partial \Phi}{\partial n}$) is prescribed on the boundary of the region.

It is worth observing that the term "homogeneous" has been used to mean different things. The solution region could be homogeneous meaning that σ, ε and μ are constant within R; the PDE could be homogeneous if g = 0 so that $L\Phi = 0$; and the boundary conditions are homogeneous when $p(r) = q(r) = w(r) = 0$.

Appendix C

Amplifier Performance

Figure C-1 illustrates the standard deviations measured on each amplifier's channel using the amplifier display and a multimeter for three different voltage inputs.

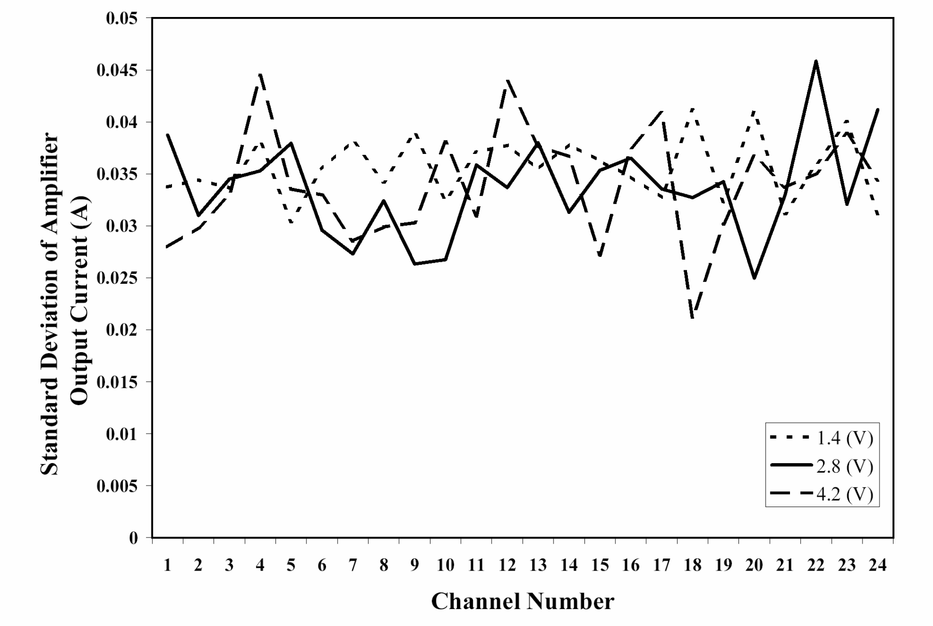

Figure C-1: Standard deviation of individual amplifier channels for input voltages of 1.4, 2.8 and 4.2 volts.

The numerical values used for the generation of this figure are listed in Table C-1. In Table C-2, the average output measured on each channel is presented.

Table C-1: Standard deviation of amplifier output current.

	Input Voltage (V)		
	1.4	**2.8**	**4.2**
Channel	**Std. Dev.**	**Std. Dev.**	**Std. Dev.**
1	0.033733	0.038736	0.027976
2	0.034416	0.031006	0.029823
3	0.033648	0.034495	0.032924
4	0.038142	0.035289	0.044467
5	0.030404	0.037937	0.033549
6	0.035484	0.029582	0.032961
7	0.038188	0.027289	0.028544
8	0.034203	0.032409	0.029889
9	0.038965	0.026331	0.030301
10	0.032438	0.026748	0.038088
11	0.037082	0.035852	0.030955
12	0.037751	0.033675	0.043924
13	0.03547	0.037983	0.037674
14	0.037825	0.031298	0.036648
15	0.036232	0.035336	0.027185
16	0.03472	0.036511	0.037481
17	0.032712	0.033549	0.040882
18	0.041166	0.032711	0.021112
19	0.032267	0.034249	0.030154
20	0.041018	0.024964	0.036758
21	0.031155	0.032997	0.033697
22	0.035913	0.045835	0.035032
23	0.04	0.032063	0.038867
24	0.031149	0.041179	0.034415

Table C-2: Amplifier outputs.

	Input Voltage (V)					
	1.4		2.8		4.2	
Channel	Amplifier Reading (A)	Multimeter Reading (A)	Amplifier Reading (A)	Multimeter Reading (A)	Amplifier Reading (A)	Multimeter Reading (A)
1	0.49	0.48	0.977	0.95	1.464	1.43
2	0.493	0.48	0.98	0.95	1.467	1.43
3	0.49	0.485	0.974	0.96	1.46	1.45
4	0.492	0.49	0.978	0.97	1.462	1.46
5	0.486	0.485	0.9695	0.96	1.453	1.45
6	0.491	0.49	0.981	0.96	1.4715	1.45
7	0.4895	0.49	0.9745	0.97	1.4605	1.45
8	0.4875	0.48	0.973	0.96	1.459	1.44
9	0.489	0.49	0.9725	0.97	1.4575	1.45
10	0.492	0.49	0.981	0.965	1.4695	1.45
11	0.493	0.48	0.981	0.96	1.4705	1.43
12	0.489	0.48	0.9735	0.96	1.4595	1.44
13	0.49	0.48	0.977	0.96	1.464	1.44
14	0.4875	0.48	0.9695	0.96	1.451	1.44
15	0.4925	0.49	0.9815	0.975	1.4705	1.46
16	0.4925	0.49	0.9825	0.97	1.4725	1.45
17	0.489	0.49	0.974	0.97	1.4585	1.45
18	0.494	0.49	0.9825	0.975	1.471	1.46
19	0.485	0.48	0.9695	0.96	1.451	1.44
20	0.4915	0.49	0.979	0.97	1.4655	1.46
21	0.4895	0.49	0.9795	0.97	1.4675	1.46
22	0.4875	0.49	0.971	0.97	1.455	1.46
23	0.495	0.49	0.982	0.975	1.47	1.46
24	0.491	0.48	0.978	0.96	1.4635	1.43

Appendix D

DAQ Accuracy

The Relevent DAQ properties are listed in Table D-1.

Table D-1: NI-PXI-6251 Characteristics [117].

Input Range	+/- 10 volts
Number of Bits	16
Resolution	0.305 mV
Random Noise Variance	280 µVrms
Gain Error	83e-6 V/V
Offset Error	20e-6 V/V
Gain Temperature Sensitivity	13e-6 V/(V°C)
Offset Temperature Sensitivity	21e-6 V/(V°C)
Reference Temperature Sensitivity	1e-6 V/(V°C)
Integral Non-Linearity Error	60e-6 V/V

The accuracy for a given measurement is calculated as follows:

$$\begin{aligned}\text{Net Gain Error} = {} & \text{Gain Error} \\ & + \text{Gain Temperature Sensitivty} \times \Delta T_i \\ & + \text{Reference Temperature Sensitivty} \times \Delta T_e\end{aligned} \tag{D-1}$$

Where ΔT_i is the temperature change since the last internal calibration and ΔT_e is the temperature change since the last external calibration. The net offset error is calculated as:

$$\begin{aligned}\text{Net Offset Error} = {} & \text{Offset Error} \\ & + \text{Offset Temperature Senitivity} \times \Delta \text{Ti} \\ & + \text{Integral Non-Linearity Error}\end{aligned} \tag{D-2}$$

Also, the noise uncertainty is calculated as:

$$\text{Noise Uncertianty} = \text{Random Noise} \times 3\ \times \text{n}^{-0.5} \qquad \text{(D-3)}$$

Where n is the number of averaging measurements. For the current setup, n=1. The absolute accuracy is calculated as:

$$\begin{aligned}\text{Absolute Accuracy} = {} & \text{Reading} \times \text{Net Gain Error} \\ & + \text{Range} \times \text{Net Offset Error} \\ & + \text{Noise Uncertainty}\end{aligned} \qquad \text{(D-4)}$$

Using the standard values of $\Delta \text{T}_\text{i} = 1°C$ and $\Delta \text{T}_\text{e} = 10°C$ as given in [117], we have:

$$\text{Net Gain Error} = 83\times10^{-6} + 13\times10^{-6} + 10\times10^{-6} = 103\times10^{-6}\left(V/V\right) \qquad \text{(D-5)}$$

$$\text{Net Offset} = 20\times10^{-6} + 21\times10^{-6} + 60\times10^{-6} = 101\times10^{-6}\left(V/V\right) \qquad \text{(D-6)}$$

$$\text{Noise Uncertainty} = 3\times280\times10^{-6} = 840\times10^{-6}\left(V\right) \qquad \text{(D-7)}$$

Therefore, using Eq. (D-4), the accuracies at $0\left(V\right)$ and $10\left(V\right)$ readings are calculated as 1850(μV) and 2880(μV) respectively.

Appendix E

Sample Accuracy Calculation

A nominal measurement N by the laser micrometer will have an associated accuracy *a*. So the actual measurement may be:

$$\begin{gathered} N+a \\ N-a \end{gathered} \tag{E-1}$$

This measurement will be converted into a voltage by the laser micrometer as:

$$\begin{gathered} V=\frac{(N+a-20)}{2} \\ V=\frac{(N-a-20)}{2} \end{gathered} \tag{E-2}$$

It is assumed that the board rounds to the nearest resolution point, which is 0.01 mm. The DAQ resolution is given as 305(μV). The number of bits *n* required to represent the input voltage is calculated as:

$$n=\frac{V}{305\times10^{-6}} \tag{E-3}$$

This must be rounded to the nearest integer value, and then *n* must be multiplied by the resolution to find the actual input voltage seen by the calculation.

Based on the DAQ accuracy discussed in Appendix B, the absolute accuracy of the measurement can be calculated and the worst case actual input voltages can be calculated.

This will yield four V_{DAQ} measurements, a high and low worst case voltage for each of the possible two worst case inputs. Finally, the voltage is converted back into the actual position measurement $N_{measured}$ as:

$$N_{measured}=2V_{DAQ}+20 \tag{E-4}$$

Therefore, V_{DAQ} is calculated as:

$$V_{DAQ}=\frac{N_{measured}-20}{2} \tag{E-5}$$

A sample calculation is shown in Table E-1.

Table E-1: Sample accuracy calculation.

Nominal Measurement	30.001 (mm)
Accuracy (Given by the Manufacturer)	0.004 (mm)
Possible Actual Measurements	30.005 (mm) 29.997 (mm)
Keyence Board Resolution	0.01 (mm)
Measurement if board rounds to nearest	30.01 (mm) 30 (mm)
Equivalent Voltage from Eq. (E-5)	5.005 (V) 5 (V)
DAQ resolution	0.000305 (V)
#Bits needed from Eq. (E-3)	16409.84 16393.44
Effective # bits	16410 16394
Effective input voltage from Eq. (E-3)	5.00505 (V) 5.00017 (V)
DAQ Accuracy from Appendix B	0.00288 (V)
Possible Voltage Measurements	5.00793 (V) 5.00217 (V) 5.00305 (V) 4.99719 (V)
Effective Measurement from Eq. (E-4)	30.01586 (mm) 30.00434 (mm) 30.00610 (mm) 29.99438 (mm)
Error	-0.01486 (mm) -0.00334 (mm) -0.00510 (mm) 0.00662 (mm)

Appendix F

Stability of the FL-PID Controller

Let assume that the actual governing equation of the system is:

$$\left(\frac{\alpha}{m}z+\frac{\beta}{m}\right)u-g=\ddot{z} \tag{F-1}$$

where α and β are two constant coefficients of the system and u is the controller signal sent to the power amplifier. The controller communicates with the power amplifier via an analogue voltage ranging between 0 to 10 volts. Therefore, the final controller signal is always bounded to:

$$0\le u\le 10 \tag{F-2}$$

The positioning error is defined as the difference between a desired position z_c and measured position z as:

$$e=z_c-z \tag{F-3}$$

Assume that the estimated parameters of the system used in the controller design are $\hat{\alpha}$ and $\hat{\beta}$. Now let define the state space variables of the system as:

$$X_1=z-z_C \tag{F-4}$$

$$X_2=\dot{z} \tag{F-5}$$

$$X_3=\int\left(z-z_C\right)\,dt \tag{F-6}$$

The FL-PID control signal is calculated as:

$$u=\frac{g}{\alpha z+\beta}-K_1X_1-K_2X_2-K_3X_3 \quad , \quad 0\le u\le 10 \tag{F-7}$$

where K_1, K_2, and K_3 are the proportional, derivative and integral gains of the FL-PID controller respectively. Substituting Eq. (F-7) into Eq. (F-1) we have:

$$\ddot{z}=\left[\frac{g}{\alpha\left(X_1+z_C\right)+\beta}-K_1X_1-K_2X_2-K_3X_3\right]\left[\alpha\left(X_1+z_C\right)+\beta\right]-g \tag{F-8}$$

Therefore, the state space representation of the system will be obtained as:

$$\begin{aligned}
\dot{X}_1 &= X_2 \\
\dot{X}_2 &= \left[\frac{g}{\alpha\left(X_1+z_\mathrm{C}\right)+\beta} - K_1X_1 - K_2X_2 - K_3X_3\right]\left[\alpha\left(X_1+z_\mathrm{C}\right)+\beta\right]-g \\
\dot{X}_3 &= X_1
\end{aligned} \tag{F-9}$$

Equation (F-9) can be rewritten as,

$$\begin{aligned}
\dot{X}_1 &= X_2 \\
\dot{X}_2 &= \left(\alpha z_\mathrm{C}+\beta\right)\left[-K_1X_1 - K_2X_2 - K_3X_3\right]+\alpha X_1\left[-K_1X_1 - K_2X_2 - K_3X_3\right] \\
\dot{X}_3 &= X_1
\end{aligned} \tag{F-10}$$

In the matrix form, equation (F-10) is expressed as:

$$\dot{\mathbf{X}} = \underbrace{\begin{bmatrix} 0 & 1 & 0 \\ -\left(\alpha z_\mathrm{C}+\beta\right)K_1 & -\left(\alpha z_\mathrm{C}+\beta\right)K_2 & -\left(\alpha z_\mathrm{C}+\beta\right)K_3 \\ 1 & 0 & 0 \end{bmatrix}}_{\mathbf{A}}\mathbf{X} + \underbrace{\begin{bmatrix} 0 \\ 1 \\ 0 \end{bmatrix}}_{\mathbf{B}}\delta\left(\mathbf{X}\right) \tag{F-11}$$

Where α, β, K_1, K_2 and K_3 are positive constants. Also, $\delta\left(\mathbf{X}\right)$ is the disturbance term and the controller gains are selected so that matrix $\mathbf{A}$ is Hurwitz. The disturbance term can be rewritten as:

$$\delta\left(\mathbf{X}\right) = -\alpha K_1X_1^2 - \alpha K_2X_1X_2 - \alpha K_3X_1X_3 \tag{F-12}$$

From algebraic inequalities we have:

$$\left|X_1X_2\right| \le \frac{1}{2}\left(X_1^2+X_2^2\right) \le \frac{1}{2}\left\|\mathbf{X}\right\|^2 \tag{F-13}$$

Therefore,

$$-\alpha K_1X_1^2 \le \alpha K_1\left\|\mathbf{X}\right\|^2 \tag{F-14}$$

$$-\alpha K_2X_1X_2 \le \frac{\alpha K_2}{2}\left\|\mathbf{X}\right\|^2 \tag{F-15}$$

$$-\alpha K_2X_1X_3 \le \frac{\alpha K_3}{2}\left\|\mathbf{X}\right\|^2 \tag{F-16}$$

Hence,

$$\left|\delta\left(\mathbf{X}\right)\right| \le \gamma\left\|\mathbf{X}\right\|^2 \tag{F-17}$$

where,

$$\gamma = \alpha K_1 + \frac{\alpha K_2}{2} + \frac{\alpha K_3}{2} \tag{F-18}$$

Now, since $\mathbf{A}$ is Hurwitz, the following Lyapunov equation has a positive definite and symmetric solution P,

$$\mathbf{A}^T\mathbf{P} + \mathbf{PA} = -\mathbf{I} \tag{F-19}$$

Where, **I** is the identity matrix. Now consider a Lyapunov function V(**X**) in the form of:

$$V(\mathbf{X}) = \mathbf{X}^T\mathbf{PX} \tag{F-20}$$

As P is positive definite, V(**X**) is positive definite too. In addition there exists positive numbers λ_1 and λ_2 such that:

$$\lambda_2 \|\mathbf{X}\|^2 \le V(\mathbf{X}) \le \lambda_1 \|\mathbf{X}\|^2 \tag{F-21}$$

where,

$$\lambda_2 = \min\left[\mathrm{eig}(\mathbf{P})\right] \tag{F-22}$$

$$\lambda_1 = \max\left[\mathrm{eig}(\mathbf{P})\right] \tag{F-23}$$

Differentiating V(**X**) versus time yields:

$$\begin{aligned}\dot{V} &= \dot{\mathbf{X}}^T\mathbf{PX} + \mathbf{X}^T\mathbf{P}\dot{\mathbf{X}} = \mathbf{X}^T(\mathbf{A}^T\mathbf{P} + \mathbf{PA})\mathbf{X} + \delta(\mathbf{X})^T\mathbf{B}^T\mathbf{PX} + \mathbf{X}^T\mathbf{PB}\delta(\mathbf{X}) \\ &= -\mathbf{X}^T\mathbf{X} + 2\mathbf{X}^T\mathbf{PB}\delta(\mathbf{X})^T \le -\|\mathbf{X}\|^2 + 2\gamma\|\mathbf{PB}\|\|\mathbf{X}\|^3 = -\left[1 - 2\gamma\|\mathbf{PB}\| \cdot \|\mathbf{X}\|\right]\|\mathbf{X}\|^2\end{aligned} \tag{F-24}$$

Now let $0 < \psi < 1$ be an arbitrary constant. It can be easily shown that in the domain Ω, we have,

$$\dot{V} \le -\psi \|\mathbf{X}\|^2 \tag{F-25}$$

where Ω is defined as,

$$\Omega : \|\mathbf{X}\| \le \frac{1-\psi}{2\gamma\|\mathbf{PB}\|} \tag{F-26}$$

Therefore, if $\mathbf{X}$ is selected in domain Ω, the system is locally stable.
Combination of equations (F-21) and (F-25) yields:

$$\dot{V} \le -\psi\|\mathbf{X}\|^2 \le \frac{-\psi}{\lambda_1}V \quad \Rightarrow \quad V(t) \le V(0)\exp\left(\frac{-\psi}{\lambda_1}t\right) \tag{F-27}$$

Therefore, in domain Ω, V exponentially converges to zero. On the other hand,

$$\lambda_2\|\mathbf{X}\|^2 \le V(t) \tag{F-28}$$

Hence,

$$\left\| X(t) \right\|^2 \le \frac{1}{\lambda_2} V(0) \exp\left(\frac{-\psi}{\lambda_1} t \right) \quad \Rightarrow \quad \left\| X(t) \right\| \le \sqrt{\frac{V(0)}{\lambda_2}} \exp\left(\frac{-\psi}{2\lambda_1} t \right) \qquad \text{(F-29)}$$

And therefore, the system is locally exponentially stable.

References

[1] Tsukamoto O., Yasuda K., Chen J. Z., "A new magnetic levitation system with AC magnets", IEEE Transactions on Magnetism, Volume: 24, Issue: 2, March 1988, pp. 1497-1500.

[2] Park K.H., Ahn K.Y., Kim S.H., Kwak Y.K., “Wafer distribution system for a clean room using a novel magnetic suspension technique”, IEEE/ASME Transactions on Mechatronics, Volume: 3 , Issue: 1 , March 1998, pp. 73 – 78.

[3] Park K.H., Lee, S.K., Yi, J.H., Kim S.H., Kwak Y.K., Wang I.A., “Contactless magnetically levitated silicon wafer transport system”, Journal of Mechatronics, Vol. 6, No. 5, Aug. 1996, pp. 591-610.

[4] Yamakawa H., Moriyama I., Minamigawa Y., Maeba Y., Takematsu T., Nishitsuji M., Fujiki O., Asaishi T., Koike T., “Contamination-free transfer of silicon wafers with a magnetic levitation transport system in vacuum”, Proceedings of the 11th International Vacuum Congress (IVC-11) and the 7th International Conference on Solid Surfaces(ICSS-7), Vol. 41, No. 7-9 Pt3, Sept. 1990, pp. 1843-1845.

[5] Morizane T., Kimura N.; Taniguchi K., “Simultaneous control of propulsion and levitation of linear induction motor in a novel Maglev system”, Proceedings the 3rd International Power Electronics and Motion Control Conference, Volume: 1, Aug. 2000, Pages:127 – 131.

[6] Wang I. Y. A.; Li S. H.; Busch-Vishniac I., "A magnetic levitation transport path", IEEE Transactions on Semiconductor Manufacturing, Volume: 4, Issue: 2, May 1991, pp. 145-154.

[7] Kim W. J., Trumper D. L., “High-precision magnetic levitation stage for photolithography”, Journal of Precision Engineering, Vol. 22, 1998, pp. 66–77.

[8] Holmes M.; Hocken R., Trumper D. L., “The long-range scanning stage: a novel platform for scanned-probe microscopy” Journal of Precision Engineering, Vol. 24, Issue: 3, 2000, pp. 191–209.

[9] Williams M.E., Trumper D.L., Hocken R., “Magnetic bearing stage for photolithography”, CIRP Annals, Vol. 42, No. 1, 1993, pp. 607-610.

[10] Levis M., Maggiore Manfred, “Nonlinear control of planar magnetic levitation system”, Proceedings of 42nd IEEE conference on decision and control, Dec. 2003, pp. 6578-6583.

[11] Unger B., Hollis R., "Design and operation of a force-reflecting magnetic levitation coarse-fine teleoperation system", Proceedings of the 2004 IEEE International Conference on Robotics and Automation, Volume: 4, May 2004, pp. 4147-4152.

[12] Salcudean S.E., Wong N.M.; Hollis R.L., "Design and control of a force-reflecting teleoperation system with magnetically levitated master and wrist", IEEE Transactions on Robotics and Automation, Volume: 11, Issue: 6, Dec. 1995, pp. 844-858.

[13] Salcudean S. E., Wong N. M., Hollis R. L., "A force-reflecting teleoperation system with magnetically levitated master and wrist", Proceedings IEEE International Conference on Robotics and Automation, Vol. 2, May 1992, pp. 1420-1426.

[14] Tsuda. N., Kato N., Nomura Y., Matsui H., "Design framework of teleoperating system for magnetically levitated robot with force-feedback", Proceedings of SPIE - The International Society for Optical Engineering, Vol. 4570, Oct. 2001, pp. 25-33.

[15] Lin C.E.; Yang C. K., "Force and moment calibration for NCKU 10 cm×10 cm magnetic suspension wind tunnel", Proceedings of IEEE Instrumentation and Measurement Technology Conference, Volume: 2, May 2004, pp. 1060-1065.

[16] Lin C. E., Yang C. K., Liu K. H., Jou H. L., “Improvement on drag and control performance in NCKU magnetic suspension wind tunnel”, Proceedings of the National Science Council, Republic of China, Part A: Physical Science and Engineering, Vol. 24, No. 5, Sep. 2000, pp. 330-340.

[17] Lin C. E., Jou H. L., Sheu Y. R., “System implementation of measurement and control for a magnetic suspension wind tunnel”, Proceedings of the 1995 IEEE Instrumentation and Measurement Technology Conference, Apr. 1995, pp. 200-205.

[18] Smith M.R.; Eyssa Y.M.; Van Scivrr S.W., "Design of a superconducting magnetic suspension system for a liquid helium flow experiment", IEEE Transactions on Applied Superconductivity, Volume: 7, Issue: 2, Aug. 1996, pp. 382-385.

[19] Boom R.; Eyssa Y.; McIntosh G.; Abdelsalam M.; Scurlock R.; Wu Y.; Goodyer M.; Balcerek K.; Eskins J.; Britcher C., "Superconducting electromagnets for large wind tunnel magnetic suspension and balance systems", IEEE Transactions on Magnetics, Volume: 21 , Issue: 2, Mar. 1985, pp. 444-447.

[20] Britcher C. P., Goodyer M. J., Scurlock R. G., Wu Y. Y., “flying superconducting magnet and cryostat for magnetic suspension of wind-tunnel models”, Cryogenics, Vol. 24, No. 4, Apr. 1984, pp. 185-189.

[21] Britcher C. P., “Progress towards large wind tunnel magnetic suspension and balance systems”, AIAA 22nd Aerospace Sciences Meeting, 1984.

[22] Britcher C. P., “Progress toward magnetic suspension and balance systems for large wind tunnels”, Journal of Aircraft, Vol. 22, No. 4, Apr. 1985, pp. 264-269.

[23] Britcher C. P., Goodyer M. J., Eskins J., Parker D., Halford R. J., “Digital control of wind tunnel magnetic suspension and balance systems”, International Congress on Instrumentation in Aerospace Simulation Facilities, 1987, pp. 334-342.

[24] Johnson W. G. Jr., Dress D. A., “13-inch magnetic suspension and balance system wind tunnel”, NASA Technical Memorandum, No. 4090, Jan. 1989.

[25] Daniels T. S., Tripp J. S., “Improvements to an electromagnetic position sensor for a magnetic suspension wind tunnel”, Proceedings of the 34th International Instrumentation Symposium, Vol. 34, May 1988, pp. 65-70.

[26] Covert E. E., “Magnetic suspension and balance systems for use with wind tunnels”, International Congress on Instrumentation in Aerospace Simulation Facilities, 1987, pp. 283-294.

[27] McIntosh G. E., Abdelsalam M. K., Boom R. W., Eyssa Y. M., “magnetic suspension and balance system (MSBS) advanced study - II: superconducting solenoid and magnetic wings for wind tunnel models”, International Congress on Instrumentation in Aerospace Simulation Facilities, 1987, pp. 303-307.

[28] Martindale W. R., Butler R. W., Starr R. F., “Study on needs for a magnetic suspension system operating with a transonic wind tunnel”, NASA Contractor Reports, May 1985.

[29] LaFleur S., “Advanced optical position sensors for magnetically suspended wind tunnel models”, International Congress on Instrumentation in Aerospace Simulation Facilities, 1985, pp. 106-114.

[30] Jang G. H., Park J. S., “Development of a highly efficient hard disk drive spindle motor with a passive magnetic thrust bearing and a hydrodynamic journal bearing”, Journal of Applied Physics, Vol. 97, No. 10, May 2005, pp. 507-510.

[31] Cannon D. M., Brereton M., Dill H., Sullivan M., “Design of a compliant passive magnetic bearing for use in SIRTF's Tertiary Mirror Assembly”, Proceedings of SPIE - The International Society for Optical Engineering, Vol. 1340, 1990, pp. 373-382.

[32] Cunningham D., Davis P., “Multiaxis passive isolation system for a magnetic bearing reaction wheel”, Advances in the Astronautical Sciences, Vol. 81, 1993, pp. 454.

[33] Siebert M., Ebihara B., Jansen R., Fusaro R. L., Kascak A., Kenny A., “A passive magnetic bearing flywheel”, Proceedings of the Intersociety Energy Conversion Engineering Conference, Vol. 1, 2001, pp. 125-132.

[34] Marion-Pera M. C., Yonnet J. P., “Study of permanent magnet arrangements for superconducting passive bearings”, IEEE Transactions on Magnetics, Vol. 30, No. 6, Part 1, Nov 1994, pp. 4743-4745.

[35] Komori M.; Shiraishi C., "A levitated motor with superconducting magnetic bearings assisted by self-sensing AMBs", IEEE Transactions on Applied Superconductivity, Volume: 13, Issue: 2, June 2003, pp. 2189-2192.

[36] Mukhopadhyay S. C.; Ohji T.; Iwahara M.; Yamada S., "Modeling and control of a new horizontal-shaft hybrid-type magnetic bearing", IEEE Transactions on Industrial Electronics, Volume: 47, Issue: 1, Feb. 2000, pp. 100-108.

[37] Mukhopadhyay S.C.; Donaldson J.; Sengupta G.; Yamada S; Chakraborty C.; Kacprzak D., "Fabrication of a repulsive-type magnetic bearing using a novel arrangement of permanent magnets for vertical-rotor suspension", IEEE Transactions on Magnetics, Volume: 39 , Issue: 5, Sept. 2003, pp. 3220-3222.

[38] Filatov A. V., Poluschenko O. L., Shin S. C., “A new approach to the design of passive magnetic bearings using high-temperature superconductors”, Cryogenics, Vol. 38, No. 6, Jun. 1998, pp. 595-600.

[39] Filatov A. V., Maslen E. H., “Passive magnetic bearing for flywheel energy storage systems”, IEEE Transactions on Magnetics, Vol. 37, No. 6, Nov. 2001, pp. 3913-3924.

[40] Wilcock D. F., Eusepi M., “passive magnetic-thrust bearing for energy-storage flywheels”, ASLE Transactions, Vol. 25, No. 1, Jan. 1982, pp. 7-16.

[41] Ichihara T., Matsunaga K., Kita M., Hirabayashi I., Isono M., Hirose M., Yoshii K., Kurihara K., Saito O., Saito S., Murakami M., Takabayashi H., Natsumeda M., Koshizuka N., “Fabrication and evaluation of superconducting magnetic bearing for 10 kW h-class flywheel energy storage system”, Physica C: Superconductivity and its Applications, Vol. 426-431, No. I, Oct. 2005, pp. 752-758.

[42] Koshizuka N., Matsunaga K., Yamachi N., Kawaji A., Hirabayashi H., Murakami M., Tomita M., Une S., Saito S., Isono M., Nasu H., Maeda T., Ishikawa F., “Construction of the stator installed in the superconducting magnetic bearing for a 10 kWh flywheel”, Physica C: Superconductivity and its Applications, Vol. 412-414, Special Issue, Oct. 2004, pp. 756-760.

[43] Matsunaga K., Tomita M., Yamachi N.. Iida K., Yoshioka J., Isono M., Hirose M., Nasu H., Kameno H., Kubo A., Takahata R., Kitai N., Yamamoto H., Nakamura Y., Koshizuka N., Murakami M., “Fabrication and evaluation of superconducting bearing module for 10 kW h flywheel”, Physica C: Superconductivity and its Applications, Vol. 378-381, Part 1, Oct. 2002, pp. 883-887.

[44] Bassani R., “Levitation of passive magnetic bearings and systems”, Tribology International, Vol. 39, no. 9, Sep. 2006, pp. 963-970.

[45] Bassani R., Ciulli E., “Passive magnetic bearings low instability and possible stability”, Proceedings of the World Tribology Congress III-2005, 2005, pp. 89-90.

[46] Bassani R., “Dynamic stability of passive magnetic bearings”, Nonlinear Dynamics, Vol. 50, No. 1-2, Oct. 2007, pp. 161-168.

[47] Wang F., Wang J., Kong Z., Xu L., “A Novel BLDC motor with passive magnetic bearings for blood pump application”, 2003 IEEE Industry Applications Conference; 38th IAS Annual Meeting: Crossroads To Innovation, Vol. 2, Oct. 2003, pp. 1429-1433.

[48] Qian K. X., Yuan H. Y., Zeng P., Ru W. M., “A novel permanent maglev rotary LVAD with passive magnetic bearings”, Journal of Medical Engineering and Technology, Vol. 29, No. 5, Sep./Oct. 2005, pp. 235-237.

[49] Qian K. X., Wan F.K., Ru W. M., Zeng P., Yuan H. Y., “Study on stable equilibrium of levitated impeller in rotary pump with passive magnetic bearings”, Journal of Medical Engineering and Technology, Vol. 30, No. 2, Mar./Apr. 2006, pp. 78-82.

[50] Polajzer B., Stumberger G., Dolinar D., Hameyer K., “Design of a radial active magnetic bearing”, Proceedings of 17th Symposium of Electromagnetic Phenomena in Nonlinear Circuits, Jul. 2002, pp. 55-58.

[51] Polajzer B., Stumberger G., Dolinar D., “Numerical analysis of radial active magnetic bearings”, 12th International Power Electronics & Motion Control Conference, 2006, pp. 1913-1918.

[52] Polajzer B., Stumberger G., Dolinar D., “Impact of iron core saturation on radial forces of active magnetic bearings”, Przeglad Elektrotechniczny, Vol. 82, No. 5, 2006, pp. 41-43.

[53] Polajzer B., Stumberger G., Dolinar D., Hameyer K., “Determination of a dynamic radial active magnetic bearing model using the finite element method”, Journal for Computation and Mathematics in Electrical and Electronic Engineering, Vol. 23, No. 3, 2004, pp. 783-788.

[54] Polajzer B., Stumberger G., Ritonja J., Tezak O., Dolinar D., Hameyer K., “Impact of magnetic nonlinearities and cross-coupling effects on properties of radial active magnetic bearings”, IEEE Transactions on Magnetics, Vol. 40, No. 2, Part 2, March 2004, pp. 798-801.

[55] Polajer B., Dolinar D., Stumberger G., Hameyer K., “Force calculation of the laboratory implementation of a radial active magnetic bearing”, Journal of Technical Physics, Vol. 43, No. 4, 2002, pp. 453-457.

[56] Polajzer B., Dolinar D., Stumberger G., Tezak O., Hameyer K., “Analysis of the laboratory implementation of a radial active magnetic bearing”, Electromagnetic Fields in Electrical Engineering (ISEF 01), Sep. 2001, pp. 502-507.

[57] Nicolsky R., Gorelov Y., Pereira A. S., David D. F. B., Santisteban A., Stephan R. M., Ripper A., De Andrade R. Jr., Gawalek W., Habisreuther T., Strasser T., “Superconducting axial bearing for induction machines with active radial magnetic bearings”, IEEE Transactions on Applied Superconductivity, Vol. 9, No. 2, Part 1, Jun 1999, pp. 964-967.

[58] Nicolsky R., De Andrade R. Jr., Ripper A., David D. F. B., Santisteban J. A., Stephan R. M., Gawalek W., Habisreuther T., Strasser T., “Superconducting-electromagnetic hybrid bearing using YBCO bulk blocks for passive axial levitation”, Superconductor Science and Technology, Vol. 13, No. 6, Jun 2000, pp. 870-874.

[59] Nicolsky R., Pereira A. S., De Andrade R. Jr., David D. F. B., Santisteban J. A., Stephan R. M., Ripper A., Gawalek W., Habisreuther T., Strasser T., “Development of hybrid bearing system with thrust superconducting magnetic bearing and radial active electromagnetic bearing”, Physica C: Superconductivity and its Applications, Vol. 4, Feb. 2000, pp. 2509-2512.

[60] Nicolsky R., Gorelov Y. A., “Pseudo-hysteretic behavior in semiconductor-superconductor junction”, Physica C: Superconductivity and its Applications, Vol. 4, Feb. 2000, pp. 2735-2736.

[61] Nicolsky R., “Metallic weak-link character of grain boundaries in high-Tc materials”, Proceedings of the International Winter School Conference: Electronic Properties of High-Tc Superconductors, 1993, pp. 88.

[62] Nicolsky R., “Andreev reflections and critical currents in high Tc superconductors”, Cryogenics, Vol. 29, No. 3A, Mar. 1989, pp. 388-391.

[63] Schulz A., Schneeberger M., Wassermann J., “A reliable switching amplifier driving an active magnetic bearing - Experimental results”, Proceedings of the IEEE International Conference on Industrial Technology, Dec. 2005, pp. 389-394.

[64] Schulz A., Schneeberger M., Wassermann J., “A reliable switching amplifier for active magnetic bearings error detection strategies and measurement results”, Proceedings of the IEEE International Conference on Industrial Technology, Vol. 2, Dec. 2004, pp. 701-707.

[65] Schulz A., Wassermann J., Schneeberger M., “A reliable switching amplifier for active magnetic bearings”, Proceedings of the IEEE International Conference on Industrial Technology, Vol. 1, Dec. 2003, pp. 198-202.

[66] Brown G. V., DiRusso E., Provenza A. J., “An active magnetic bearing with high Tc superconducting coils and ferromagnetic Cores”, Advances in Cryogenic Engineering, No. 41/A, 1996, pp. 973.

[67] Brown G. V., DiRusso E., Provenza A. J., “Active homopolar magnetic bearing with high temperature superconductor coils and ferromagnetic cores”, NASA Technical Memorandum, No. 106916, Aug. 1995.

[68] Brown G. V., DiRusso E., Provensa A. J., “Active magnetic bearing with high TC superconducting coils and ferromagnetic cores”, NASA Technical Memorandum, No. 106995, Jul. 1995.

[69] Matsuda K., Kanemitsu Y., Kijimoto S., “Optimal number of stator poles for compact active radial magnetic bearings”, IEEE Transactions on Magnetics, Vol. 43, No. 8, Aug. 2007, pp. 3420-3427.

[70] Knospe C. R., “Active magnetic bearings for machining applications”, Control Engineering Practice, Vol. 15, No. 3, Special Issue, Mar. 2007, pp. 307-313.

[71] Lee K. C., Jeong Y. H., Koo D. H., Hyeong J. A., “Development of a radial active magnetic bearing for high speed turbo-machinery motors”, 2006 SICE-ICASE International Joint Conference (IEEE Cat. No.06TH8879), Oct. 2006, pp. 6-12.

[72] Arai K. I., Honda T., “Micromagnetic actuators”, Robotica, Vol. 14, Sep./Oct. 1996, pp. 477-481.

[73] Dario P., Valleggi R., Carrozza M. C., Montesi M. C., Cocco M., “Microactuators for microrobots: a critical survey”, Journal of Micromechanics and Microengineering, Vol. 2, No. 3, Sep. 1992, pp. 141-157.

[74] Rembold U., Fatikow S., “Autonomous microrobots”, Journal of Intelligent and Robotic Systems, Vol. 19, 1997, pp. 375–391.

[75] Shuxiang G., Fukuda T., Asaka K., “A new type of fish-like underwater microrobot”, IEEE/ASME Transactions on Mechatronics, Vol. 8, No. 1, 2003, pp. 136-141.

[76] Stefanini C., Carrozza M. C., Dario P., “A mobile microrobot driven by a new type of electromagnetic micromotor”, 7th International Symposium on Micro Machine and Human Science, 1996, pp. 195-201.

[77] Lyshevski S. E., “Micromanipulators actuated by micromotors”, Proceedings of the 41st IEEE Conference on Decision and Control, 2002, pp. 3658-3663.

[78] Suzumori K., Kohei H., Toyomi M., “A direct drive pneumatic stepper motor for robots: designs for pipe inspection microrobots and human care robots, Proceedings of the 1998 IEEE International Conference on Robotics and Automation, 1998, pp. 3047-3052.

[79] Shibata T., Takanari S., Nobuaki K., “Development of in-pipe microrobot using microwave energy transmission”, Electronics and Communications in Japan, Part 2, Vol. 84, No. 11, 2001, pp. 704-710.

[80] Hollar S., Flynn A., Bellew C., Pister K. S. J., “Solar powered 10 mg silicon robot”, Proceedings of the IEEE Micro Electro Mechanical Systems (MEMS), 2003, pp. 706-711.

[81] Sakakibara T., Izua H., Shibata T., Tarui H., Shibata K., Kiyama S., Kawahara N., “Multi-Source power supply system using micro –photovoltaic devices combined with microwave antenna”, Proceedings of the IEEE Micro Electro Mechanical Systems (MEMS), 2001, pp. 192-195.

[82] Batzel T. D., Lee K. Y., “Electric propulsion with the sensorless permanent magnet synchronous motor: model and approach”, IEEE Transactions on Energy Conversion, Vol. 20, No. 4, Dec. 2005, pp. 818-825.

[83] Batzel T. D., Lee K. Y., “Electric propulsion with sensorless permanent magnet synchronous motor: implementation and performance”, IEEE Transactions on Energy Conversion, Vol. 20, No. 3, Sep. 2005, pp. 575-583.

[84] Mathieu J. B., Beaudoin G., Martel S., “Method of propulsion of a ferromagnetic core in the cardiovascular system through magnetic gradients generated by an MRI system”, IEEE Transactions on Biomedical Engineering, Vol. 53, No. 2, Feb. 2006, pp. 292-299.

[85] Mathieu J. B., Martel S., “Magnetic steering of Iron Oxide microparticles using propulsion gradient coils in MRI”, Proceedings of the 28th Annual International

Conference of the IEEE Engineering in Medicine and Biology Society, 2006, pp. 472-475.

[86] Mathieu J. B., Martel S., Yahia L. H., Soulez G., Beaudoin G., “Preliminary studies for using magnetic resonance imaging systems as a mean of propulsion for microrobots in blood vessels and evaluation of ferromagnetic artifacts”, Canadian Conference on Electrical and Computer Engineering, Vol. 2, 2003, pp. 835-838.

[87] Mathieu J. B., Martel S., Yahia L. H., Soulez G., Beaudoin G., “Preliminary investigation of the feasibility of magnetic propulsion for future microdevices in blood vessels”, Bio-Medical Materials and Engineering, Vol. 15, No. 5, 2005, pp. 367-374.

[88] Miki M., Tokura S., Hayakawa H., Inami H., Kitano M., Matsuzaki H., Kimura Y., Ohtani I., Morita E., Ogata H., Izumi M., Sugimoto H., Ida T., “Development of a synchronous motor with Gd-Ba-Cu-O bulk superconductors as pole-field magnets for propulsion system”, Superconductor Science & Technology, Vol. 19, No. 7, Jul. 2006, pp. 494-499.

[89] Ohashi S., Dodo D., “Influence of the propulsion system on the levitation characteristics of the HTSC-permanent magnet hybrid magnetically levitated system” IEEE Transactions on Applied Superconductivity, Vol. 17, No. 2, Jun. 2007, p 2083-2086.

[90] Ohashi S., “Levitation and propulsion for the magnetically levitated conveyance system using two phase linear motor”, Transactions of the Institute of Electrical Engineers of Japan, Part D, Vol. 126D, No. 6, 2006, pp. 812-817.

[91] Khamesee M. B., Shameli E., “Pole piece effect on improvement of magnetic controllability for noncontact micromanipulation”, IEEE Transactions on Magnetics, Vol. 43, No. 2, Feb. 2007, pp. 533-542.

[92] Khamesee M.B., Shameli E., “Regulation technique for a large gap magnetic field for 3D non-contact manipulation”, Mechatronics, Vol. 15, No. 9, Nov. 2005, pp. 1073-1087.

[93] Khamesee M. B., Kato N., Nomura Y., Nakamura T., “Design and control of a microrobotic system using magnetic levitation”, IEEE/ASME Transactions on Mechatronics, Vol. 7, No. 1, March 2002, pp. 1-14.

[94] Khamesee M. B., Nakamura T., Kato N., Nomura Y., Mizutani K., “Teleoperated microhand for operation in small insulation chambers”, Proceedings of the ASCE Specialty Conference on Robotics for Challenging Environments, 1998, pp. 321-327.

[95] Elbuken C., Shameli E., Khamesee M. B., “Modeling and analysis of eddy-current damping for high-precision magnetic levitation of a small magnet”, IEEE Transactions on Magnetics, Vol. 43, No. 1, Jan. 2007, pp. 26-32.

[96] Nakamura T., Khamesee M. B., “Prototype mechanism for three-dimensional levitated movement of a small magnet”, IEEE/ASME Transactions on Mechatronics, Vol. 2, No. 1, Mar. 1997, pp. 41-50.

[97] Nakamura T., Khamesee M. B., “Mechanism for three dimensional levitated movement of a small magnet”, International Workshop on Advanced Motion Control, AMC, Vol. 2, 1996, pp. 464-469.

[98] Roch I., Bidaud Ph., Collard D., Buchaillot L., “Fabrication and characterization of an SU-8 gripper actuated by a shape memory alloy thin film”, Journal of Micromechanics and Microengineering, Vol. 13, No. 2, Mar. 2003, pp. 330-336.

[99] Huang W. M., Gao X. Y., Loo B. K., He L. M., Ngoi B. K. A., “Micro-gripper using two-way NiTi shape-memory alloy thin sheet”, Materials Science Forum, Vol. 394-395, 2002, pp. 87-90.

[100] Zhang H., Burdet E., Hutmacher D W., Poo A. N., Bellouard Y., Clavel R., Sidler T., “Robotic micro-assembly of scaffold/cell constructs with a shape memory alloy gripper”, Proceedings-IEEE International Conference on Robotics and Automation, Vol. 2, 2002, pp. 1483-1488.

[101] Choi S. B., Han Y. M., Kim J. H., Cheong C. C., “Force tracking control of a flexible gripper featuring shape memory alloy actuators”, Mechatronics, Vol. 11, No. 6, Sep. 2001, pp. 677-690.

[102] Escher K., Hornbogen E., “Shape memory alloys for robot grippers and mechanical hands”, European Space Agency, (Special Publication) ESA SP, No. 299, 1989, pp. 27-32.

[103] Jeon C. S., Park J. S., Lee S. Y., Moon C. W., “Fabrication and characteristics of out-of-plane piezoelectric micro grippers using MEMS processes”, Thin Solid Films, Vol. 515, No. 12, Apr. 2007, pp. 4901-4904.

[104] Xinhan H., Jianhua C., Min W., Xiadong L., “A piezoelectric bimorph micro-gripper with micro-force sensing”, Proceedings of 2005 International Conference on Information Acquisition, 2005, pp. 145-149.

[105] Karjalainen I.,Sandelin T., Heikkila R., Tuokko R., “Using piezoelectric technology to improve servo gripper performance in mini- and microassembly”, Assembly Automation, Vol. 25, No. 2, 2005, pp. 117-123.

[106] Kim W. H., Park J. S., Shin K. S., Park K. B., Seong W. K., Moon C. W., “Simulation and fabrication of silicon micro-grippers actuated by piezoelectric actuator”, Materials Science Forum, Vol. 475-479, No. III, PRICM 5: The Fifth Pacific Rim International Conference on Advanced Materials and Processing, 2005, pp. 1885-1888.

[107] Sun L., Chen J., Sun P., “Design of milli-grippers using piezoelectric actuator as well as electromagnetic force”, Proceedings of the International Symposium on Micromechatronics and Human Science, 1995, pp. 199-204.

[108] Barsky M. F., Lindner D. K., Claus R. O., “Robot gripper control system using PVDF piezoelectric sensors”, IEEE Transactions on Ultrasonics, Ferroelectrics, and Frequency Control, Vol. 36, No. 1, Jan. 1989, pp. 129-134.

[109] Hermann A. Haus and James R. Melcher, Electromagnetic Fields and Energy, Prentice Hall, Englewood Cliffs, NJ, 1989.

[110] Nathan Ida and Joao P.A. Bastos, Electromagnetics and Calculation of Fields, Second Edition, Springer, 1997.

[111] Tirupathi R. Chandrupatla and Ashok D. Belgundu, Introduction to Finite Elements in Engineering, Third Edition, Prentice Hall, Englewood Cliffs, NJ, 1997.

[112] D. Bruce Montgomery, Solenoid Magnet Design : The Magnetic and Mechanical Aspects of Resistive and Superconducting Systems, Wiley and Interscience, 1969.

[113] Deeley E. M., “Avoiding surface impedance modification in BE methods by singularity-free representations”, IEEE Transaction on Magnetics, Vol. 28, Issue 5, Sep. 1992, pp. 2814-2816.

[114] Deeley E. M., Xiang J., “The use of modified surface impedance in a minimum-order boundary element method”, IEEE Transaction on Magnetics, Vol. 26, Issue 5, Sep. 1992, pp. 2762 - 2764.

[115] "Product evaluation report", S. G. Smallwood Inc., Waterloo, Canada, 2005.

[116] "High speed laser scan micrometer LS-5000 series instruction manual", Keyence Corporation, Japan, 1996.

[117] "NI-625x specification", National Instruments Online Internet Document available at http://www.ni.com/pdf/manuals/371291d.pdf, Last accessed July 8, 2006.

[118] "NI-PXI-6733 data sheet", National Instruments Online Internet Document available at http://www.ni.com/pdf/products/us/4daqsc362-365_372-373_368.pdf, Last accessed July 8, 2006.

[119] "Sorensen DSC series data sheet", Sorensen Online Internet Document available at http://www.elgar.com/pdfs/datasheets/DSC.pdf, Last accessed July 8, 2006.

[120] Peterson K. S., Grizzle J. W., Stefanopoulou A. G., "Nonlinear control for magnetic levitation of automotive engine vales", IEEE Transaction on Control Systems Technology, Vol. 14, No. 2, Mar. 2006, pp.346-54.

[121] Alvarez-Sanchez E., Alvarez-Gallegos J., Castro-Linares R., "Modeling and controller design of a magnetic levitation system", 2nd International Conference on Electrical and Electronics Engineering, Vol. 5, Sep. 2005, pp. 330-334.

[122] Jiunshian P., Jianming L., Yasser M., Yahaghi T., "Neuro-sliding mode control for magnetic levitation systems", IEEE International Symposium on Circuits and Systems (ISCAS 2005), Vol. 5, May 2005, pp. 5130-5133.

[123] Fallaha C., Kanaan H., Saad M., "Real time implementation of a sliding mode regulator for current-controlled magnetic levitation system", Proceedings of the 2005 IEEE International Symposium on Intelligent Control, Vol. 1, Jun. 2005, pp.696-701.

[124] Jalili-Kharaajoo M., "Sliding mode control of voltage-controlled magnetic levitation systems", Proceedings of 2003 IEEE Conference on Control Applications, Vol. 1, Jun. 2003, pp. 83-86.

[125] Jalili-Kharaajoo M., "Robust variable structure control applied to voltage-controlled magnetic levitation systems", 2nd IEEE International Conference on Industrial Informatics, Vol. 1, Jun. 2004, pp. 335-338.

[126] Lin F. J., Teng L. T., Shieh P. H., "Intelligent adaptive backstepping control system for magnetic levitation apparatus", IEEE Transaction on Magnetics, Vol. 43, No. 5, May 2007, pp. 2009-2018.

[127] Benjamin C. Kuo and Farid Golnaraghi, Automatic Control Systems, Eighth Edition, John Wiley and Sons, 2003.

[128] Sigurd Skogestad and Ian Postlethwaite, Multivariable Feedback Control Analysis and Design, Second Edition, John Wiley and Sons, 2007.

[129] K. J. Astrom and B. Wittenmark, Adaptive Control, 2nd ed. Reading, PA: Addison-Wesley, 1995.

[130] R. Isermann, K. H. Lachmann and D. Matiko, Adaptive Control Systems, Prentice Hall, 1992.

[131] David G. Craig, "Modeling and control of a magnetically levitated microrobotic system", Masters Thesis, University of Waterloo, Department of Mechanical and Mechatronics Engineering, 2006.

[132] Hassan K. Khalil, Nonlinear Systems, Third Edition, Prentice Hall, Upper Saddle River, NJ, 2002.

[133] Mir Behrad Khamesee, A study on teleoperation of magnetically levitated microrobots for micromanipulation, Ph.D. Dissertation, Graduate School of Engineering, Mie University, Japan, March 1999.